# DEVELOPMENT OF A CROSS-SCALE HYDRODYNAMIC MODEL FOR ALL TEXAS COASTAL WATERS

# FINAL REPORT

Jiabi Du, Ph.D.
Kyeong Park, Ph.D.

College of Marine Sciences and Maritime Studies
Texas A&M University

August 31, 2024

Submitted to Texas Water Development Board
Contract No. 2300012715

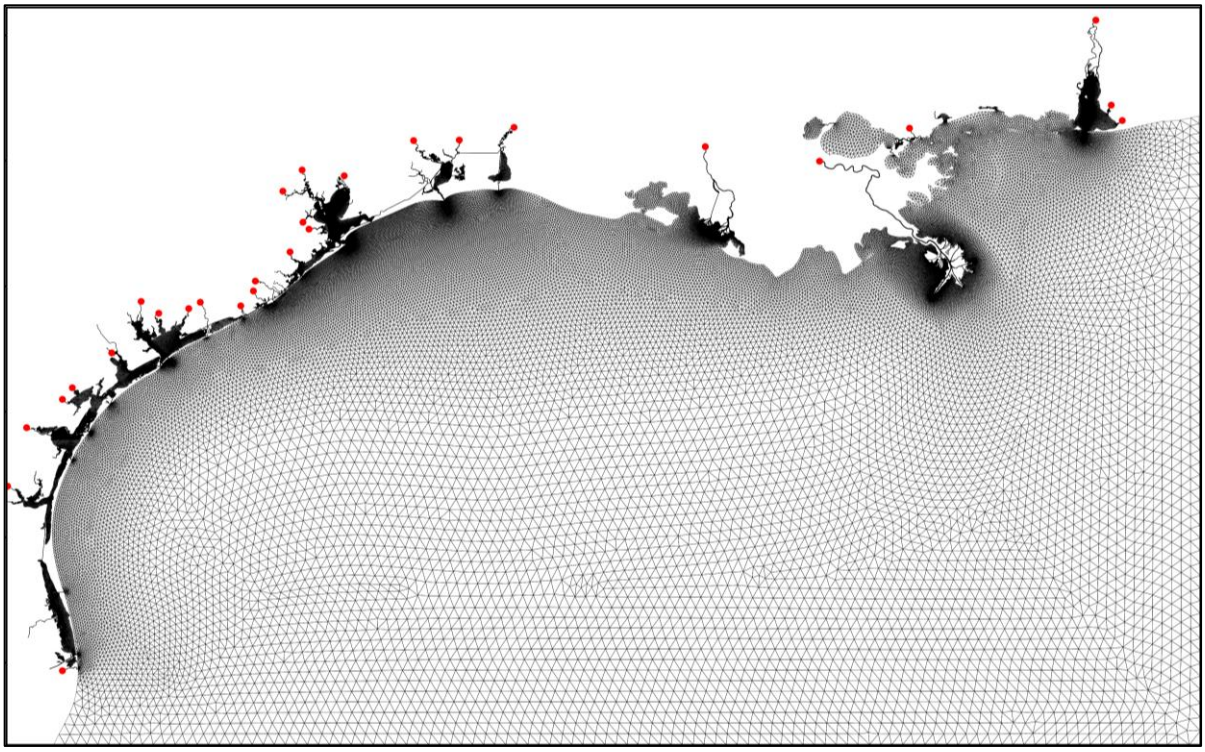

*This page is intentionally blank*

# Table of Contents

# List of Figures/Tables

# List of Acronyms

CUDEM: Continuously Updated Digital Elevation Model
DEM: Digital Elevation Model
NARR: North American Regional Reanalysis
HYCOM: Hybrid Coordinate Ocean Model
LSC: Localized Sigma Coordinates with Shaved Cells
SCHISM: Semi-implicit Cross-scale Hydroscience Integrated System Model
TABS: Texas Automated Buoy System
TAMU: Texas A&M University
TWDB: Texas Water Development Board
USACE: U.S. Army Corps of Engineers

# Executive Summary

The Texas Water Development Board (TWDB) contracted with the coastal ocean modeling team at College of Marine Sciences and Maritime Studies of Texas A&M University (TAMU) to develop a cross-scale hydrodynamic model with high-resolution grids for all major coastal bays along the Texas coast. The 3-dimensional hydrodynamic model is to replace the legacy model, TxBLEND, developed decades ago. Tasks of this project include model grid refinement, development of Python tools for preparing model input files, and analyzing model outputs.

This report details the model configuration, efficiency, and performance. The modeling team at TAMU has been working closely with TWDB to decide the model domain, mesh resolution, and Python tools. The model has been well calibrated in terms of water level, salinity, temperature, and tidal current in major Texas coastal bays as well as the shelf current at the inner Texas shelf ocean. Comparison of salinity between observation and 20-year simulations (2000-2019) suggests excellent and reliable model performance, particularly in Galveston Bay. A follow-up work is suggested to further improve the model performance in salinity in lower southwestern Texas bays such as Mission-Aransas Estuary and upper and lower Laguna Madre, where freshwater inflow is highly limited and hypersaline condition occurs. Model errors in salinity for lower Texas bays are notable and likely related to the uncertainty of freshwater inputs. Coupling with a watershed model is a potential solution to resolve this issue. Despite some discrepancies in salinity, the model has shown good performance in current velocities. Therefore, the model can serve as a reliable data source to provide essential velocity data for oil spill modeling.

Based on good model performance presented in this report, the TAMU modeling team believes the model is ready for operational use.

# 1 Introduction

To support regional water planning and development of environmental flow regime recommendations, the Coastal Science program at Texas Water Development Board (TWDB) has maintained a legacy 2D (vertically integrated) model, TxBLEND, for decades and recently decided to upgrade the modeling system to a 3D modeling system based on SCHISM (Semi-implicit Cross-scale Hydroscience Integrated System Model; Zhang et al. 2015; Zhang et al. 2016). A 3D model is more robust in resolving baroclinic processes (e.g., the two-layer estuarine circulation due to horizontal salinity gradient) that are important in water exchange between Texas bays and coastal ocean (Du et al. 2019). With the increasing availability of computer power, running a 3D high-resolution model has become a common practice for ocean forecasting.

An accurate hydrodynamic model could serve as a solid platform to address a variety of issues, especially in the coastal areas where terrestrial materials from watersheds and pollutants from coastal industry and community are aggregated, diluted, and exchanged with the open ocean. A numerical model, once well-calibrated, is an efficient tool for coastal resources and water quality management. A reliable numerical hydrodynamic model is highly demanded for Texas coastal waters given numerous existing environmental issues such as oil spills (Williams et al. 2017), petrochemical pollutants (Santschi et al. 2001; Lopez et al. 2022), harmful algal bloom (Buskey et al. 2001; Thyng et al. 2013), desalination projects (Hodges et al. 2006), mercury and microplastic release (Dellapenna et al. 2022), flooding (Huang et al. 2021), droughts (Bruesewitz et al. 2023), and hurricanes (Du and Park 2019). Those issues are likely to be worsened under a warming climate and increasing population along the coast.

Water movement, mixing, and transport are the fundamental processes for nearly every marine environmental issue. Simulating the transport and exchange processes in the coastal waters requires a hydrodynamic model to not only resolve the adjoining shelf-wide and open ocean dynamics (Zhu et al. 2015) but also the small-scale, highly variable processes near the coastline and inside estuarine bays as the shelf-open ocean and estuarine bays are closely connected. Connecting individual bays in an ocean model is especially important and demanded for Texas coastal waters. Extensive studies have shown that materials such as fish larvae and microplastic released at one Texas bay could reach other bays along the coast (e.g., Thyng and Hetland 2017; Steffen et al. 2023; Summers et al. 2024). A seamless, cross-scale, 3D hydrodynamic model is one of the most computationally efficient solutions when the model domain needs to cover a vast area.

In collaboration with TWDB, researchers at College of Marine Sciences and Maritime Studies, Texas A&M University (TAMU) have developed a hydrodynamic model for the entire Texas coastal waters, resolving detailed bathymetric and geometric features of the coastal bays, including all major and minor bays and estuaries, such as Galveston Bay, Matagorda Bay, San Antonio Bay, Aransas Bay, Corpus Christi Bay, and Laguna Madre. The model is based on Du et al. (2019), which used SCHISM (https://github.com/schism-dev: Zhang et al. 2016), an advanced, open-source model system that has been successfully applied worldwide.

In this project, the TAMU modeling team: 1) refined the model mesh for all major bays; 2) used updated bathymetry data from multiple reliable data sources; 3) created Python-based tools to

download data, prepare model inputs, and analyze model outputs. This report provides technical details and justifications for all these works. A secondary goal of this report is to provide necessary guidelines for future works (e.g., further refining the model grid for specific bays).

# 2 Grid generation

## 2.1 Model domain and grid

A relatively large model domain (97.79°W-87.00°W; 25.35°N-31.12°N) is selected that covers the northwestern part of the Gulf of Mexico (Fig. 2.1). The model domain includes not only the Texas coast but also the entire Louisiana coast, Mississippi coast, Alabama Coast, and portion of the western Florida coast (Figs. 2.1-2.2). Adopting such a large model domain is to include the great influence of major rivers such as the Mississippi and Atchafalaya rivers on the salinity in the Texas coast. In non-summer season, downcoast shelf current (moving from Louisiana to Texas) is prevalent, which moves a large river plume toward the Texas coast. It is thus especially important to include such large rivers in the model domain. With some of the Mississippi River plume also moving to the east, and as it is desirable to have a buffer zone in the model domain to allow the Mississippi freshwater to move and mix with surrounding ocean water, we extend the model domain about 200 km to the east of the Mississippi River. There are complex bathymetric and geometric features to the east of the Mississippi River, but the current model does not resolve all of them for computational efficiency.

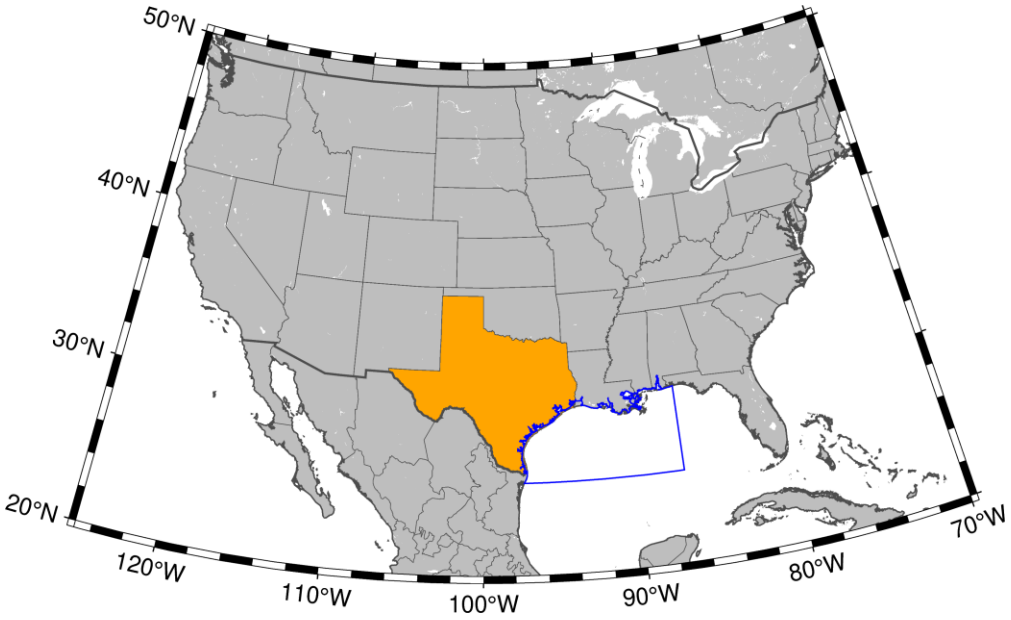


**Figure 2.1**: Map showing the outline of the model domain (blue line), with Texas highlighted with a yellow polygon.

The model domain also includes a relatively large portion of the deep Gulf to 1) allow the impact of deep ocean dynamics, such as mesoscale eddies cascading into the coastal zone, and 2) provide a large buffer zone for the shelf-wide dynamics, such as the cross-shelf mixing of freshwater. In the current model domain, the deepest part has a depth of 3,604 m.

We elected to use an unstructured hybrid mesh composed primarily of triangular elements for most of the domain, with rectangular elements (referred to here as “quads”) in navigation and ship channels for better computational efficiency and accuracy (Kim et al. 2014). For each major coastal bay, the grid was refined to faithfully resolve the land boundaries (Fig. 2.3). In total, there are 118,200 nodes and 188,395 elements (see Fig. 2.4 for the final mesh). With spatial

resolutions varying from 10 km in the deep ocean to ~30 m in the shipping channels. The following sections will describe the details of mesh generation.

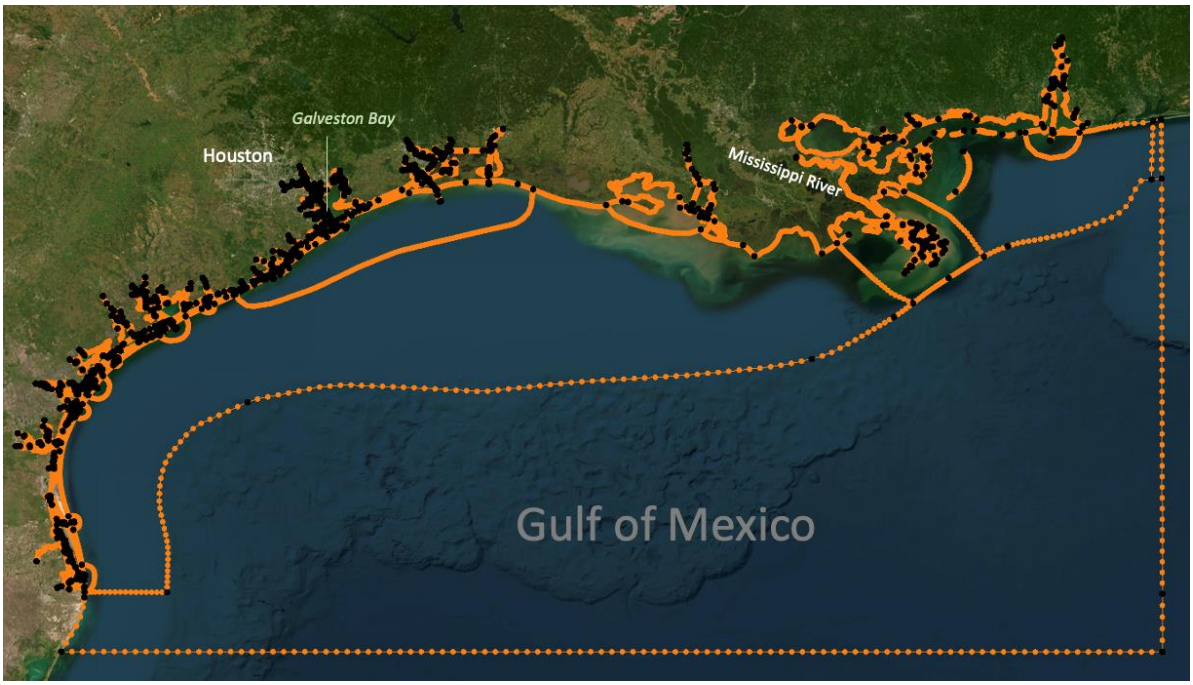


**Figure 2.2**: Model domain and controlling points (yellow and black dots) for mesh generation. Controlling points are used to control the grid resolution and grid type (quads or triangles). Black dots are controlling points (known as node in Aquaveo SMS) used to define arcs (an arc is controlled by two black dots). The yellow dots are typically evenly distributed but manually adjusted to capture complex bathymetry and coastal geometry.


**Figure 2.3**: A zoom-in view of the controlling points for the mesh in Galveston Bay (left) and upper Galveston Bay (right). Grid nodes were created in a way to faithfully represent the land boundaries and navigation channels.

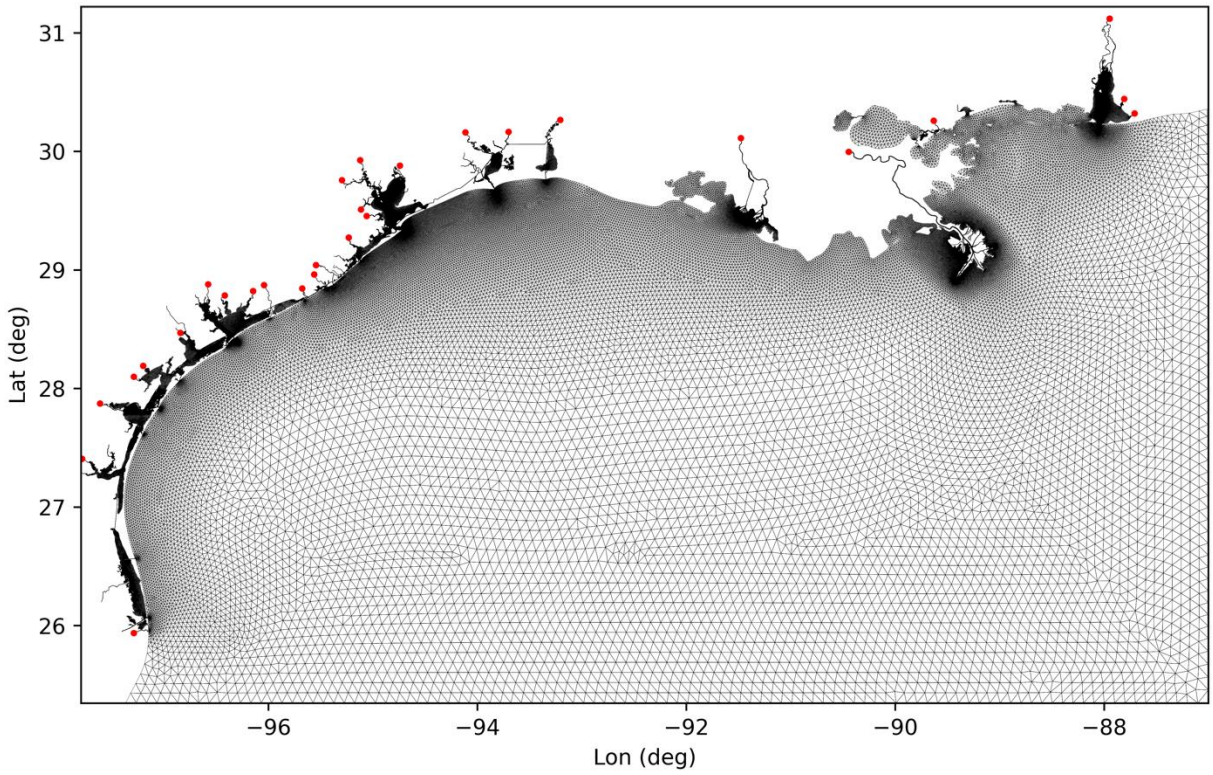


**Figure 2.4**: Model mesh (Version 2.7.0) with red dots indicating the freshwater input locations.

## 2.2 Resolving ship channels

One of the most critical elements in generating the model grid is resolving the deep but narrow ship channels. The deep ship channel plays a key role in the movement of water and solutes (e.g., salt). The strength of estuarine circulation, which determines the strength of exchange flow, is proportional to the cube of depth (MacCready 2004). Then, the circulation strength in a channel with 15 m depth would be 125 times stronger than that over a shallow shoal of 3 m depth. We hence put great efforts into resolving the channels, carefully (and often manually) aligning grid nodes to the channel edge using 5 and 10 m isobaths, respectively, as the upper and lower edges of the channel slope (Fig. 2.5). A minimum of 5 grid nodes are used to resolve the channel, with 2 nodes at both the upper and lower edges of the channel and 1 node at the middle the channel (Ye et al. 2018). To better resolve the channel bathymetry, we use 5 grid nodes in the deep channels and 4 grid nodes on the slopes, i.e., a total of 9 grid nodes (Fig. 2.5). To ensure the same number of grid nodes across a channel over the entire length of the channel, we use the quads (rectangular grids with four vertices in each element; an element refers to the area enclosed by grid lines).

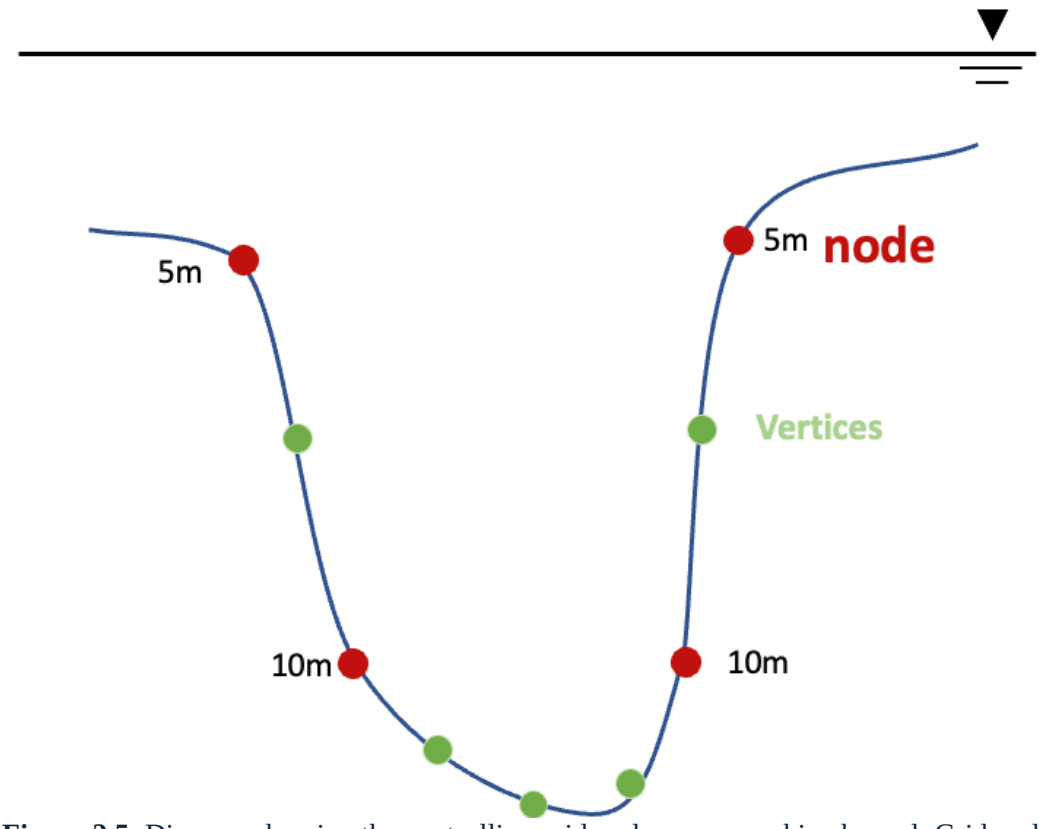


**Figure 2.5**: Diagram showing the controlling grid nodes across a ship channel. Grid nodes (red dots) are manually defined at 5 and 10 m isobaths while the vertices (green dots) between nodes are evenly distributed between the lower edge of the channel (10 m isobath) and between the 5 and 10 m grid nodes.

We follow the following sequence when resolving ship channels: 1) to get the bathymetry contours, specifically the 5 and 10 m contours from ArcGIS (or other software such as QGIS); 2) to import the contours into the Aquaveo SMS by adding the contours shapefiles; 3) to add controlling grid nodes along the 5 and 10 m isobaths (Fig. 2.6). Typically, multiple patch polygons (used to generate quads in SMS) are used along the ship channel. It is essential to keep the number of vertices the same on both sides of each patch polygon. Otherwise, some bad-quality and highly skewed quads or triangle grids will be generated. In some cases (although rare), using an uneven number of vertices on opposite sides may be necessary. For instance, in the areas where the channel is heavily curved, perfect quads are not feasible near the curvature of ship channels (Fig. 2.7). Examples of the grids around ship channels in major Texas bays are shown in Fig. 2.8.

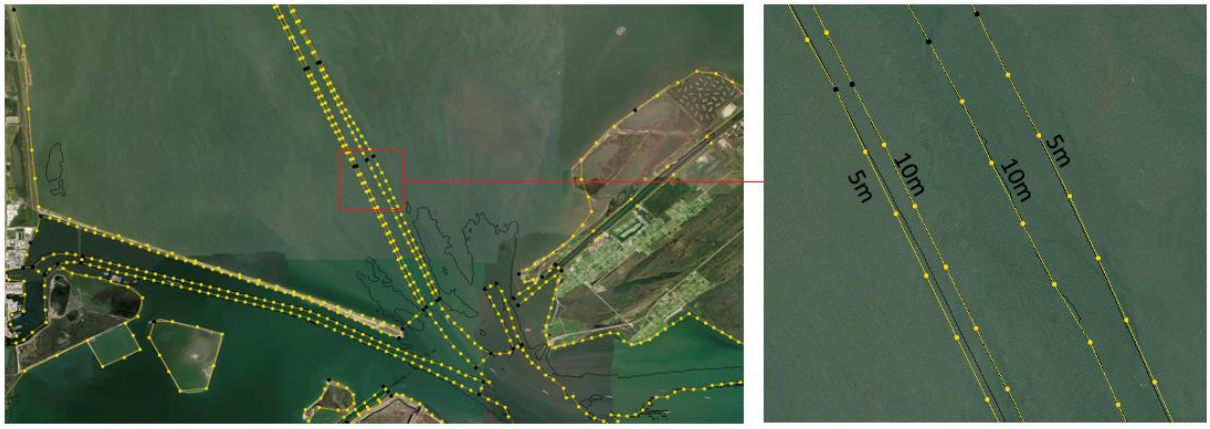


**Figure 2.6**: Mesh controlling vertices (yellow dots) along a ship channel in lower Galveston Bay (29.39N, 94.82W). The yellow lines are the controlling arcs. The black thin lines denote the 5 and 10 m isobaths. The 10 m isobath in the right panel is hardly visible because the controlling arcs are aligned closely with the isobath.

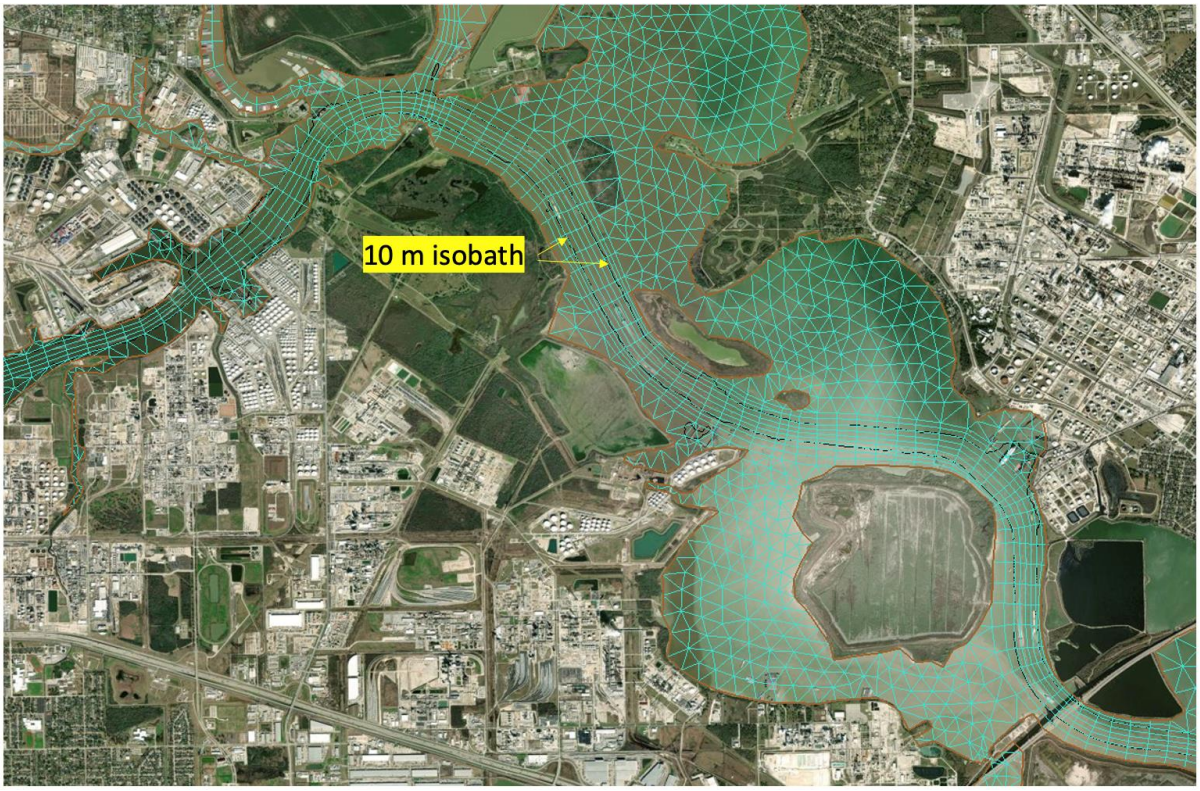


**Figure 2.7**: Grid in the upper Galveston Bay, highlighting how the quads are used to represent the curved ship channel. Thin black lines are the 5 and 10 m isobaths.

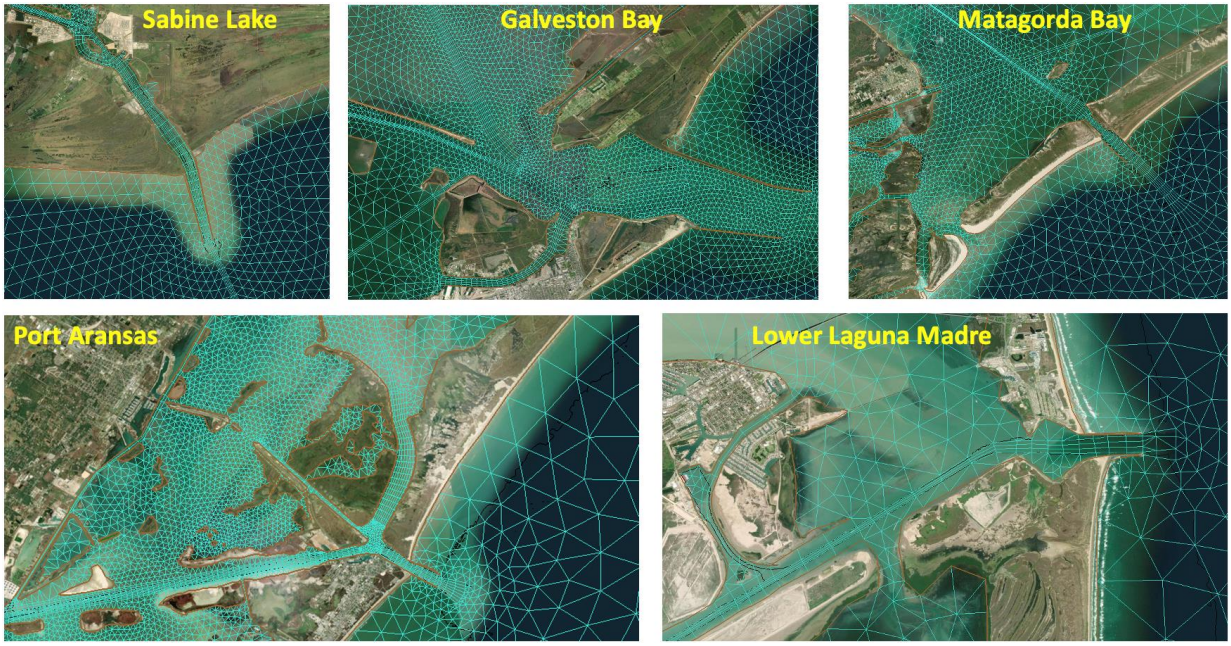


**Figure 2.8**: Zoom-in view of the grid of ship channels in Sabine Lake (29.68N, 93.83W), Galveston Bay (29.34N, 94.73W), Matagorda Bay (28.43N, 96.33W), Port Aransas (27.84N, 97.05W), and Port Isabel (26.06N, 97.15W).

## 2.3 Resolving Intracoastal Waterway

One major feature that connects different bays in the model domain is the Intracoastal Waterway (ICW), a 3,000-mile (4,800 km) inland waterway along the Atlantic and Gulf of Mexico coasts of the United States. Some sections of the waterway consist of natural inlets, saltwater rivers, bays, and sounds, while others are artificial canals. It provides a navigable route along its length without many of the hazards of travel on the open sea.

The ICW is typically deeper (3-5 m) than the shoals (2-3 m) in Texas bays. We use elongated quads to resolve the ICW, with 3 grid nodes across the waterway, including 1 controlling node at the deepest part of the waterway (Figs. 2.9-2.10). Using quads has the advantage of: 1) capturing the deepest part of the channel, 2) using fewer number of elements, and 3) having better computational efficiency.

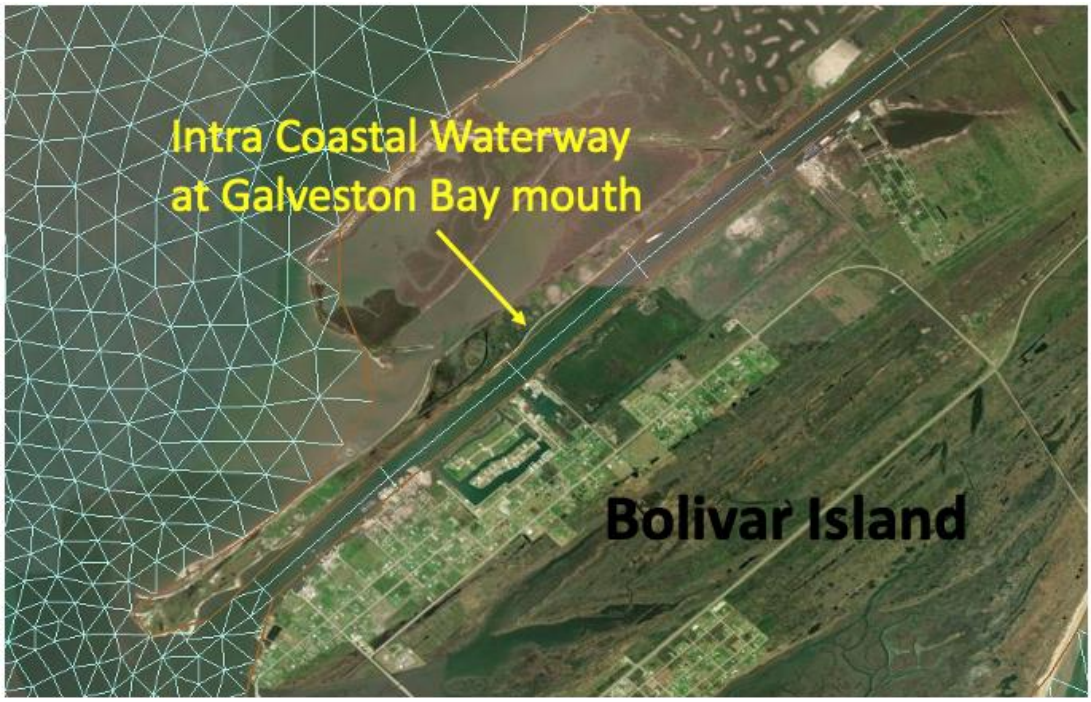


**Figure 2.9**: Grid for Intracoastal Waterway in a canal, an example near the Galveston Bay mouth.


**Figure 2.10**: Grid for Intracoastal Waterway in the open water, an example at Aransas Bay.

## 2.4 Resolving small creeks and embayment

Hydrodynamics in small creeks and embayment is less sensitive to the grid configuration. However, the surface area of these open waters affects the tidal prism and, therefore, tidal currents. The more coastal embayment and creeks for a given bay, the larger the tidal basin and the stronger the tidal current at the bay entrance.

We include all coastal embayment and creeks with a width (or length) exceeding 100 m. One good example is the low-lying area to the east of Sabine Lake (Fig. 2.11), where a large lagoon-type open water is connected to Sabine Lake by a narrow channel (~30 m wide).

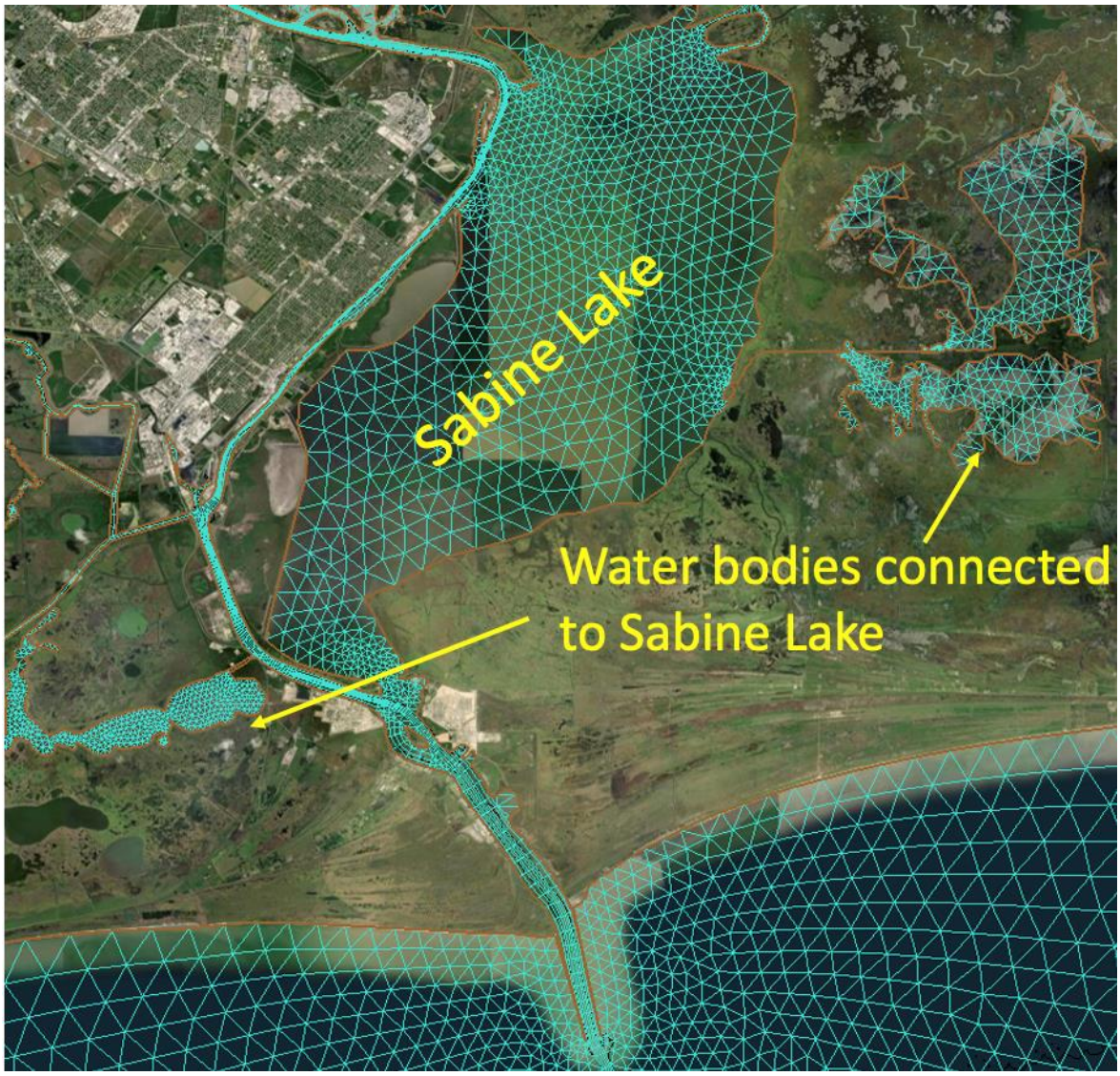


**Figure 2.11**: Grid for the lagoon-type open water to the east of Sabine Lake. Note the narrow channel (barely seen in the plot) that connects the lagoon-type water and the main Sabine Lake.

## 2.5 Resolving small islands

The existence of islands affects water movement and exchange between bays and coastal oceans. There are numerous islands near the Intracoastal Waterway created from dredge spoil deposits. These islands, despite their small sizes, have the potential to influence the current velocity. We resolve islands with a width or length larger than 100 m (see examples in Figs. 2.12-2.13).

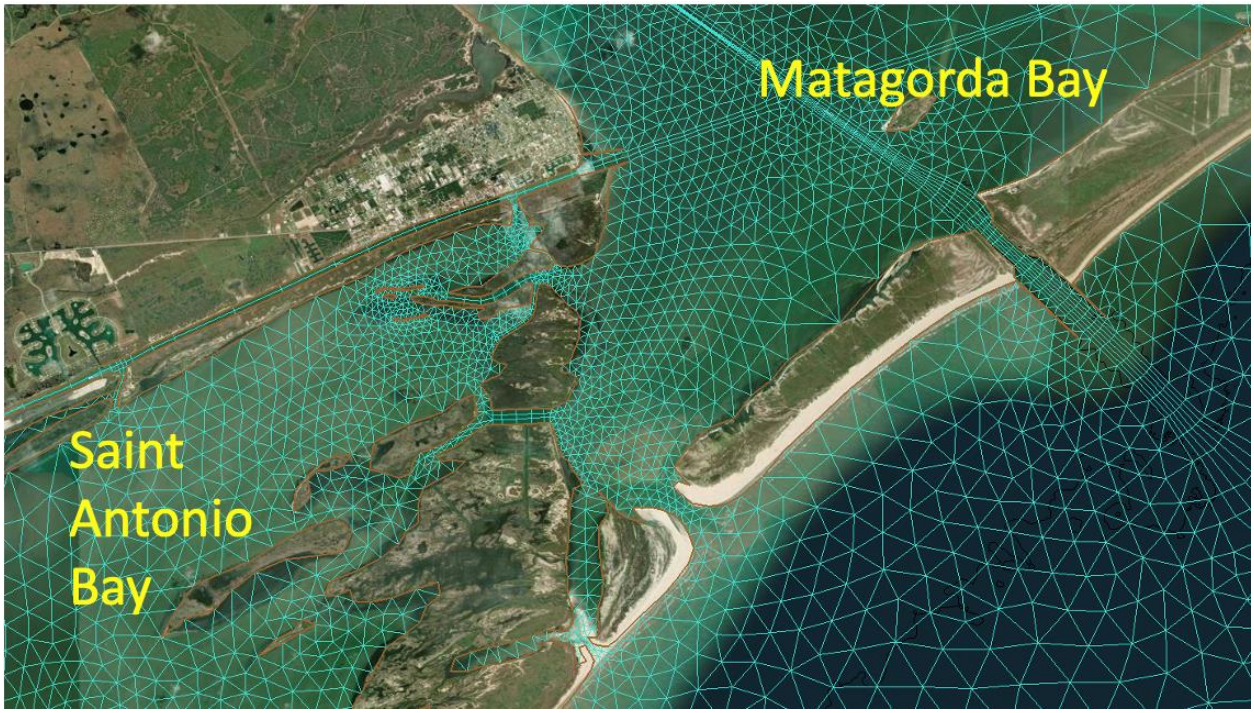


**Figure 2.12**: Grid showing islands between Matagorda Bay and Saint Antonio Bay (28.40N, 96.42W)

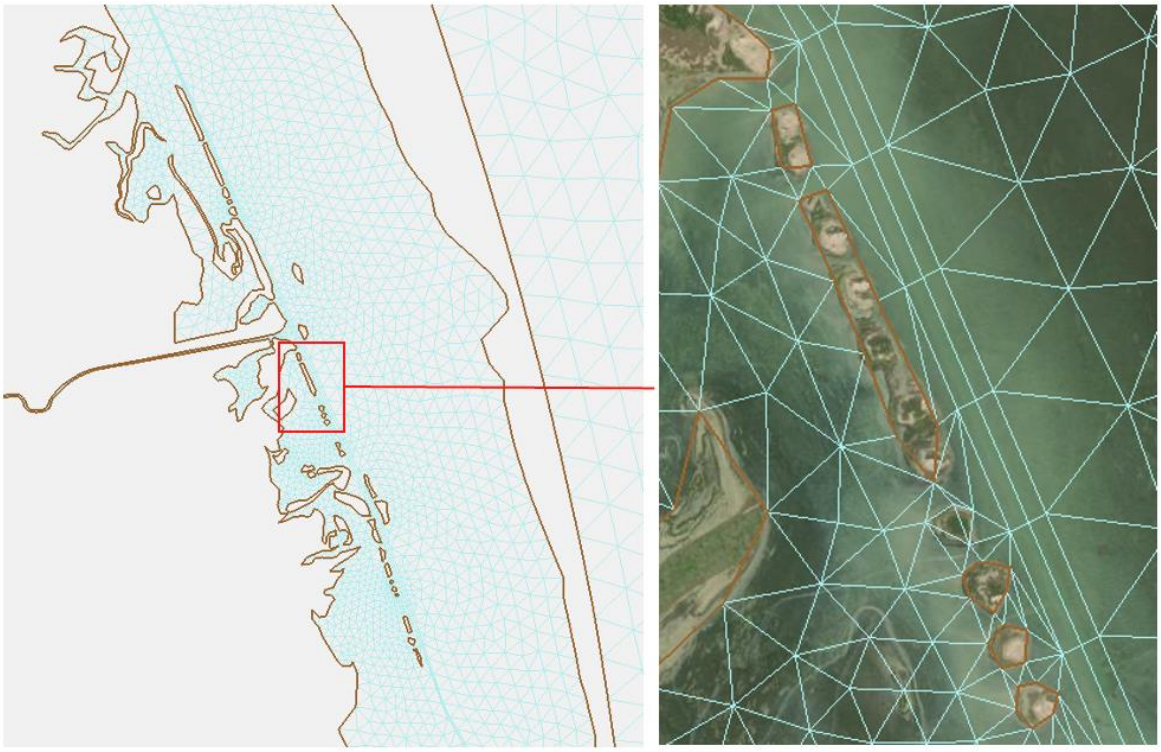

**Figure 2.13**: Grid showing small islands near the Intracoastal Waterway in lower Laguna Madre (26.34N, 97.32W).

## 2.6 Vertical grid

SCHISM has the flexibility of using different types of vertical grids, including S-Z grid and LSC$^2$ (Localized Sigma Coordinates with Shaved Cell; Zhang et al. 2015). LSC$^2$ is a more advanced vertical grid, which allows for a different number of sigma layers depending on the local depth. It has two advantages: 1) faithfully representing bathymetry; and 2) leading to better computational efficiency, especially when there is a vast shallow area where one can apply a small number of vertical layers. The second advantage is especially important when simulating flooding (i.e., inundation). Although the current model development does not include the flooding simulation components, using the LSC$^2$ will make it easier for future development for flooding. In the LSC$^2$, one can determine the minimum number of layers. After testing different minimum numbers of layers, we decide to use 10 minimum layers for accuracy. Figures 2.14 and 2.15 show the vertical grid from the deep Gulf to the Texas coast and across the Houston Ship Channel. Compared to the S-Z grid, using LSC$^2$ allows to avoid strong curvature of the vertical grid across a ship channel (Fig. 2.16).

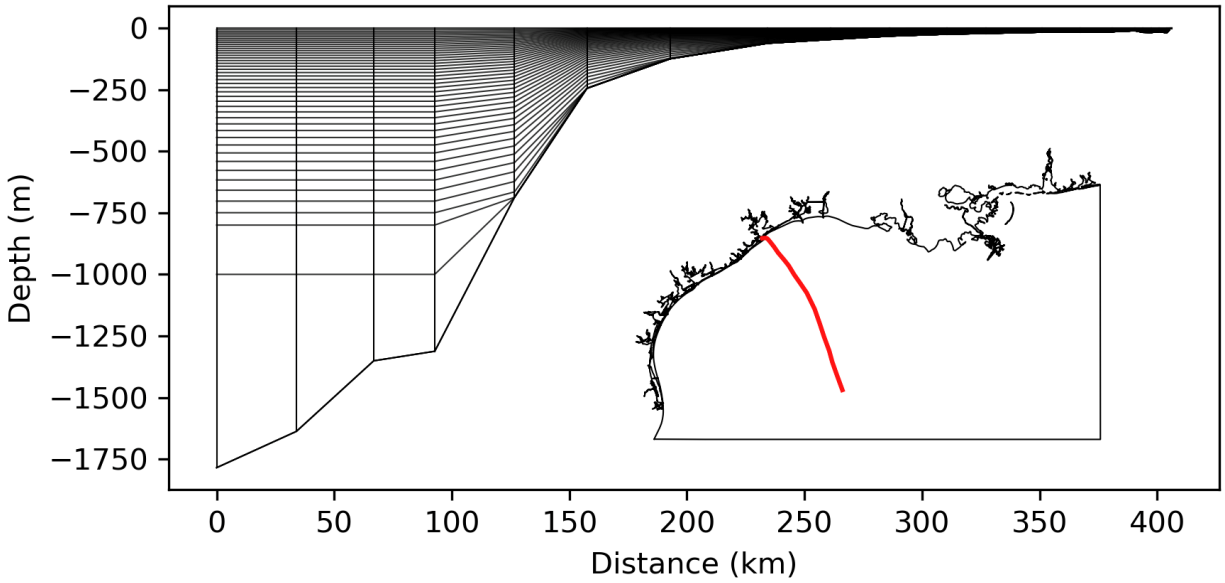


**Figure 2.14**: Vertical grid along a transect (red line in the subset) from the deep Gulf to the Texas Coast.

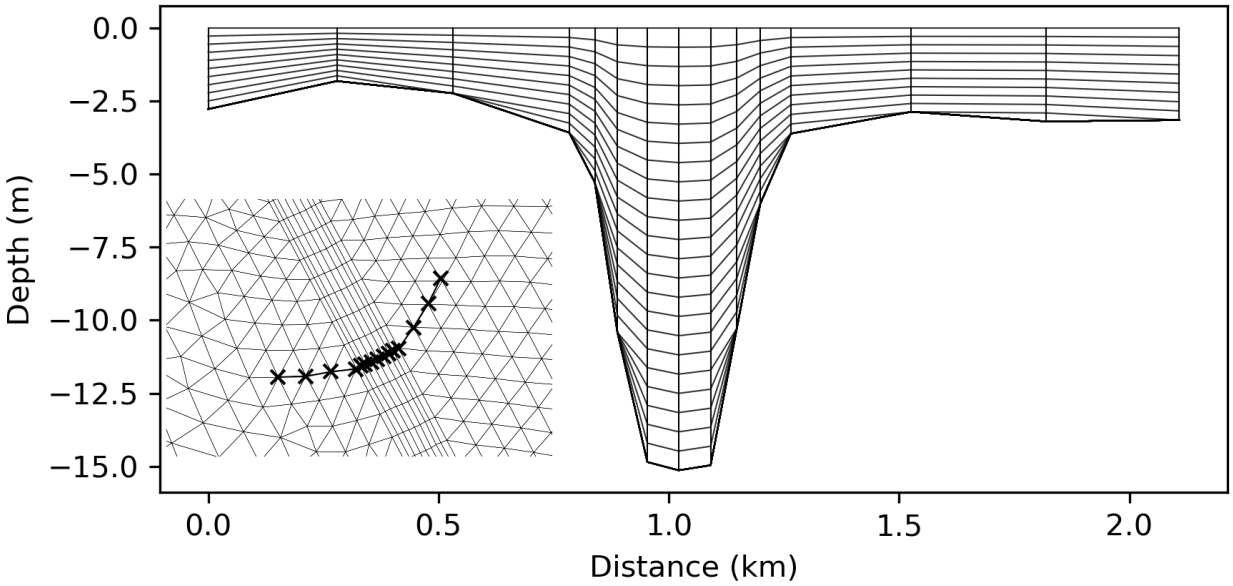


**Figure 2.15**: Vertical grid along a cross-section across Houston Ship Chanel in the lower Galveston Bay. Grid nodes whose vertical layers are plotted are marked with a black cross in the bottom-left subset.

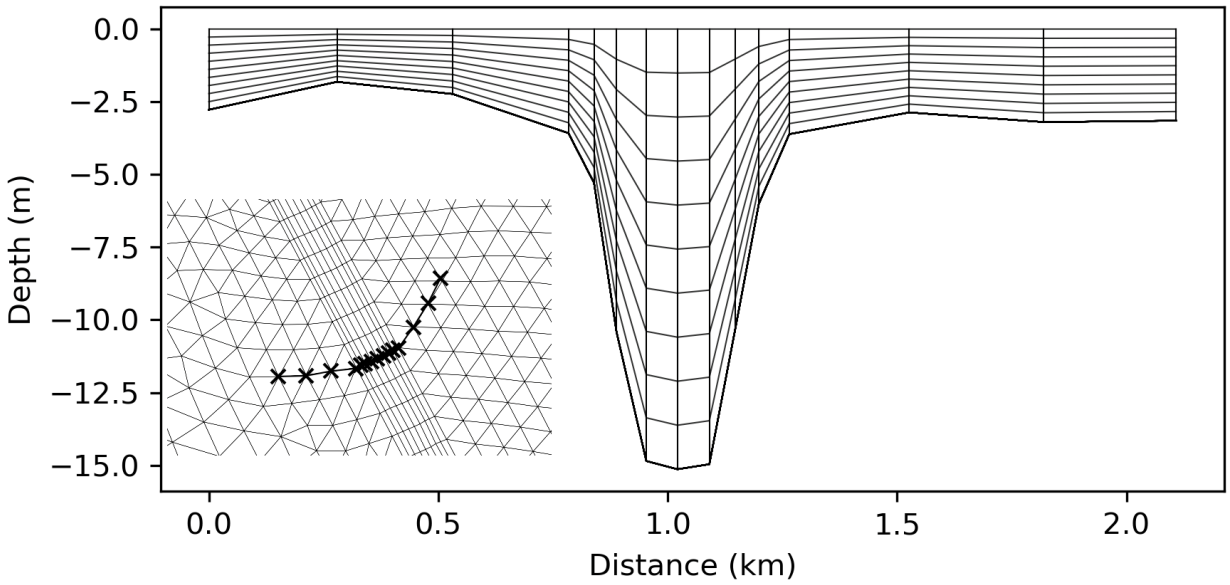


**Figure 2.16**: Example of pure sigma vertical grid (10 layers) along the same cross-section as in Fig. 2.15 across the Houston Ship Channel in the lower Galveston Bay.

# 3 Bathymetry

## 3.1 Bathymetry data

Bathymetry data from four sources are used, including ETOPO1 (1 arc-minute global relief model; developed by the National Geophysical Data Center; https://www.ncei.noaa.gov/products/etopo-global-relief-model), CUDEM (3 arc-second Continuously Updated Digital Elevation Model; maintained by NOAA; https://chs.coast.noaa.gov/htdata/raster2/elevation/NCEI_ninth_Topobathy_2014_8483), in situ surveys by Geodynamics, Inc. under a contract with TWDB, and channel survey data by USACE (United States Army Corps of Engineers). When assigning the bathymetry to each model grid node, these data have been used one by one with later ones having a higher priority. That is, the model grid was first assigned with bathymetry from ETOPO1. For those grids within the CUDEM coverage, their bathymetry was overwritten with data from CUDEM, with the same process repeated with data from Geodynamics and then USACE.

Of the four bathymetry data sources, the CUDEM is the major one. CUDEM covers the nearshore region along the US coast (Fig. 3.1) and has a very high resolution (~3 m), high enough to resolve small bathymetric features including the IWC. The contours (e.g., 5 and 10 m isobaths) used in mesh generation are based on the CUDEM data. CUDEM uses the NAVD88 vertical datum (Amante et al. 2023).

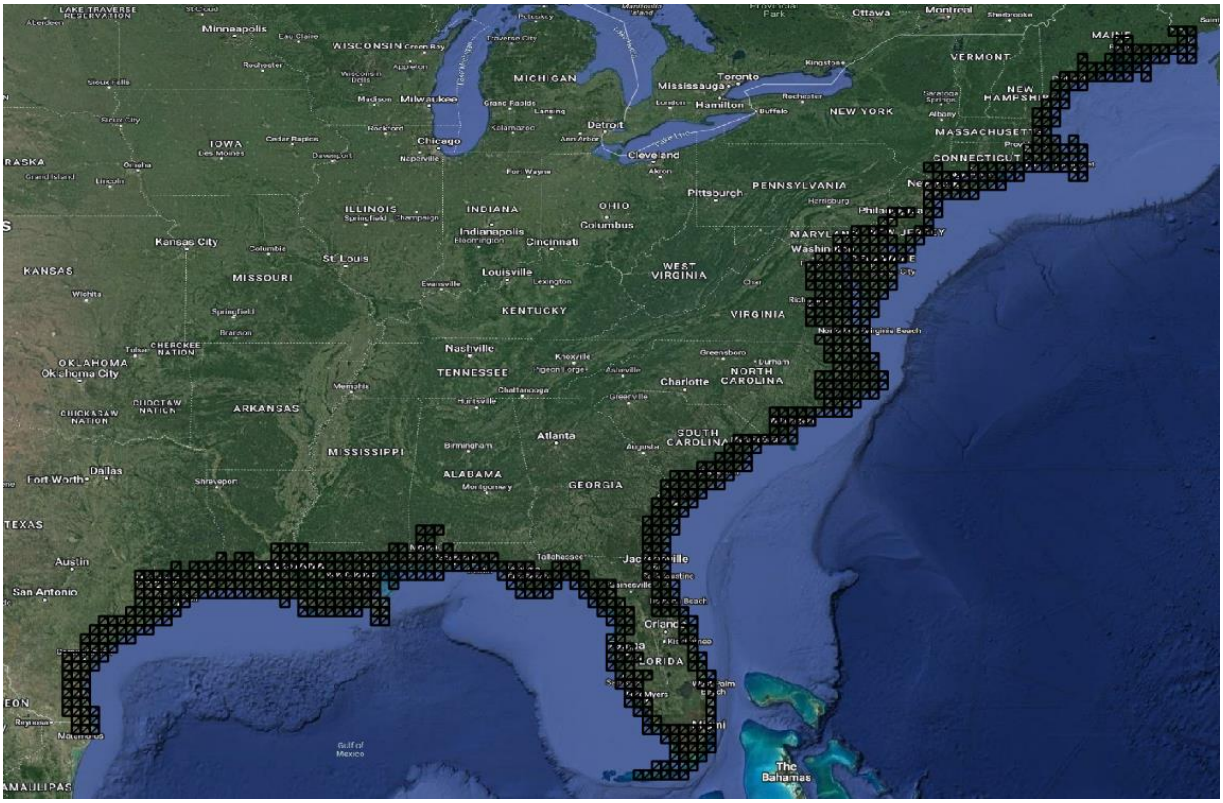


**Figure 3.1**: Coverage of CUDEM, with each black rectangle indicating a tile of bathymetry data.

## 3.2 Recent survey data from TWDB

High-resolution bathymetry survey (through a contract to company Geodynamics, Inc.) in Nueces Bay, San Jacinto River, Houston Ship Channel Shallows, and Lower Galveston Bay were conducted between August and November of 2023 (Fig. 3.2). The survey products were re-processed by the TAMU modeling team, which were reprojected into the lon/lat format and interpolated into a predefined mesh with a resolution similar to the original data. Note that the survey data in lower Galveston Bay does not include the ship channel, for which we used the USACE survey data. The bathymetry data provided by Geodynamic, Inc. use the vertical datum of NAVD88.

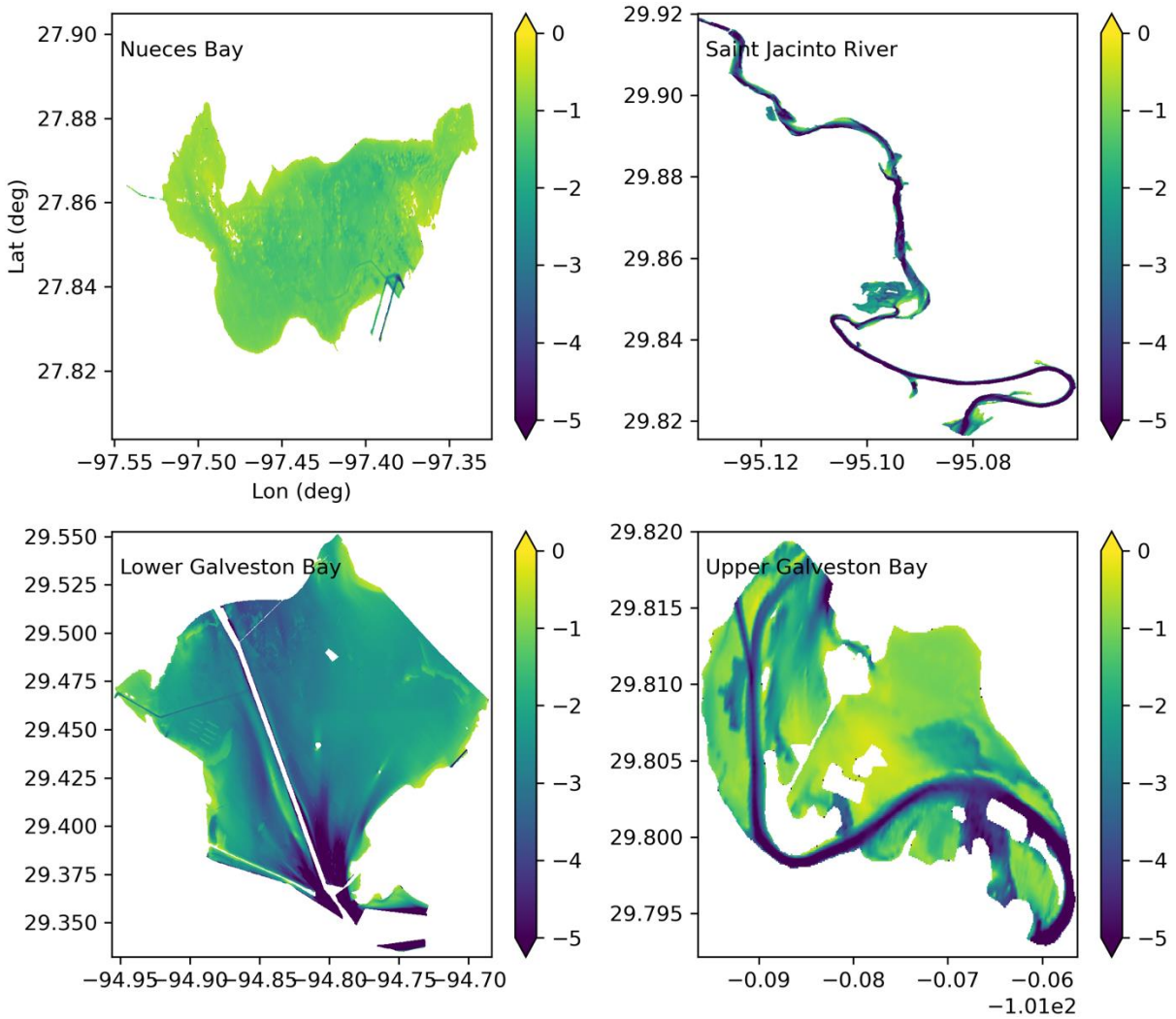


**Figure 3.2**: Reprocessed bathymetry data (unit of the color scale: m) based on the recent surveys by Geodynamics, Inc. Not all the survey data are shown here.

## 3.3 Processing USACE survey data

The USACE survey data covers most ship channels and ICW (Fig. 3.3). There have been 1400+ surveys conducted by USACE since January 2023 for Texas coastal waters. We downloaded the raw survey data from the USACE data portal and mapped the data from its original format (scatted data points) onto a predefined mesh. Two additional challenges arose when processing the data: 1) the challenge of downloading the 1401 zip files; and 2) the difficulty of excluding invalid interpolated data. The second challenge was especially hard to resolve. In the recent USACE and TWDB survey data, the ship channels are typically deeper than those in the CUDEM data. In the Houston Ship Channel, for example, the USACE bathymetry is deeper by up to 3 m than the CUDEM (Fig. 3.4).

The USACE bathymetry data use the Mean Lower Low Water (MLLW) datum, which is lower than the NAVD88 by 0.17 m at the Galveston Bay mouth (at NOAA station 8771341), 0.19 m at Port Aransas (at NOAA station 8775241), and 0.26 m at Port Isabel (at NOAA station 8779770). The difference is much less than the difference between different datasets (Fig. 3.4), and the datum difference is unlikely to impact modeling results significantly. Currently, the bathymetry data were used without any datum correction. A correction is suggested for future upgrades.

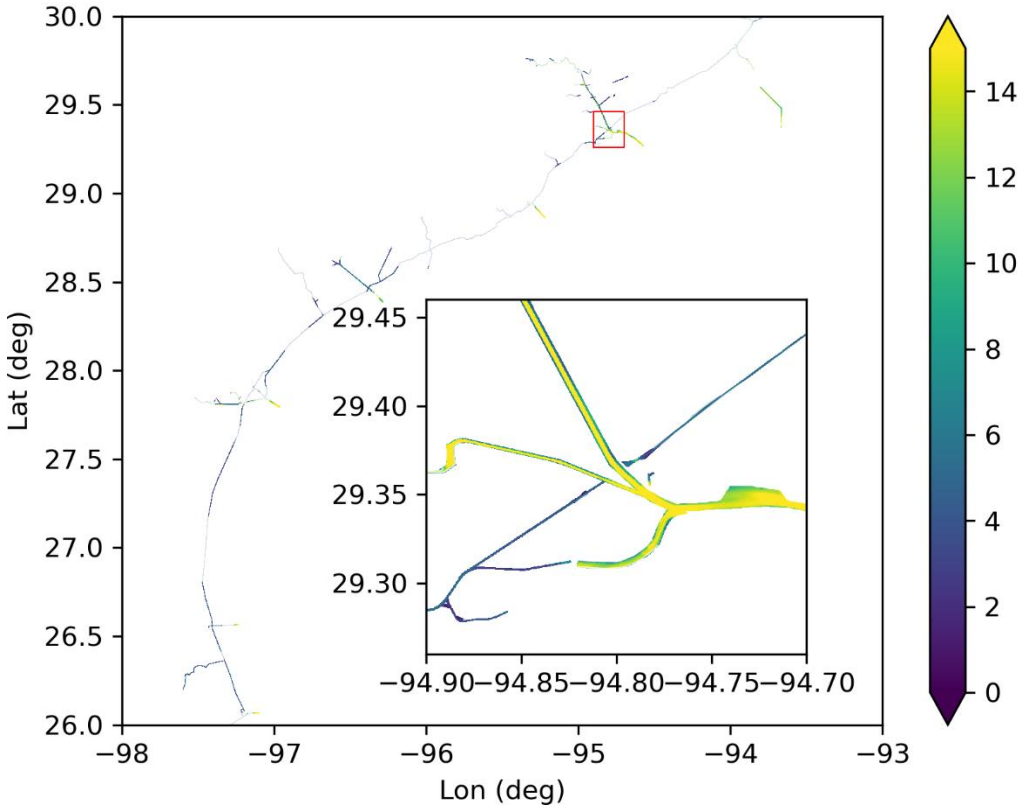


**Figure 3.3**: Coverage of the 1401 U.S. Army Corps of Engineers (USACE) surveys since January 2023 for Texas coastal waters. A zoom-in view of the processed bathymetry data (unit of the color scale: m) near Galveston Bay mouth is shown in the subset.

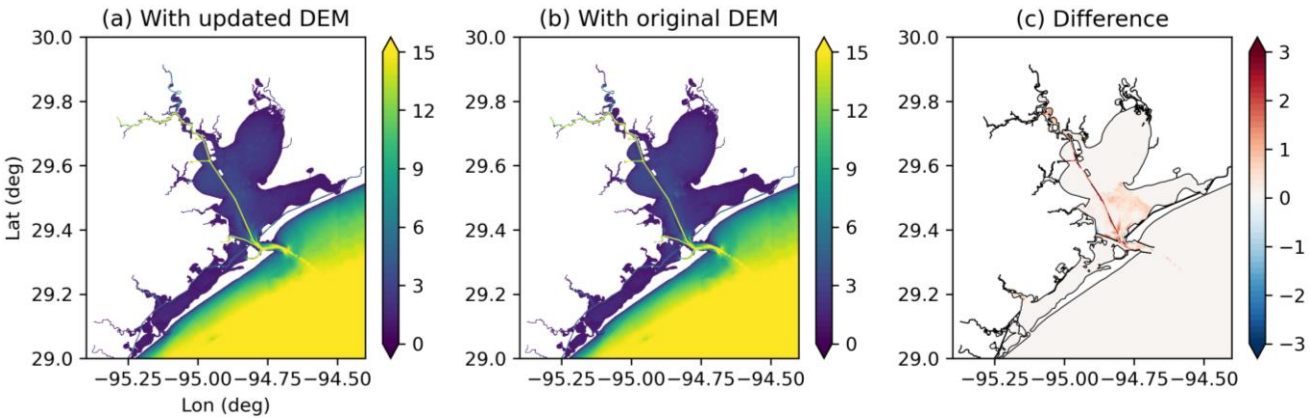


**Figure 3.4**: Model bathymetry with updated and original DEM (Digital Elevation Model) data (unit of the color scale: m) for Galveston Bay, with the last panel showing the difference (updated – original).

## 3.4 Final bathymetry in the model

Examples of the assigned bathymetry for 5 Texas bays are shown in Figs. 3.5-3.10. It is important to ensure that the ship channels are clearly represented in the model bathymetry.

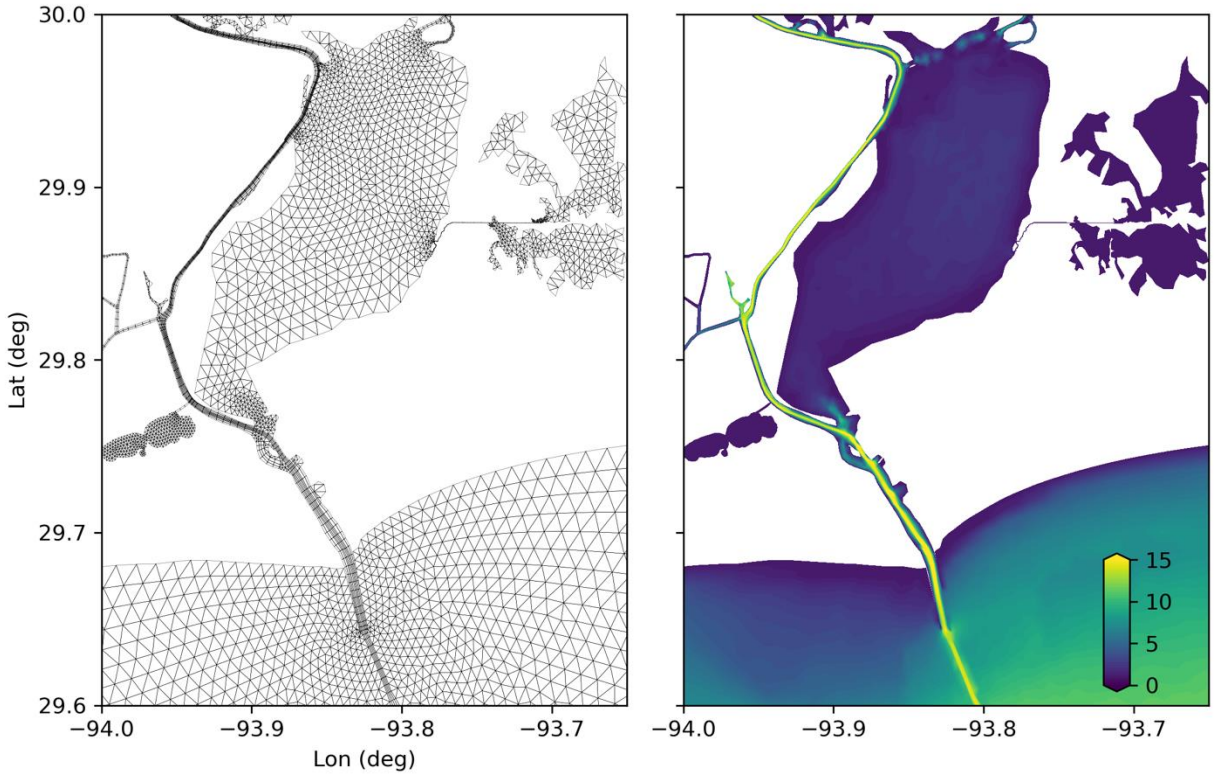


**Figure 3.5**: Model grid and bathymetry (unit of the color scale: m) for Sabine Lake.

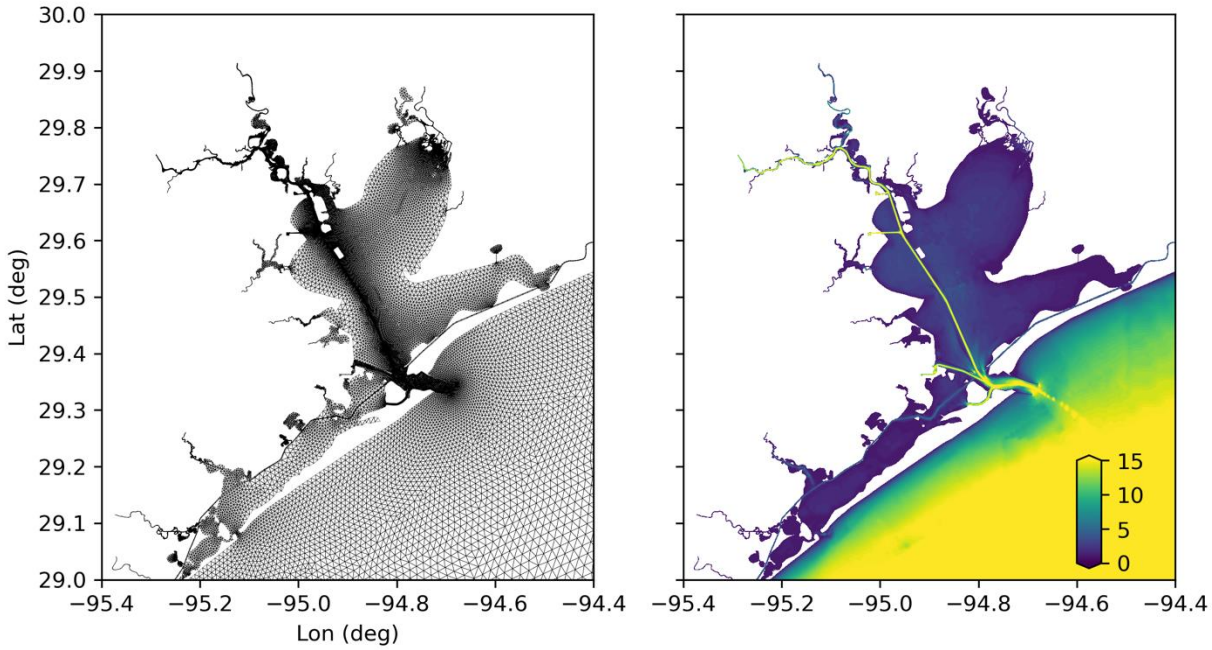


**Figure 3.6**: Model grid and bathymetry (unit of the color scale: m) for Galveston Bay.

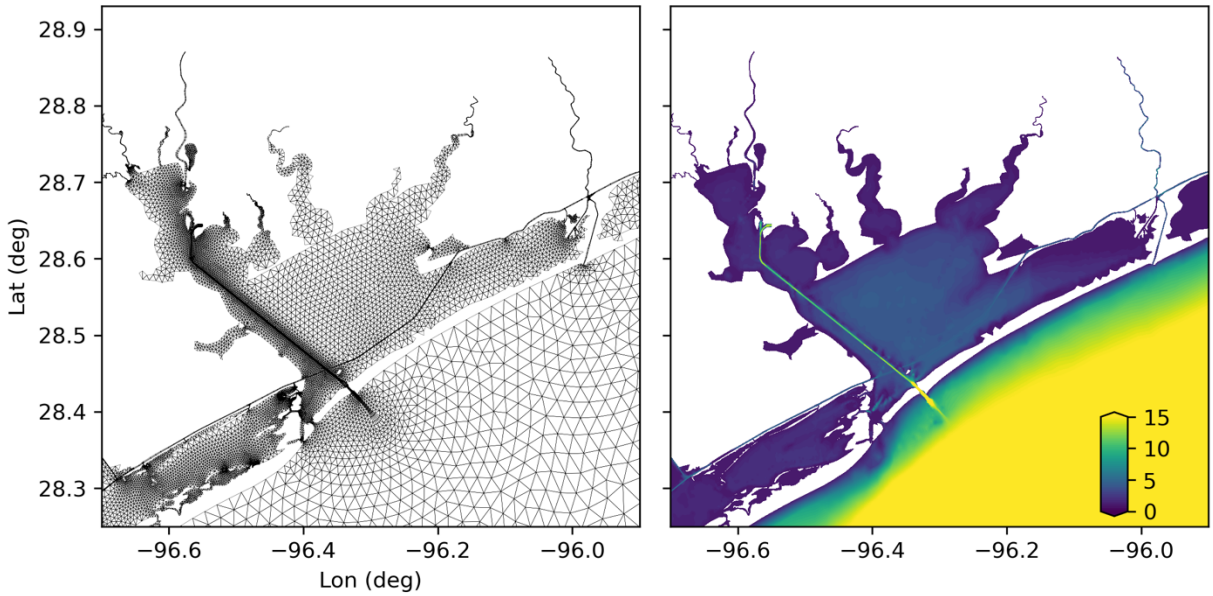


**Figure 3.7**: Model grid and bathymetry (unit of the color scale: m) for Matagorda Bay.

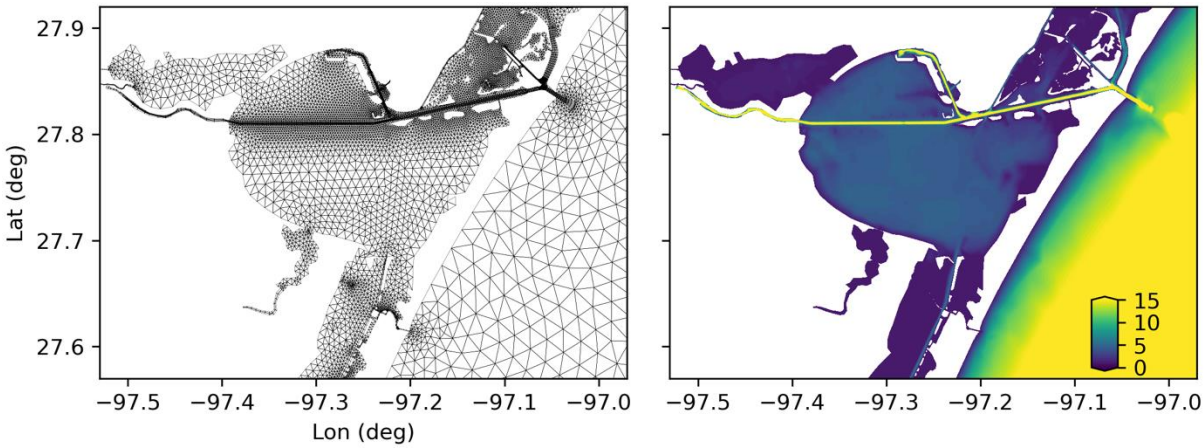


**Figure 3.8**: Model grid and bathymetry (unit of the color scale: m) for Corpus Christi Bay.

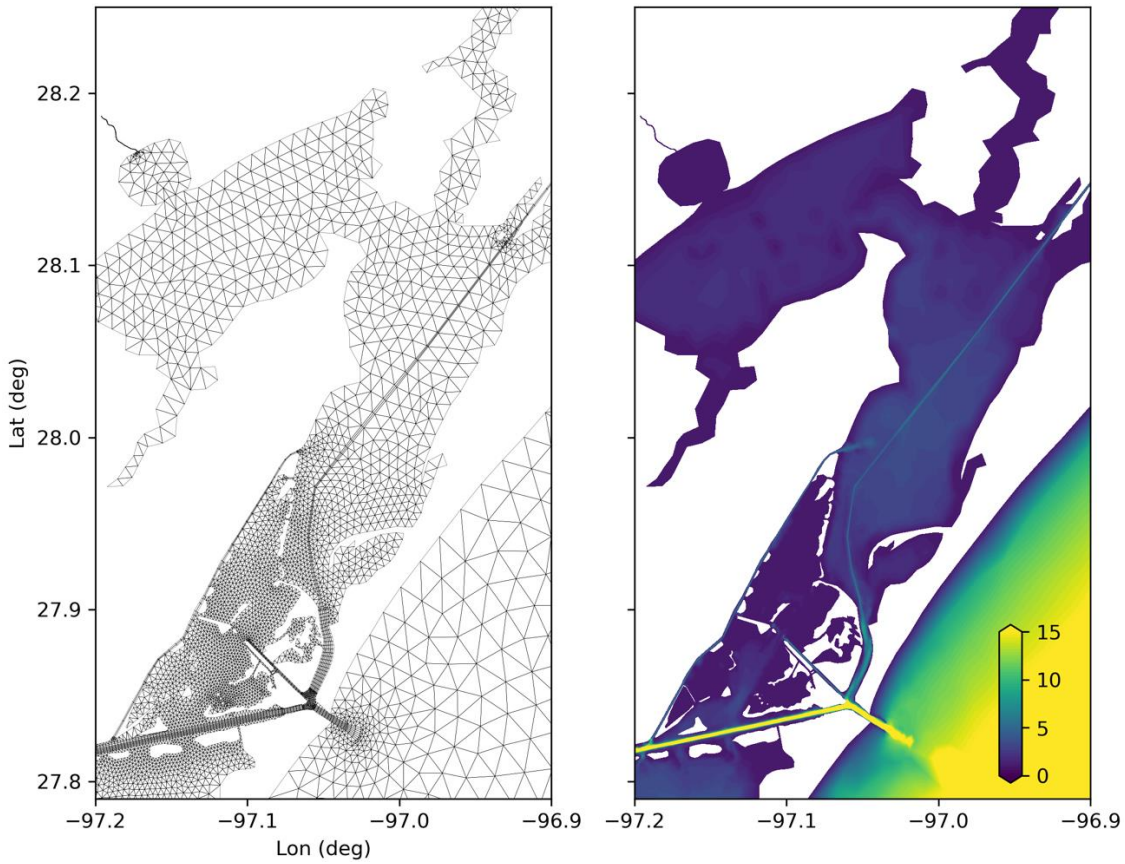


**Figure 3.9**: Model grid and bathymetry (unit of the color scale: m) for Mission-Aransas Estuary.

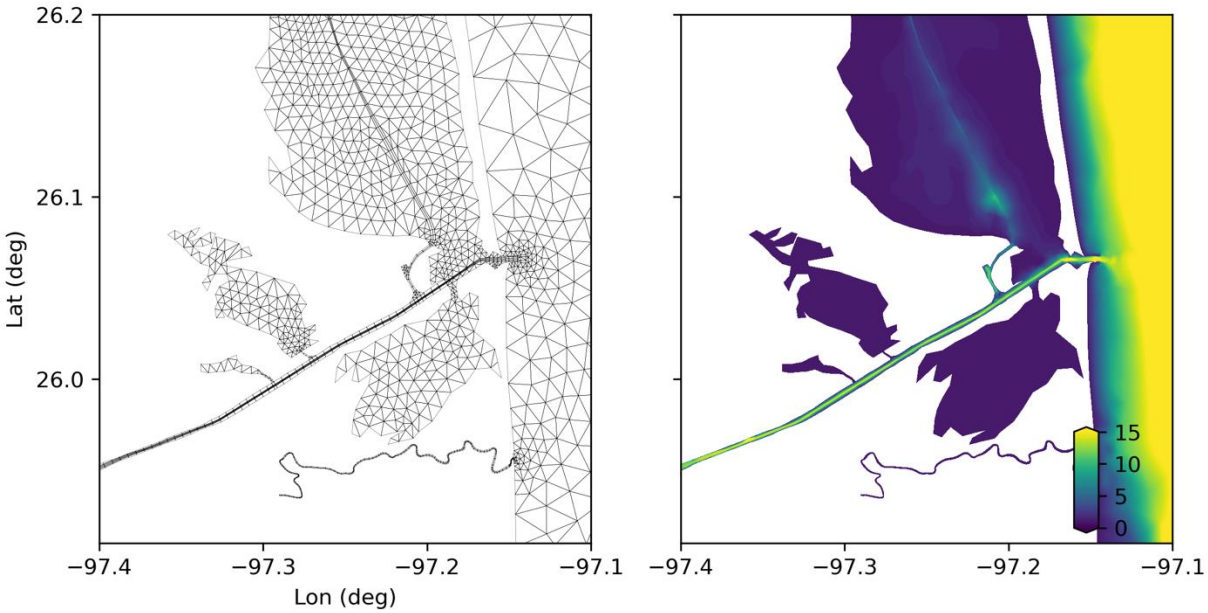


**Figure 3.10**: Model grid and bathymetry (unit of the color scale: m) for Lower Laguna Madre.

# 4 Model input files

To drive the model, several types of input files are needed for: 1) model grids (horizontal and vertical); 2) stream flow and water temperature at river boundaries; 3) salinity, temperature, water level, and velocity at ocean boundaries; and 4) atmospheric forcing such as air pressure, wind, humidity, solar radiation, and precipitation. The input files are either in ASCII or netCDF format.

Major input files and their purposes are listed below.

a) hgrid.gr3 and hgrid.ll: model mesh files with node-centered spatial data and mesh connectivity. If using the lon/lat coordinate, these two files are identical.
b) TEM_nudge.gr3 and SAL_nudge.gr3: nudging coefficients in the nudging zone (~50 km from the ocean boundary).
c) watertype.gr3: water type. A constant value of 1 (open water) is used.
d) albedo.gr3: spatially varying albedo. A constant value of 0.15 is used.
e) drag.gr3: drag coefficient. A constant value of 0.0025 is used.
f) diffmin.gr3: minimum diffusivity. A constant value of $10^{-6}$ is used.
g) diffmax.gr3: maximum diffusivity. A constant value of $10^{-2}$ is used.
h) windrot_geo2proj.gr3: used to rotate winds in case they do not align with coordinate axes. A constant value of 0 is used since no rotation is needed.
i) xlcs.gr3: used to define the surface mixing length scale. A constant value of 0.5 is used.
j) tvd.prop: switch for the 2$^{nd}$ order TVD transport scheme. A constant value of 1 is used.
k) vgrid.in: vertical grid.
l) bctides.in: file specifying the boundary conditions. Tidal amplitude and phase information comes from FES2014 (Carrere et al. 2015).
m) hotstart.nc: netCDF file specifying the initial conditions for salinity, temperature, and surface elevation. Data from global HYCOM reanalysis is used.
n) elev2D.th.nc: time series of subtidal water level at the ocean boundary. Data from global HYCOM reanalysis is used.
o) SAL_3D.th.nc and TEM_3D.th.nc: time series data for salinity and temperature at the ocean boundary. Data from global HYCOM reanalysis is used.
p) SAL_nu.nc and TEM_nu.nc: time series data for salinity and temperature in the nudging zone. Data from global HYCOM reanalysis is used.
q) source.nc: source/sink file specifying the volume, temperature, and salinity for freshwater inputs. Data from USGS/NOAA gauging stations is used.
r) sflux: a directory containing the atmospheric forcings for wind, air pressure, precipitation, humidity, and solar radiation. For hindcast simulation, NARR is used.
s) param.nml: main parameter input file.

More information regarding the model input files can be found in the SCHISM manual (available at https://ccrm.vims.edu/schismweb/SCHISM_v5.9-Manual.pdf; https://schism-dev.github.io/schism/master/index.html).

## 4.1 Input file for river discharge (source.nc)

The model domain (Fig. 2.4) includes 29 rivers. For each river, we obtained freshwater inflow data from the corresponding USGS stations (available at https://waterdata.usgs.gov/). To address

missing data at a given USGS station, we used interpolation based on information from nearby USGS stations within 200 km. We first filled data gaps using data from the nearby station with the strongest linear relationship. If gaps still remained, we used data from stations with weaker linear relationships. Only stations with linear relationship with $R^2$ greater than 0.8 were used.

In the model, river inputs are treated as point sources. At each point source, data for volume flux, salinity (0 for freshwater) and water temperature are needed. The flow injection locations, along with the USGS gauging stations for flow and the USGS/NOAA stations for water temperature, are shown in Table 4.1. For the flow, the most downstream stations are selected. For some rivers, there are no USGS gauging stations. For these rivers, the freshwater inflow is calculated based on its watershed area relative to its neighboring river watershed. For instance, based on the ratio of watershed areas, the flow from Carancahua Creek is 12% of the flow from Lavaca River, and Caney Creek flow is 32% of the flow from San Bernard River. There could be resultant model bias when using freshwater input based on the watershed area ratio, but the impact from these rivers is mostly localized and minimal to the bay-wide conditions as these ungagged rivers are relatively small compared to major rivers discharging to the coastal bays. For water temperature, data from nearby USGS stations (within 100 km) with water temperature measurements are used. For those without a nearby USGS water temperature station, data at the NOAA station closest to the flow station are used.

**Table 4.1**: Freshwater inputs at major rivers included in the model.

| NO. | River Name | Lon | Lat | Flow station | Flow ratio | Temperature station | Note |
|---|---|---|---|---|---|---|---|
| 1 | San Fernando Creek | -97.773 | 27.401 | USGS08211900 | 1.00 | NOAA8776604 | |
| 2 | Nueces River | -97.605 | 27.869 | USGS08211200 | 1.00 | USGS08211200 | |
| 3 | RioGrand River | -97.290 | 25.936 | USGS08211900 | 1.00 | NOAA8776604 | Using San Fernando Creek |
| 4 | Aransas River | -97.284 | 28.095 | USGS08189700 | 1.00 | NOAA8774770 | |
| 5 | Mission River | -97.196 | 28.186 | USGS08189500 | 1.00 | NOAA8774770 | |
| 6 | Guadalupe River | -96.842 | 28.468 | USGS08188810 | 1.00 | NOAA8773037 | |
| 7 | Lavaca River | -96.576 | 28.870 | USGS08164000 | 1.00 | NOAA8773259 | |
| 8 | Carancahua Creek | -96.422 | 28.772 | USGS08164000 | 0.12 | NOAA8773146 | Ratio based on watershed |
| 9 | Tres Palacios River | -96.147 | 28.812 | USGS08162600 | 1.00 | NOAA8773146 | |
| 10 | Colorado River | -96.035 | 28.862 | USGS08162501 | 1.00 | NOAA8773146 | |
| 11 | Caney Creek | -95.670 | 28.829 | USGS08117705 | 0.32 | NOAA8773146 | Ratio based on watershed |
| 12 | San Bernard River | -95.557 | 28.951 | USGS08117705 | 1.00 | NOAA8773146 | |
| 13 | Brazos River | -95.530 | 29.036 | USGS08116650 | 1.00 | NOAA8773146 | |
| 14 | Buffalo Bayou | -95.355 | 29.762 | USGS08073600 | 1.00 | NOAA8770777 | |
| 15 | Chocolate Bayou | -95.229 | 29.260 | USGS08078000 | 1.00 | NOAA8771972 | |
| 16 | San Jancinto River | -95.131 | 29.918 | USGS08072000 | 1.00 | NOAA8770777 | |

| | | | | | | | |
|---|---|---|---|---|---|---|---|
| 17 | Clear Creek | -95.179 | 29.520 | USGS08076997 | 1.00 | NOAA8771013 | |
| 18 | Dickinson Bayou | -95.102 | 29.430 | USGS08076997 | 1.00 | NOAA8771013 | |
| 19 | Trinity River | -94.745 | 29.877 | USGS08067252 | 1.00 | USGS08067252 | |
| 20 | Neches River | -94.087 | 30.103 | USGS08041780 | 0.25 | NOAA8770475 | Ratio calibrated |
| 21 | Sabine River | -93.702 | 30.114 | USGS08030500 | 0.25 | NOAA8770475 | Ratio calibrated |
| 22 | Calcasieu River | -93.284 | 30.200 | USGS08015500 | 1.00 | NOAA8767961 | |
| 23 | Atchafalaya River | -91.490 | 30.040 | USGS07381490 | 1.00 | USGS07381600 | |
| 24 | Mississippi River | -91.198 | 30.491 | USGS07374000 | 1.00 | USGS07374000 | |
| 25 | Pearl River | -89.638 | 30.287 | USGS02489500 | 1.00 | NOAA8747437 | |
| 26 | Alabama River | -87.952 | 31.115 | USGS02428400 | 1.00 | NOAA8737048 | To Mobile Bay |
| 27 | Tombigbee River | -87.952 | 31.115 | USGS02469761 | 1.00 | NOAA8737048 | To Mobile Bay |
| 28 | Fish River | -87.810 | 30.443 | USGS02378500 | 1.00 | NOAA8737048 | |
| 29 | Bon Secour River | -87.709 | 30.319 | USGS02378500 | 0.50 | NOAA8737048 | Ratio based on watershed |

## 4.2 Input files for ocean boundary condition

### 4.2.1 Tide

At the ocean boundary, FES2014 (Carrere et al. 2015), a global tide product, is used to specify the tidal harmonic constants (tidal phase and amplitude) for 8 tidal constituents, including O1, K1, Q1, P1, M2, S2, K2, and N2. Among these 8 tidal constituents, O1 and K1 (both diurnal tides) are dominant in the model domain, having a much larger amplitude compared to those of semidiurnal tides (M2 and S2) (Fig. 4.1). We specify not only the surface elevation but also the tidal velocity (both eastward and northward components from FES2014) along the ocean boundary. The tidal boundary condition can be found in the file bctides.in.

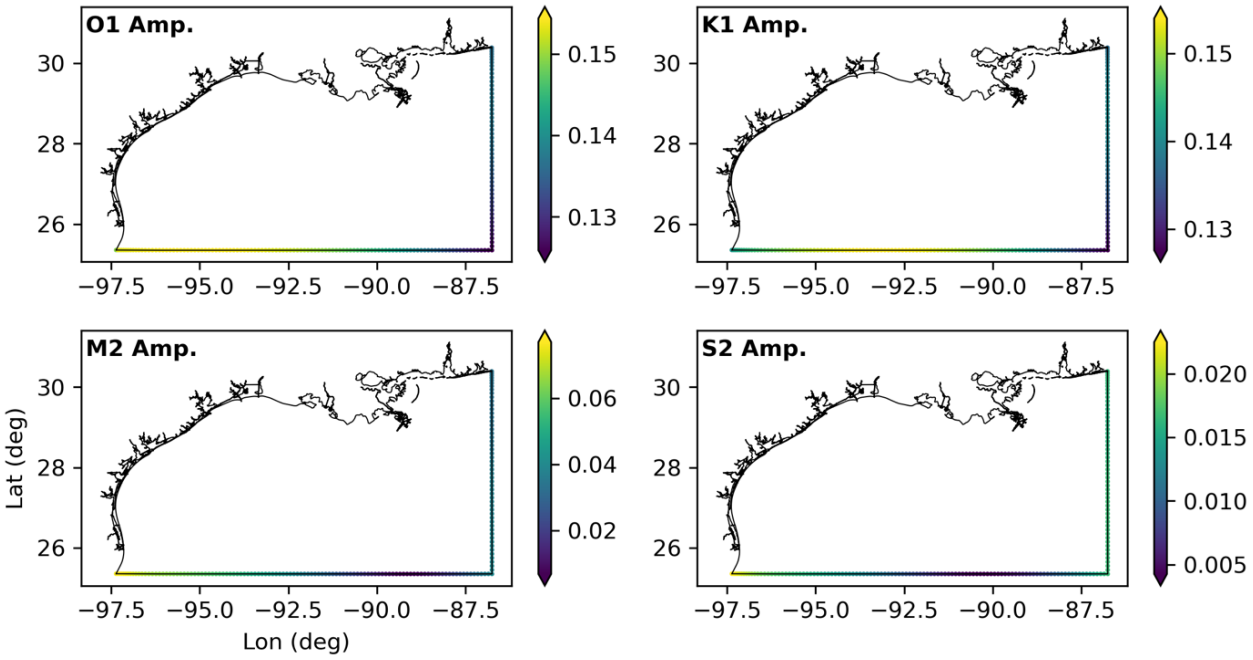

**Figure 4.1**: O1, K1, M2, and S2 amplitude for surface elevation along the open boundary (from FES2014). Note the different color scales (unit: m) for different tidal constituents.

### 4.2.2 Subtidal components

In addition to the tidal components, the model also includes the subtidal components at the open boundary. Global HYCOM reanalysis products (1/12 degree resolution; data available at https://www.hycom.org) are used to specify the subtidal surface elevation, water temperature, and salinity at the open boundary (Fig. 4.2). Water temperature and salinity are specified for all vertical layers along the ocean boundary. A low-pass filter with a cut-off period of 50 h is used to remove high-frequency variations in the 3-h HYCOM data.

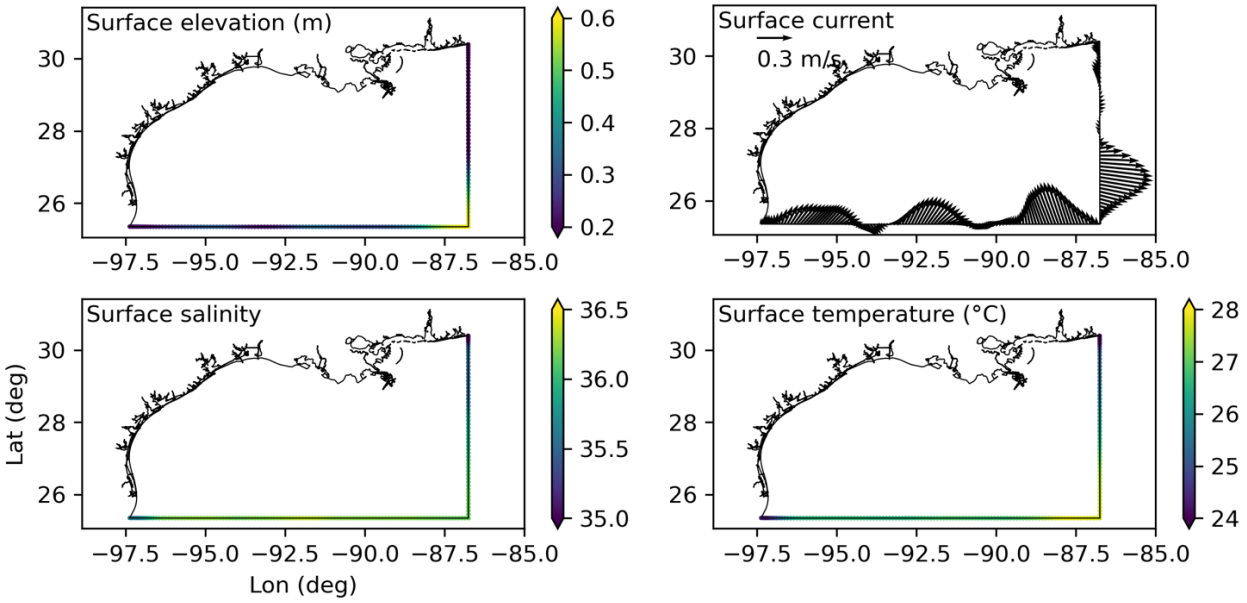


**Figure 4.2**: Mean (average for 2 years in 2018-2019) surface elevation, surface current, surface salinity, and surface temperature along the open boundary (from HYCOM).

### 4.2.3 Nudging for salinity and temperature

When enforcing the model boundary condition, a nudging scheme for both temperature and salinity is commonly applied in ocean modeling to prevent the simulated boundary values from becoming quite different from specified open boundary conditions (Chen et al. 2013). A nudging term is necessary when the wave or flow propagates outward from the model domain of interest to radiate instability near the boundary. A nudging zone of ~50 km from the ocean boundary is applied, with a larger nudging coefficient (faster adjustment) near the boundary (Fig. 4.3).

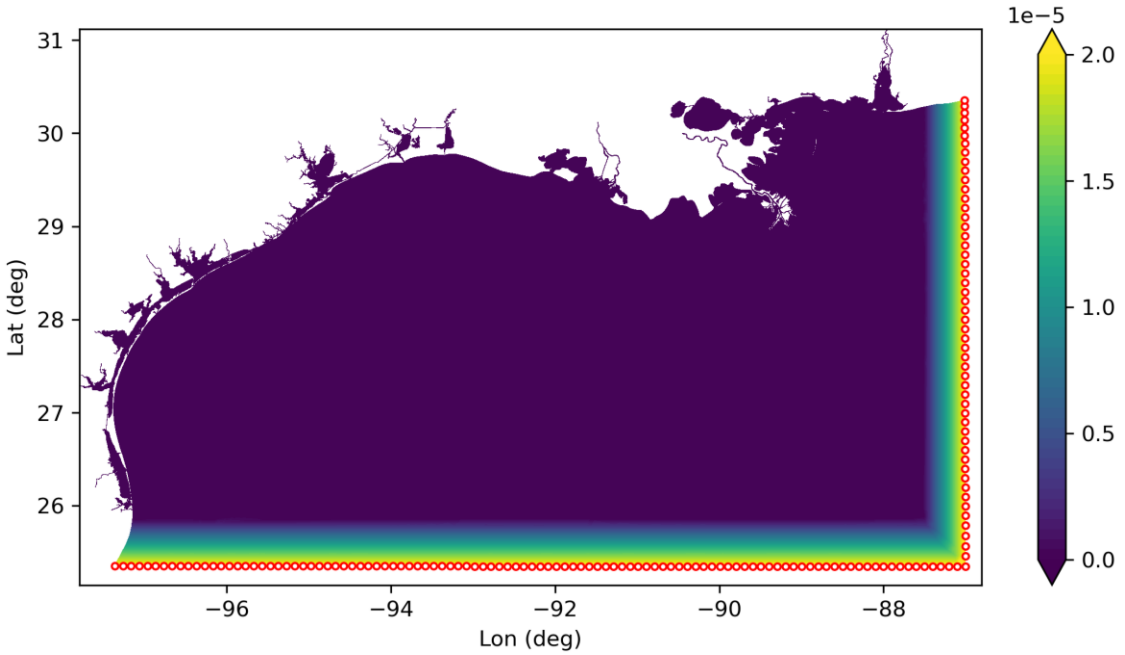


**Figure 4.3**: Nudging coefficient (filled color) in the nudging zone. Marked with red open circles are the open boundary nodes.

## 4.3 Input file for atmospheric forcing

For the hindcast simulations (Section 6), the NCEP North American Regional Reanalysis (NARR; https://psl.noaa.gov/data/gridded/data.narr.html) data is used for atmospheric forcing, including eastward/northward wind speeds at 10 m above ground, air pressure at sea surface, humidity at 2 m above ground, air temperature at 2 m above ground, short-wave and long-wave solar radiation flux, and precipitation. The NARR has a resolution of 0.3 degrees (~32 km) and a temporal coverage since 1979. The reanalysis product is updated monthly.

## 4.4 Python package for preparing model input files

The TAMU modeling team has created a number of Python scripts to prepare model input files. The Python scripts listed in Table 4.2 are available at https://github.com/JiabiDu/texas_schism. The two major ones are those to convert 2dm files (from mesh generation software Aquaveo SMS) to SCHISM-needed horizontal grid and to generate forcing-related input files.

**Table 4.2**: Python scripts for the preparation of model input files.

| Python script | Purpose | Major prerequisites |
|---|---|---|
| **gen_grid.py*** | Generate horizontal and vertical grids | • 2dm file from SMS<br>• DEM data |
| **master_setup.py*** | Generate all needed input files for a simulation | • Grid files (generated by gen_grid.py)<br>• River flow data<br>• Temperature measurements at rivers<br>• Subsets of Global HYCOM data for salinity, temperature, water level, and velocity |

| | | |
|---|---|---|
| | | • Global tide product, FES2014<br>• Atmospheric reanalysis data from NARR |
| download_hycom.py | Download subsets of Global HYCOM data | NA |
| get_gap_free_usgs_flow.py | Download USGS flow at selected stations and interpolate the data gaps | NA |
| get_usgs_noaa_temp.py | Download water temperature data at selected USGS and NOAA stations | NA |
| get_narr_sflux.py | Download NARR reanalysis data and convert the data into format needed by SCHISM | NA |

* indicates two most important Python scripts used to prepare input files for the SCHISM model.

# 5 Model outputs

The model generates 2D outputs for variables that do not have vertical variability (e.g., surface elevation, surface solar radiation, and vertical mean velocity) as well as 3D outputs. All 2D variables are stored in out2d_*.nc files, while each 3D variable is stored in [variable]_*.nc (e.g., salinity_1.nc, salinity_2.nc, temperature_1.nc, and temperature_2.nc). User can define the model output frequency and the number of records in each netCDF file.

## 5.1 Python package for processing output files

Table 5.1 lists Python scripts (available at https://github.com/JiabiDu/texas_schism), including two major ones, to process the model output files. In using mextract.py, we suggest using a parallel mode to extract data from the model outputs for computational efficiency. When using 96 cores on TAMU supercomputer Grace, it takes ~100 sec to extract 2-year salinity data for 200+ stations with different longitude, latitude, or depth from 730 output files.

**Table 5.1**: Python scripts for processing model output files.

| Python script | Purpose | Major prerequisites |
|---|---|---|
| **mextract.py*** | Extract data at selected stations from model outputs files | • Monitoring station locations<br>• Python package *mpi4py* for parallel purpose |
| **mplot.py*** | Generate plots showing the model performance in water level, salinity, temperature, and velocity | • Data files from the above script<br>• Observation data |
| check_velocity.py | Check velocity; find out abnormal locations | |
| check_ssh.py | Check water level; find out abnormal locations | |
| check_salt.py | Check salinity | |
| plot_model_grid.py | Plot model grid | |
| make_SSS_animation.py | Make sea surface salinity animations | |
| dash_water_level.py | Create a dashboard for interactively visualizing the model outputs | • Extracted water level data at selected stations<br>• Observation data for water level |

* indicates two important Python scripts used to process model outputs files.

## 5.2 Interactive dashboard to visualize model output

We have also developed a dashboard (based on Python) to visualize the modeled water level interactively. The dashboard comprises an interactive map on the left, where the user can zoom in/out and click the station of interest (Fig. 5.1). Contents in the right panels, showing total, subtidal (residual), and tidal components of water level, will be updated automatically after the user clicks a station. The tool is handy when examining the model performance since there are numerous gauging stations in Texas coastal waters. The dashboard can be easily modified to handle other model outputs, such as salinity. This dashboard is a local product that is not

currently available on the web, but the Python script for this dashboard is available at https://github.com/JiabiDu/texas_schism.

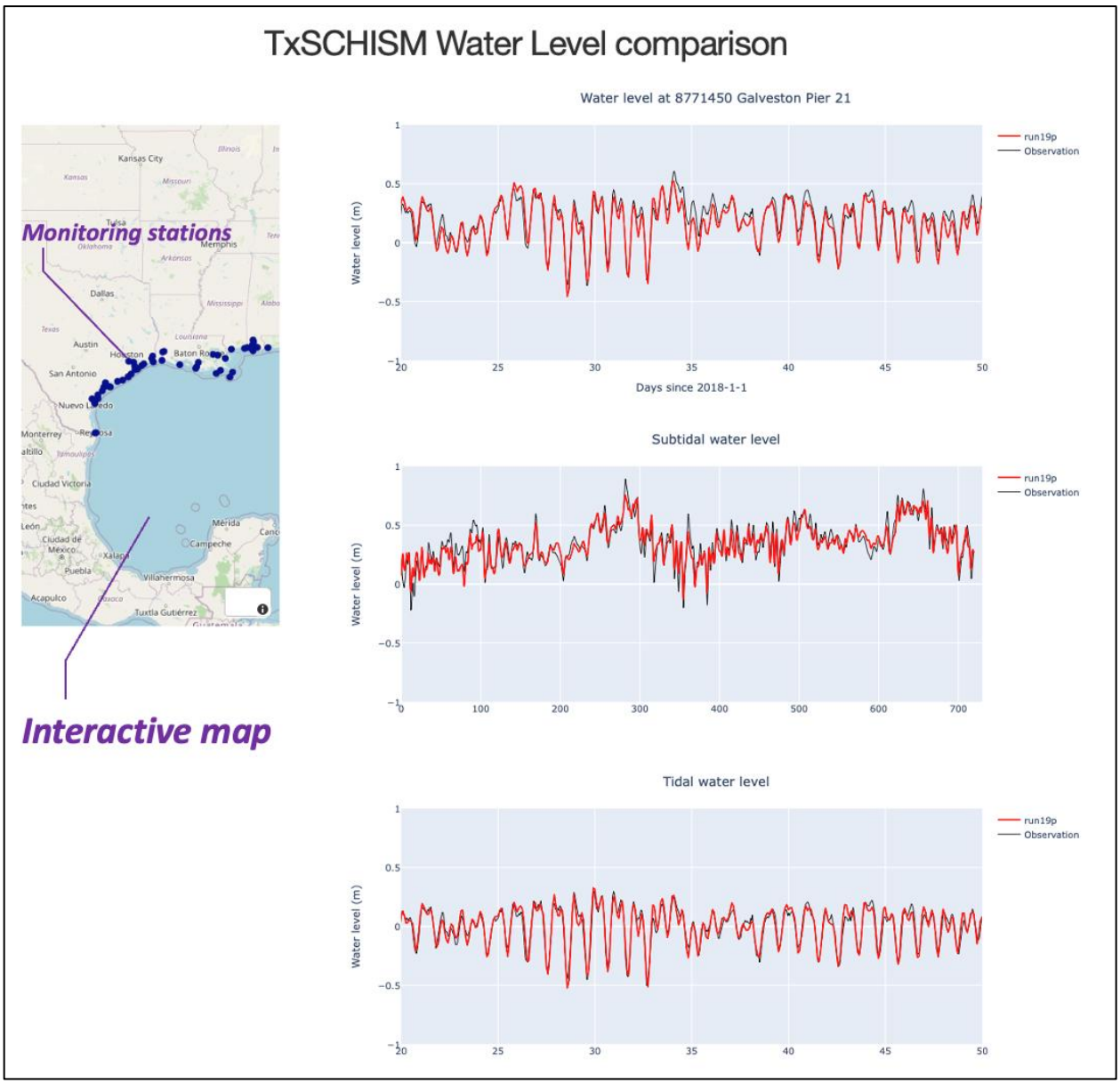


**Figure 5.1**: Dashboard to compare the model results (red line) and observations (black line) for total, subtidal, and tidal components of water level.

# 6 Model calibration

The model has been calibrated to reproduce observed water level, current velocity, salinity, and temperature. Numerous numerical experiments have been carried out to find the best model configuration. Model grids (horizontal and vertical grids) have been optimized considering the model's accuracy and computational efficiency. Key model parameters (e.g., bottom friction formula, transport scheme, and evaporation option) are tuned. Table 6.1 lists major model configurations for the final product.

With these settings, the model still runs efficiently. It takes about 18 hours to finish a one-year simulation with 384 cores at Grace, an Intel x86-64 Linux cluster at Texas A&M University. The computational cost highly depends (nearly linearly related) on the grid size and the number of vertical layers.

**Table 6.1**: Key model configurations.

| Item | Setup | Note |
|---|---|---|
| Number of segments across ship channel | 4 segments for deep channels (between two 10 m isobaths) and 2 segments between 5 and 10 m isobaths | To better resolving the bathymetric feature across the channel |
| Grid resolution | 10 km in deep Gulf (depth > 200 m), 2-5 km on shelf, and ~ 500 m inside bays (except the channels) | Using 10 km in the deep Gulf for better computational efficiency. |
| Vertical Grid | $LSC^2$ with minimum of 10 layers. Mean number of sigma layers: 16 | Little difference when applying larger minimum layers. |
| Bottom friction | Using a constant drag coefficient (0.0025) | Better than using Manning coefficient when dealing with wetting and drying. Using Manning coefficient will lead to abnormal large velocities when the total water depth is small. |
| Precipitation and evaporation | On | Important in Laguna Madre |
| Initial condition | 3D fields in the coastal ocean from global HYCOM and inside the bays using previous model simulations | 3-h HYCOM results are low pass filtered with a cut off period of 50 h. |
| Water level at ocean boundary | Harmonic + subtidal variations from global HYCOM | |
| Salinity and temperature at ocean boundary | From global HYCOM; low-pass filter is applied, with a cut-off period of 50 hr. | |
| Velocity at ocean boundary | Harmonic + subtidal variations from global HYCOM | |
| Nudging zone near the ocean boundary | ~50 km | |
| Tracer transport method | Second order TVD | itr_met=3 in param.nml |

The model was initially calibrated for 2007-2008 (Du et al. 2019) and has also been tested for Hurricane Harvey (Du and Park 2019). For this project, we chose more recent years (2018-2019), during which more data, such as the tidal current data and USGS gauging data for

freshwater flow, are available. Sensitivity tests regarding the model configurations have been carried out for a two-year period (2018-2019). Taking the horizontal grid as example, whenever some changes are made, a numerical simulation was carried out to ensure that the model's reliability and performance were not compromised. The remainder of this section presents the model performance in terms of water level, velocity, salinity, and temperature.

Observational data for water level, velocity, salinity, and temperature are from several sources (Table 6.2 and Fig. 6.1). The data, usually in csv or ascii format, were compiled with Python scripts. We used the available data and did not attempt to further clean up the data. For water level, salinity, and shelf current data, we use a low-pass filter with cut-off period of 50 h to isolate the tidal and subtidal signals. Subtidal here refers to the remaining signal after removing the tidal signal. In the Texas coastal bays, the major tidal signal is diurnal with a period of around 24 h.

**Table 6.2**: Observational data sources

| **Data** | **Source** | **URL** |
|---|---|---|
| Water level, water temperature, and tidal currents | NOAA | https://tidesandcurrents.noaa.gov<br>API: https://api.tidesandcurrents.noaa.gov/api/prod/ |
| Water salinity | TWDB | https://waterdatafortexas.org/coastal<br>https://www.waterdatafortexas.org/api |
| Shelf current | TABS | https://www.ndbc.noaa.gov<br>Buoy B: https://www.ndbc.noaa.gov/station_page.php?station=42043<br>Buoy F: https://www.ndbc.noaa.gov/station_page.php?station=42050 |

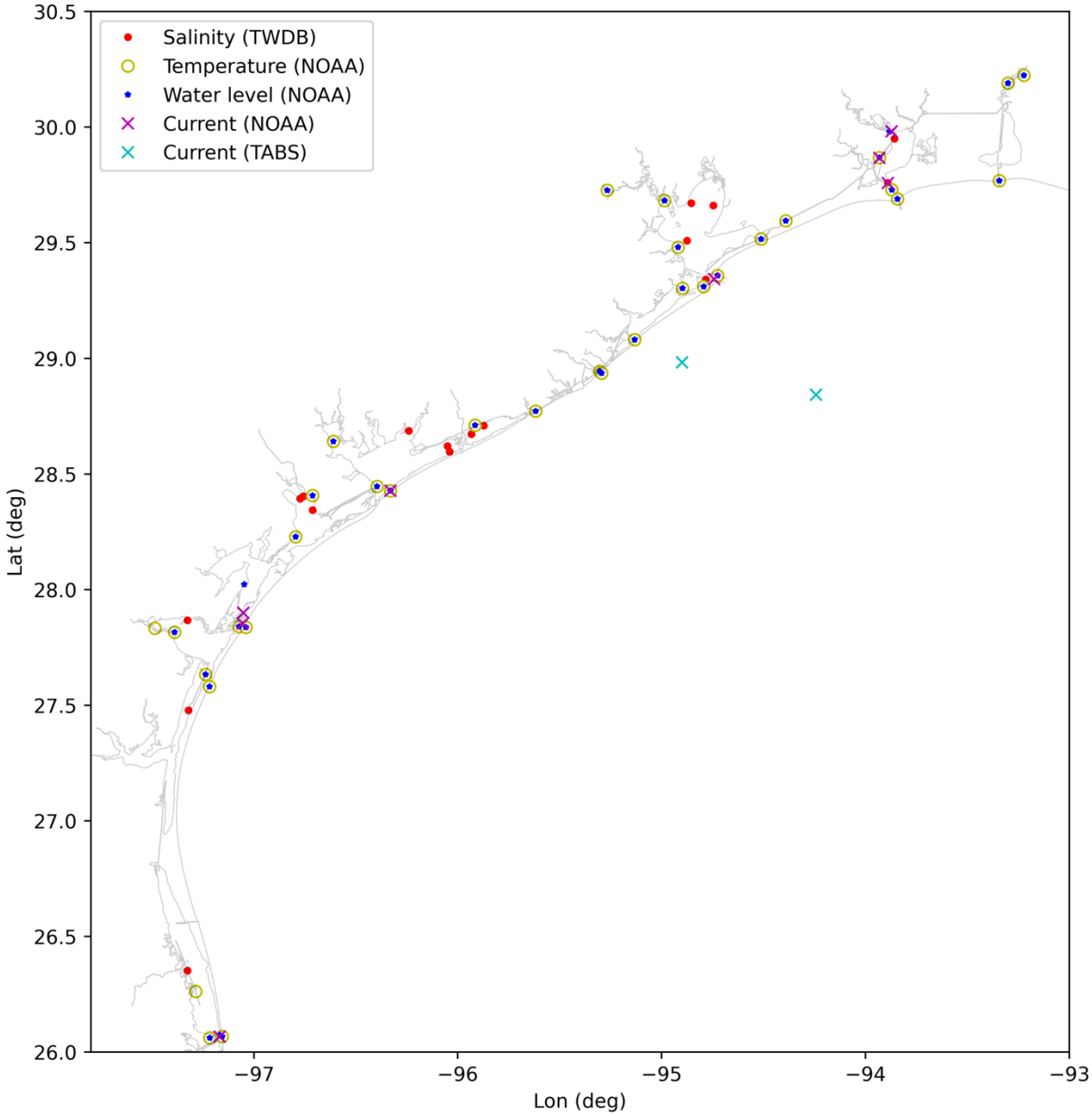


**Figure 6.1**: Locations of monitoring stations for water level, current velocity, salinity, and temperature compared with model results. The background grey lines denote the land boundary of the numerical model. Note that water level and water temperature are both measured at most NOAA stations. NOAA stations to the east of Sabine Lake (e.g., those in Louisiana, Mississippi, and Alabama) are not shown, even though they are used to calibrate the model as well. Locations of those stations can be found in the subset of model-observation comparison plots.

## 6.1 Water level

We compared the total, subtidal and tidal signals of water level at all available NOAA gauging stations (Figs. 6.2-6.4). Only some selected stations are shown here, with more stations in Appendix I. Overall, the model well reproduces the water level variations in both tidal and subtidal components along the Texas coast. The model performance is particularly outstanding in

Galveston Bay and Corpus Christi Bay, compared to stations in upper and lower Texas coastal waters (Fig. 6.1; more in the next paragraph). One highlight is the water level simulation inside Galveston Bay. The model well captures the variations in water level at both the bay mouth and the upper bay station, Morgan Point (Fig. 6.2). At Morgan Point, the water level is notably different from the bay mouth in terms of semi-diurnal signal (less semi-diurnal signal at Morgan Point) and subtidal variations.

One notable problem is the model persistently overestimates the water level by ~0.2 m at the southernmost Texas (e.g., station 8779749: SPI Brazos Santiago) and the northernmost Texas (e.g., station 8770822: Texas Point, Sabine Pass). Another issue is the persistent underestimation by ~0.2 m in Saint Antonio Bay (station 8773037 in Fig. A1.4). Several tuning efforts (e.g., changing the bottom friction formula and manning coefficient) have been made but without success. The discrepancies can be induced by bathymetry uncertainty, grid resolution, numerical errors, and uncertainty in vertical datum used at different stations along the coast. Future editions on the grid and tuning efforts are needed to improve the model performance.

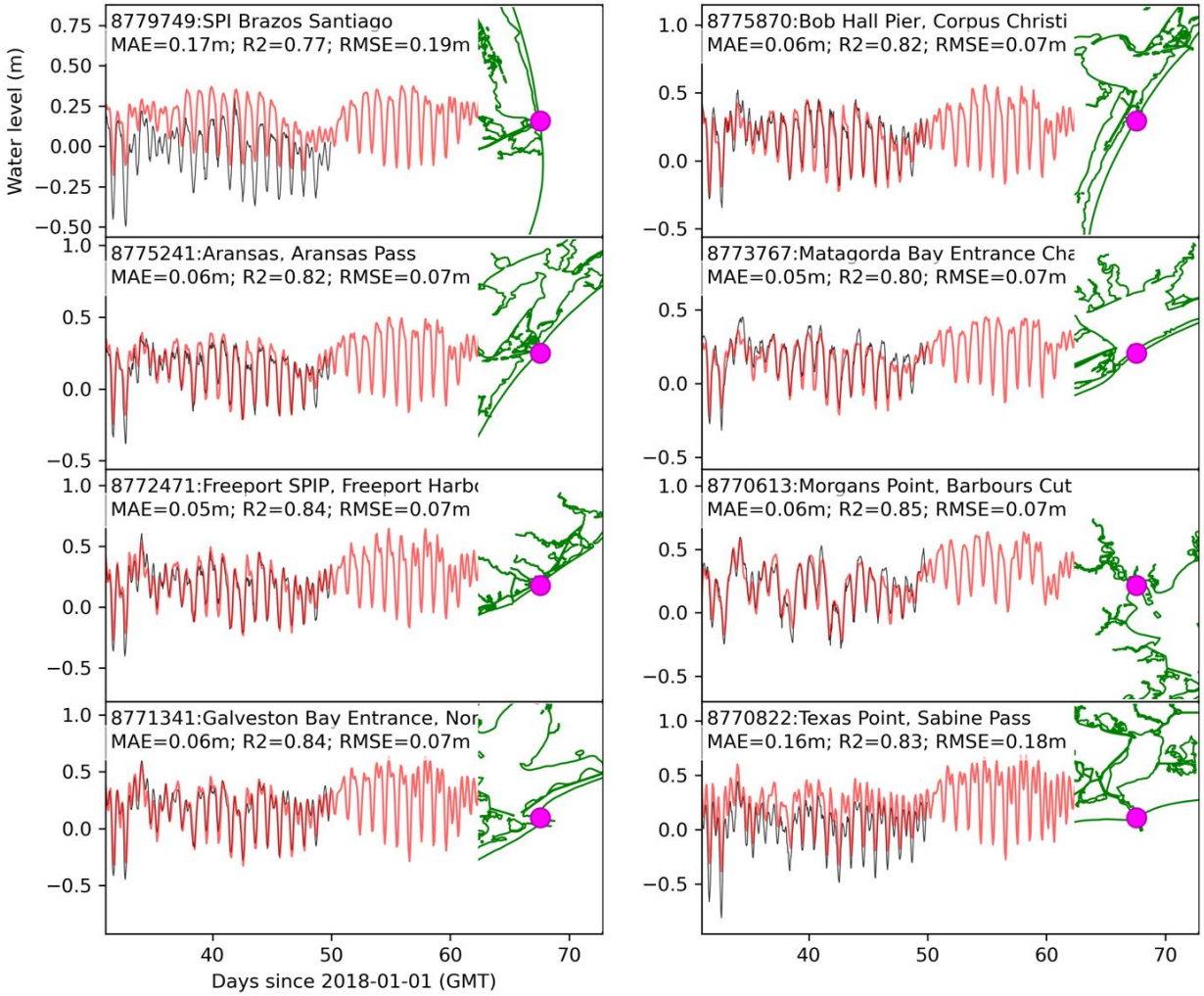


**Figure 6.2**: Water level comparison between model (red) and observation in NAVD88 datum (black) at selected stations along the Texas coast. Only 20-day (days 30 to 50 in 2018) results are shown here. Mean

absolute error (MAE), $R^2$, and root mean square error (RMSE) are shown at the top of each panel. The locations of the monitoring stations are marked with magenta dots on the right subsets.

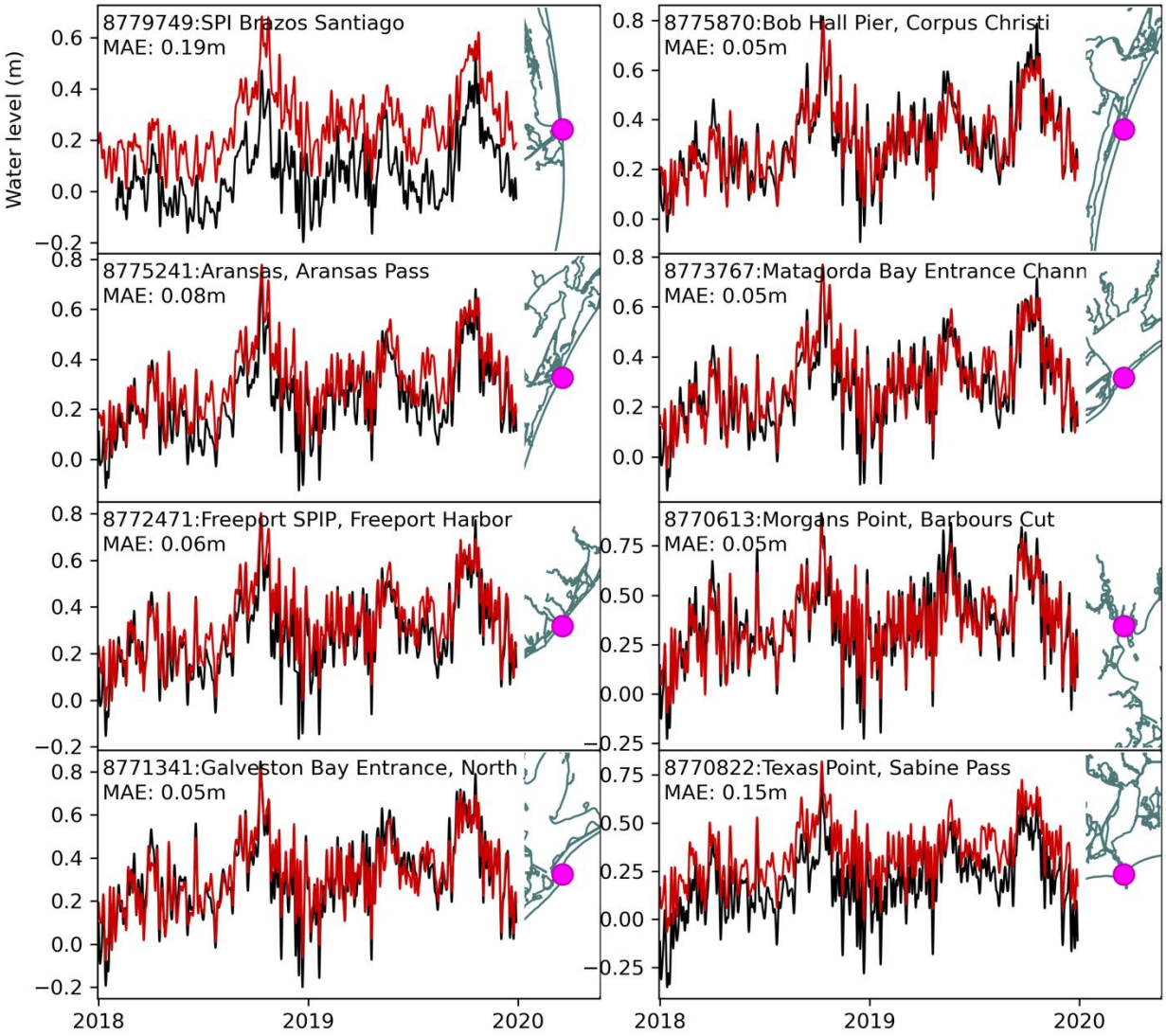


**Figure 6.3**: Comparison of subtidal water level between model (red) and observation in NAVD88 datum (black) at selected stations along the Texas coast. The locations of the monitoring stations are marked with magenta dots on the right subsets.

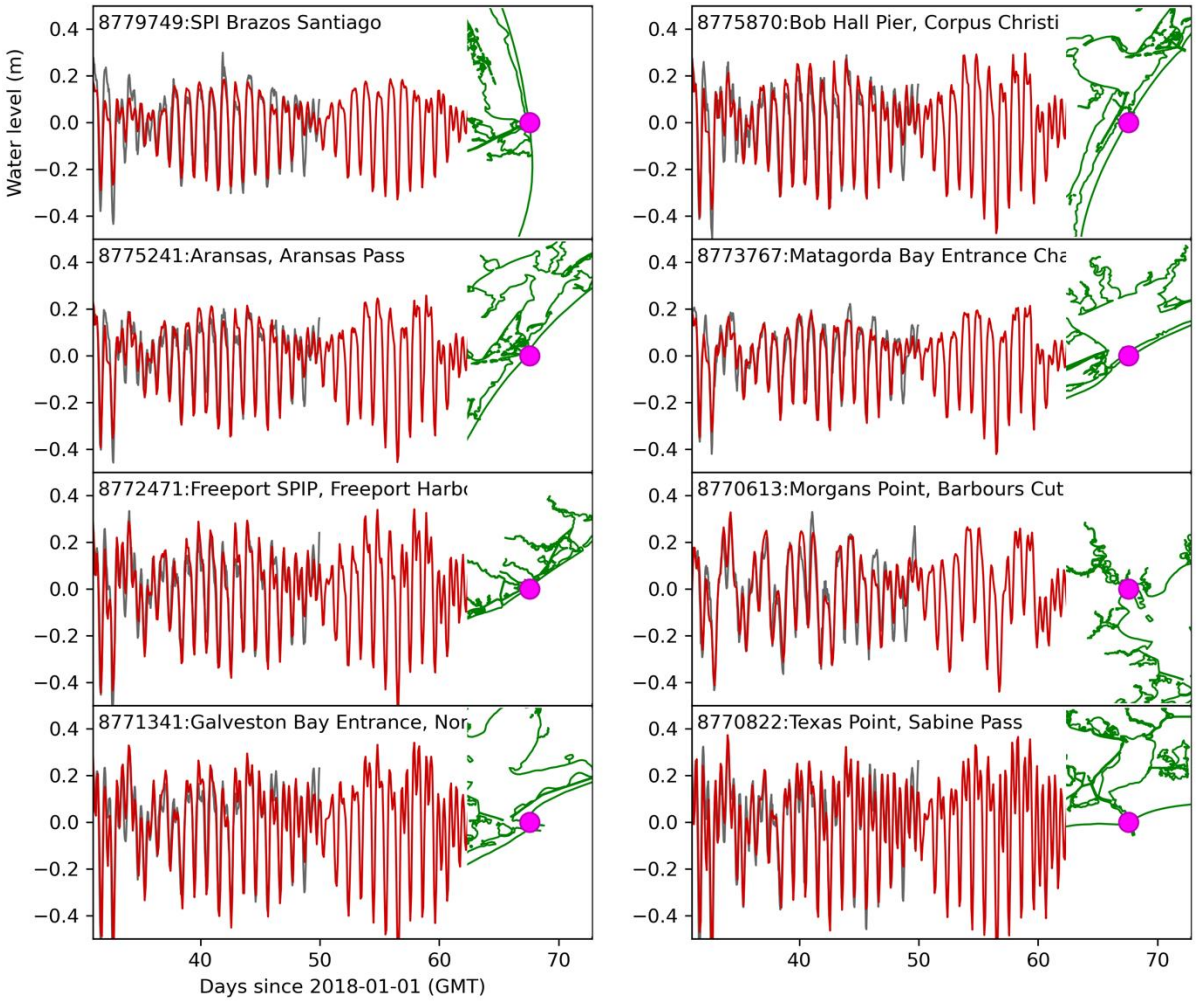


**Figure 6.4**: Comparison of tidal water level between model (red) and observation (black) at selected stations along the Texas coast. The locations of the monitoring stations are marked with magenta dots on the right subsets.

## 6.2 Velocity

We compared the current velocity at multiple stations along the Texas coast for both its eastward and northward components. Figures 6.5-6.6 show the eastward component only since the east-west direction is the dominant current orientation at these stations (except station STX1802 near Port Aransas). East velocity at two buoy stations off Galveston Bay (buoy B and F) was also compared with the model results (Figs. 6.7-6.8). Comparisons at other stations are shown in Appendix II.

The model captures both the variations of current magnitude and direction at the bay mouth stations. At the inner shelf stations, buoys B and F from Texas Automated Buoy System (TABS), the model also performs well in reproducing the overall low-frequency variations. A closer examination of the shelf current shows that the model overestimates the tidal variability, especially at buoy F. This discrepancy is likely related to the open boundary condition. Nevertheless, the tidal components on the shelf have a much smaller magnitude compared to the

subtidal components and thus will not significantly affect the net transport on the timescale of days.

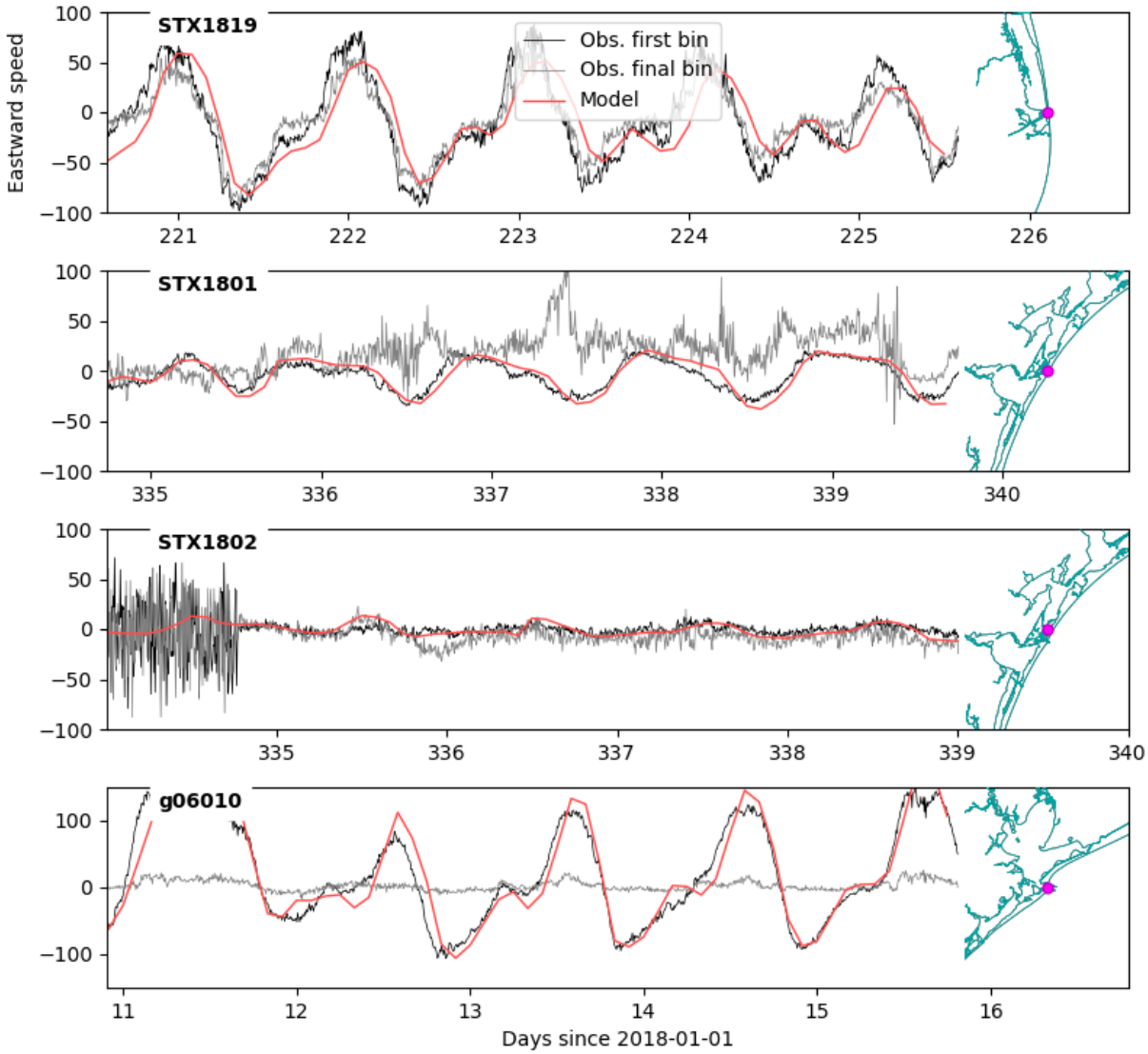


**Figure 6.5**: Comparison of eastward current velocity at selected NOAA stations (a zoom-in view for 5 days), with red lines indicating the model result while black and grey lines indicating the first and last bin of ADCP measurements. The locations of the monitoring stations are shown with magenta dots on the right subsets.

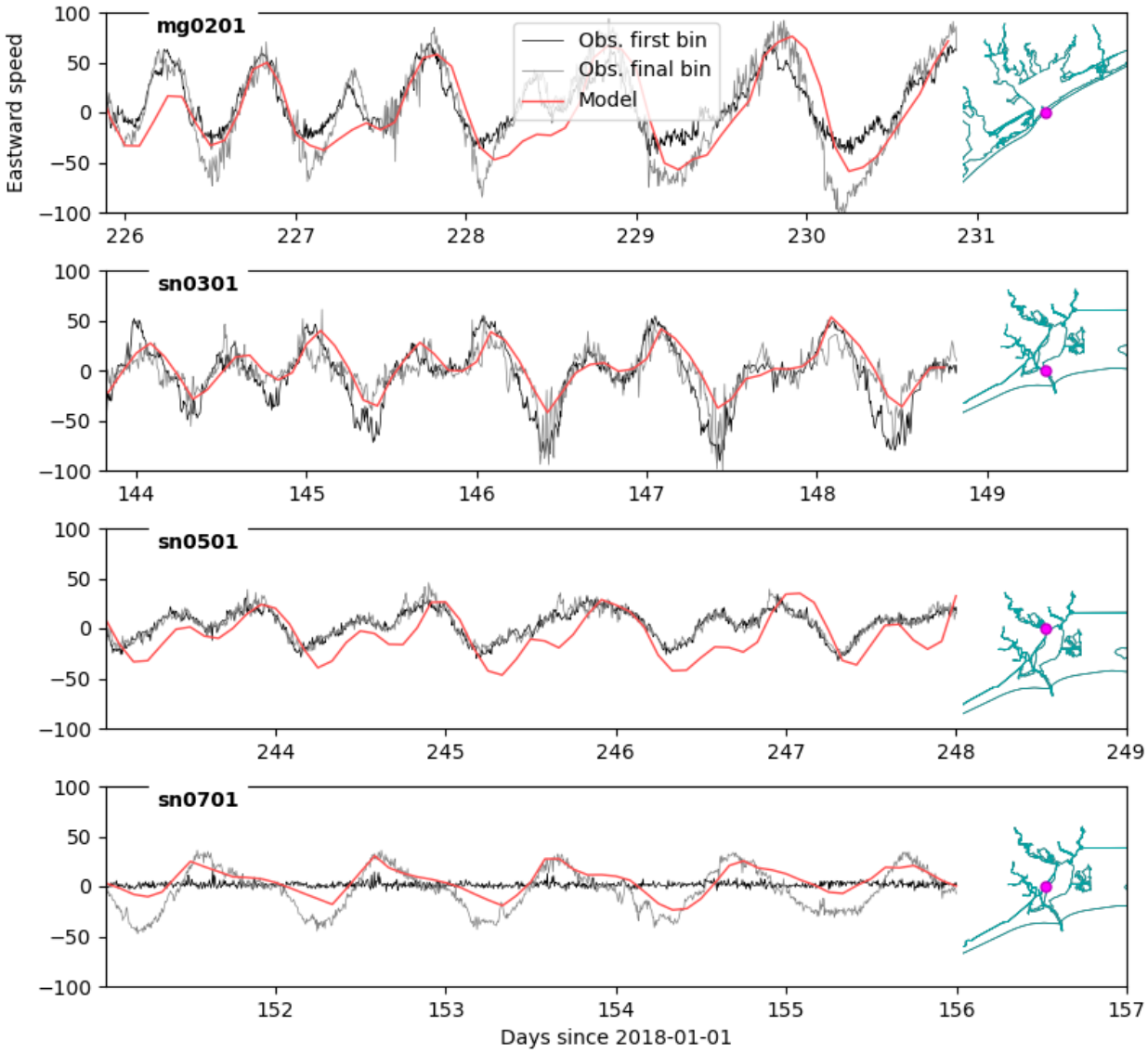


**Figure 6.6**: Comparison of eastward current velocity at selected NOAA stations (a zoom-in view for 5 days), with red lines indicating the model result while black and grey lines indicating the first and last bin of ADCP measurements. The locations of the monitoring stations are shown with magenta dots on the right subsets.

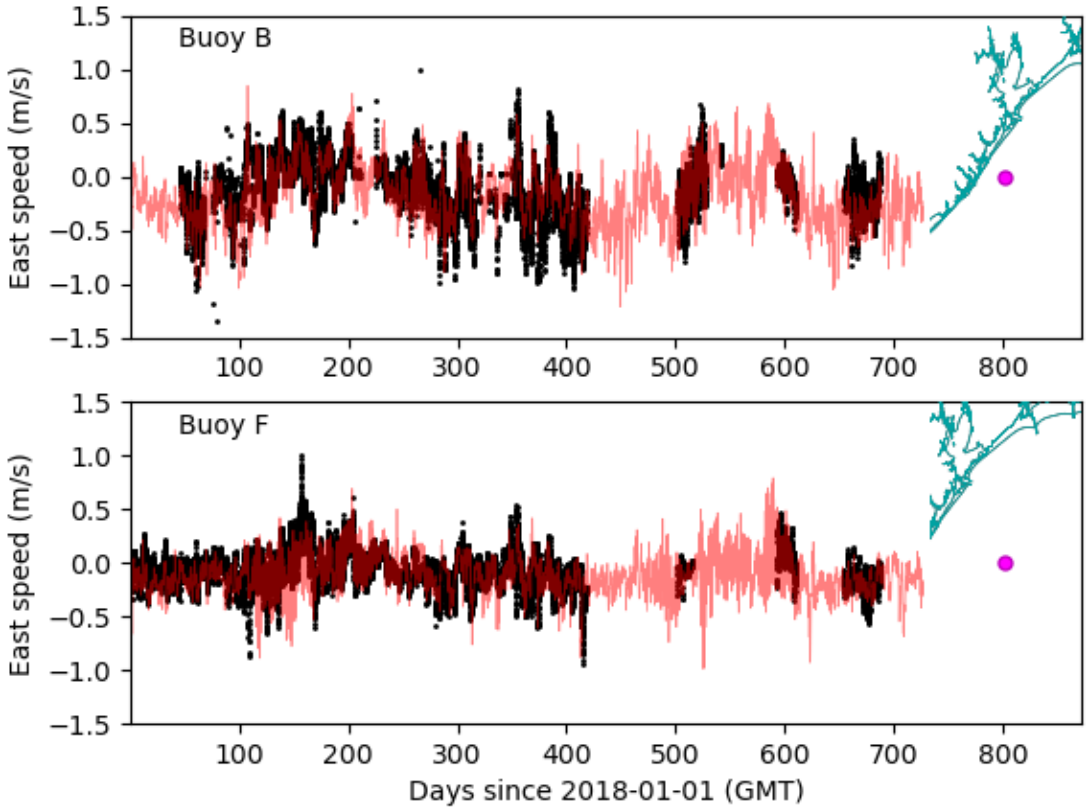


**Figure 6.7**: Comparison of eastward current velocity at TABS (https://tabs-web.geos.tamu.edu) buoys B and F, located 20 and 50 km off the Texas coastline, respectively. Black dots indicate the observation and red lines indicate the model results.

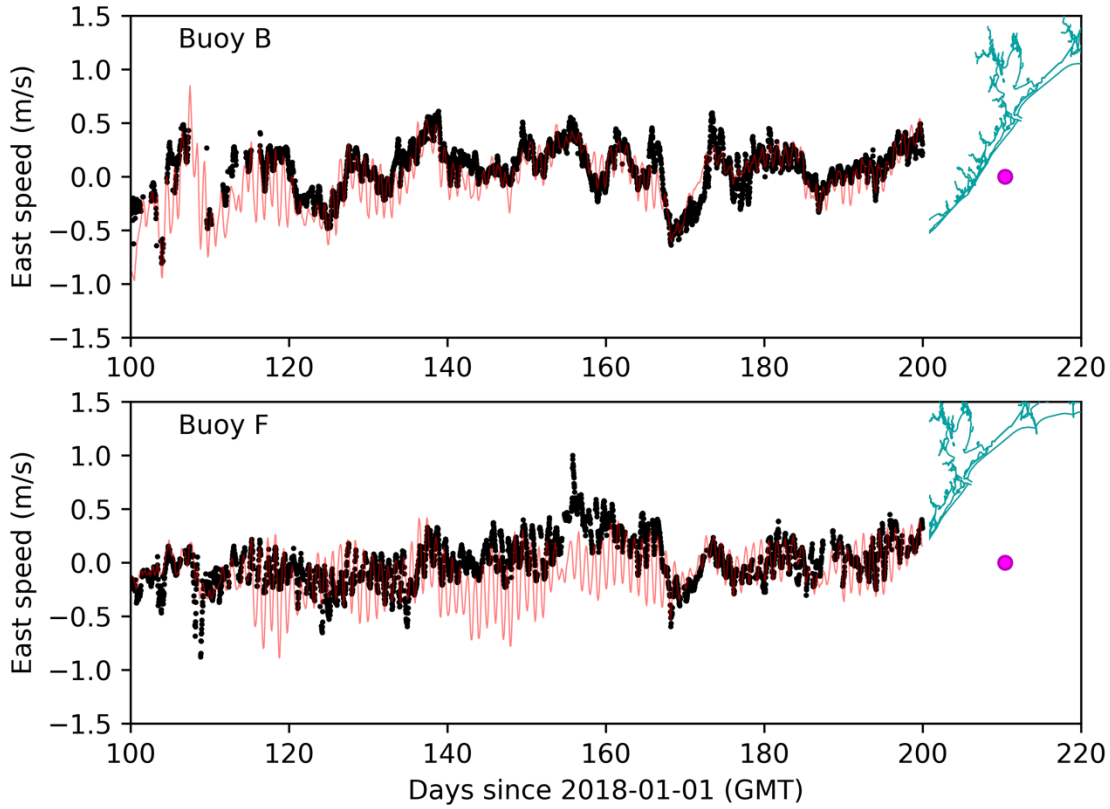


**Figure 6.8**: A zoom-in view of shelf current comparison for days 100-200 since 2018-01-01. Black dots indicate the observation and red lines indicate the model results.

## 6.3 Salinity

The most informative variable in hydrodynamic modeling for coastal waters is salinity. Accurate salinity simulation indicates the reliability of the model in simulating physical mass transport, which is the combined result of advective currents, diffusion and mixing processes, freshwater inputs, and coastal ocean dynamics. The model-data comparison for salinity is shown in Figs. 6.9-6.13 and Appendix III.

Overall, the model well reproduces the observed salinity variability along the Texas coast (Figs. 6.9-6.13). The performance is especially outstanding in Sabine Lake and Galveston Bay, where long-term high-quality salinity data are available. However, discrepancies are notable in Matagorda Bay and Laguna Madre, where freshwater input is very limited for most of the time and thus salinity is extremely sensitive to the accuracy of freshwater inputs. At some stations (e.g., see Figs. 6.11 and 6.13), the data show sudden decreases/increases over relatively short time periods, which the model cannot reproduce. These peaks in observed salinity are not likely real signals but rather sensor malfunction, possibly due to biofouling in highly productive bay waters.

The model is also capable of simulating the hypersaline condition in Laguna Madre, where salinity is frequently higher than normal seawater salinity. For instance, at station LMA2, the salinity is higher than that at the bay mouth station (SPCG; Fig. 6.13).

Using the current model configuration, we also conducted a long-term 20-year simulation. The model's reliability is confirmed by the good model-observation agreement in Galveston Bay for the 20-year simulation period (Fig. 6.14).

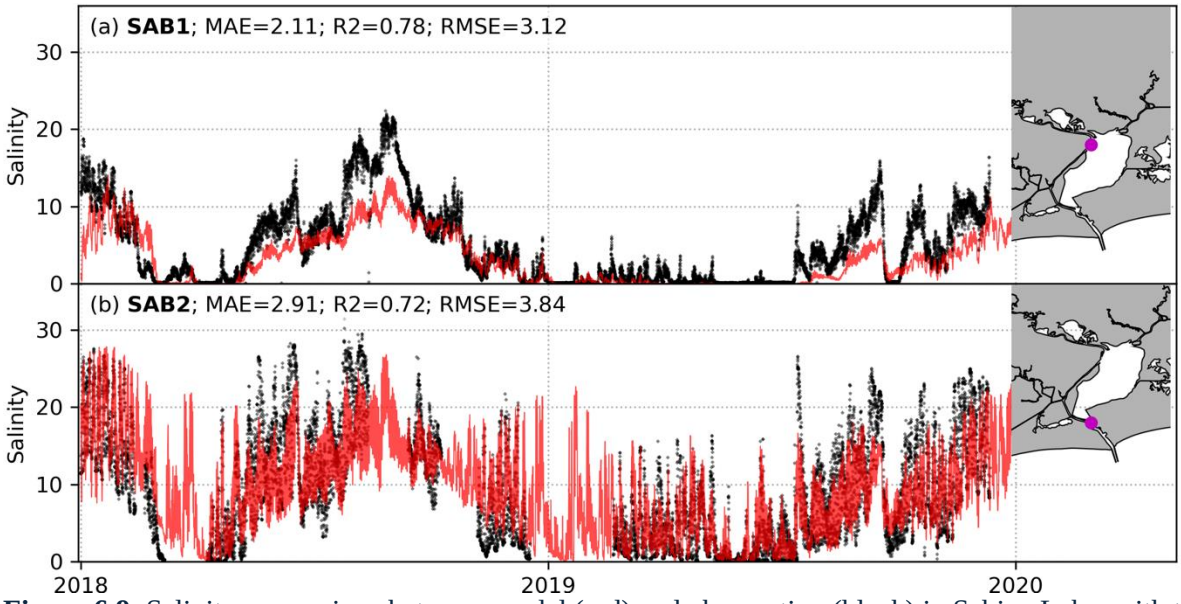


**Figure 6.9**: Salinity comparison between model (red) and observation (black) in Sabine Lake, with the mean absolute error (MAE), $R^2$, and root mean square error (RMSE) shown at the top of each panel. The locations of the monitoring stations are marked with magenta dots on the right subsets.

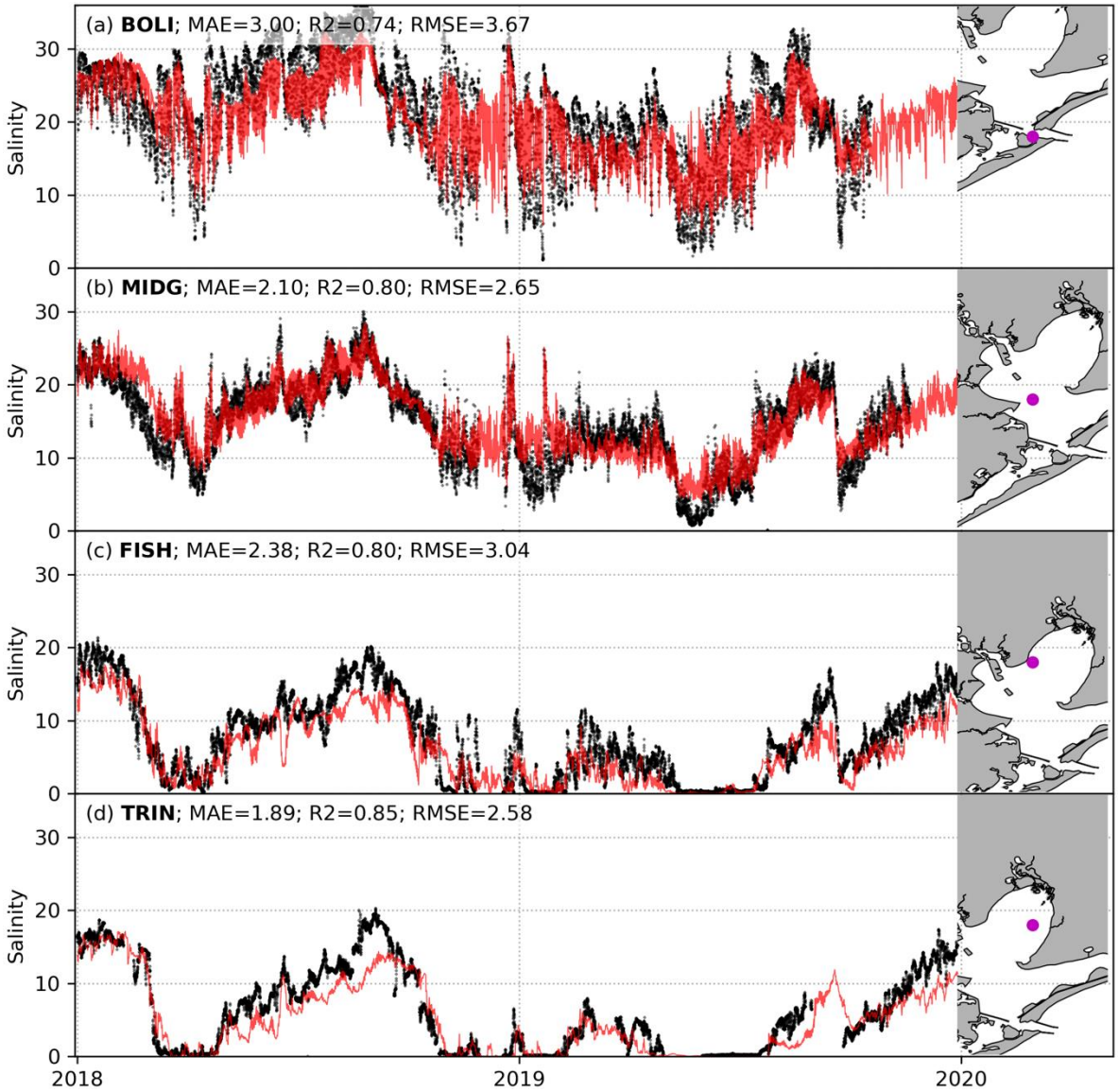


**Figure 6.10**: Salinity comparison between model (red) and observation (black) in Galveston Bay, with mean absolute error (MAE), $R^2$, and root mean square error (RMSE) shown at the top of each panel. The locations of the monitoring stations are marked with magenta dots on the right subsets.

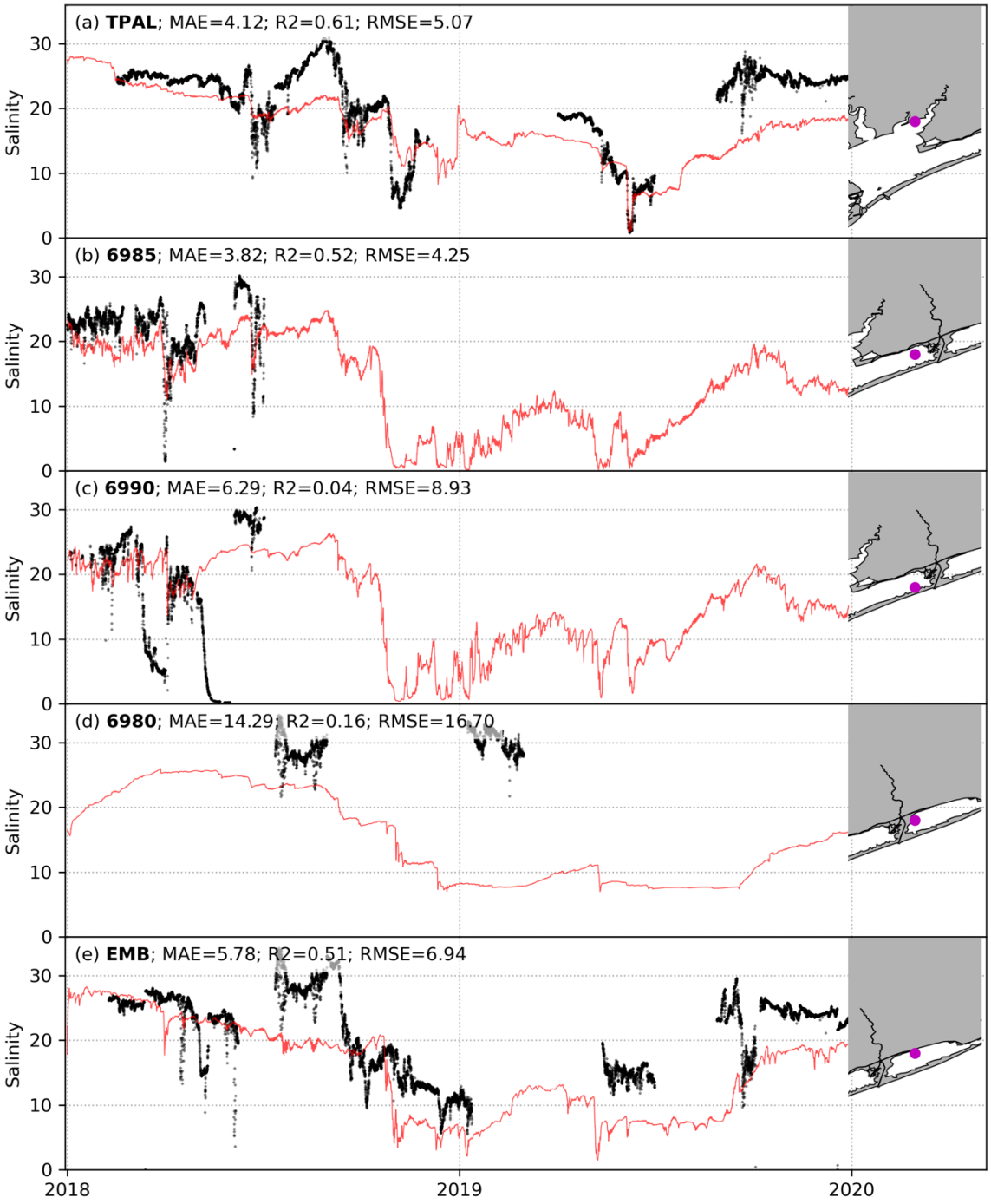


**Figure 6.11**: Salinity comparison between model (red) and observation (black) in East Matagorda and Matagorda Bays, with mean absolute error (MAE), $R^2$, and root mean square error (RMSE) shown at the top of each panel. The locations of the monitoring stations are marked with magenta dots on the right subsets.

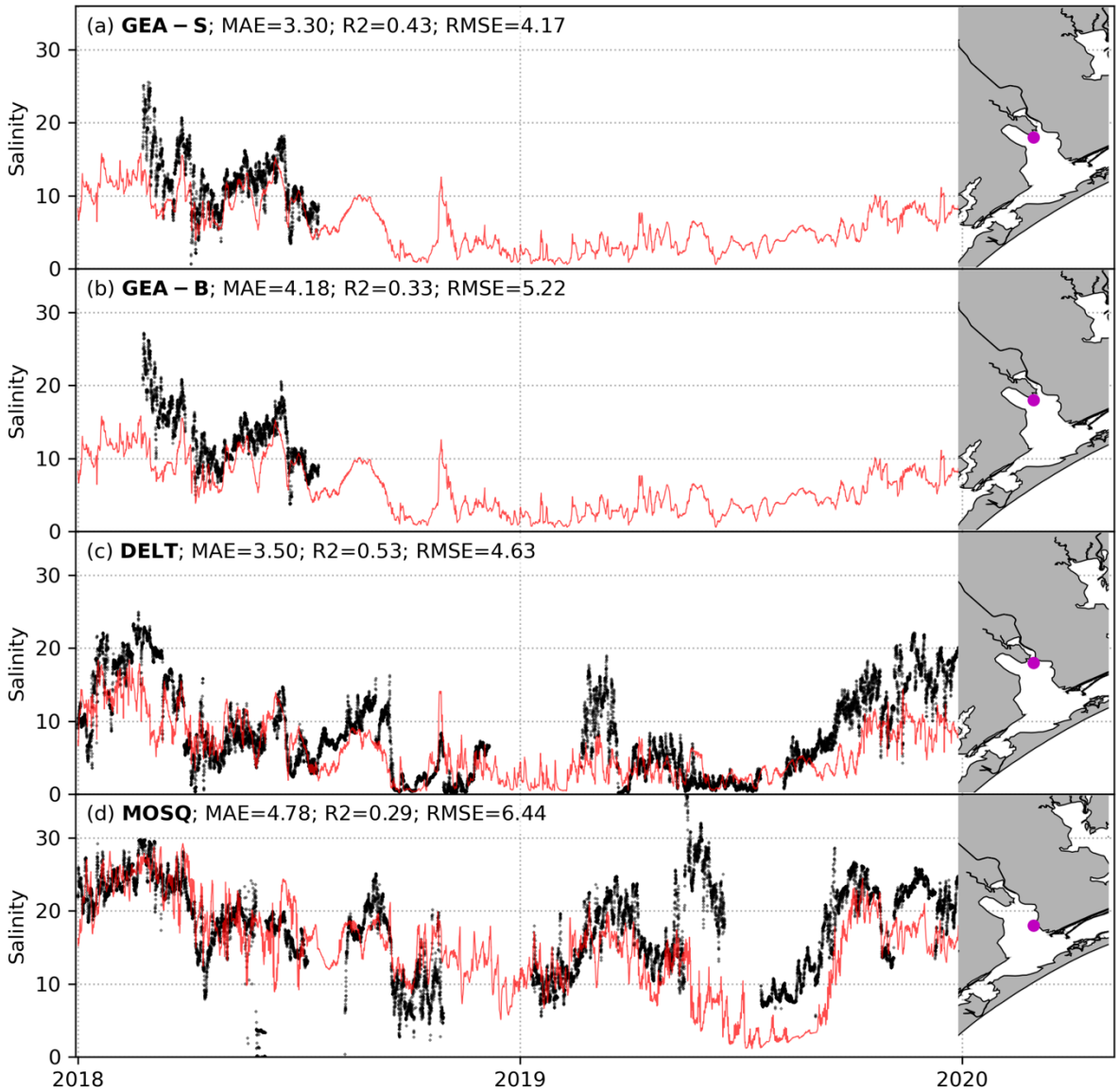


**Figure 6.12**: Salinity comparison between model (red) and observation (black) in Saint Antonio Bay, with mean absolute error (MAE), $R^2$, and root mean square error (RMSE) shown at the top of each panel. The locations of the monitoring stations are marked with magenta dots on the right subsets.

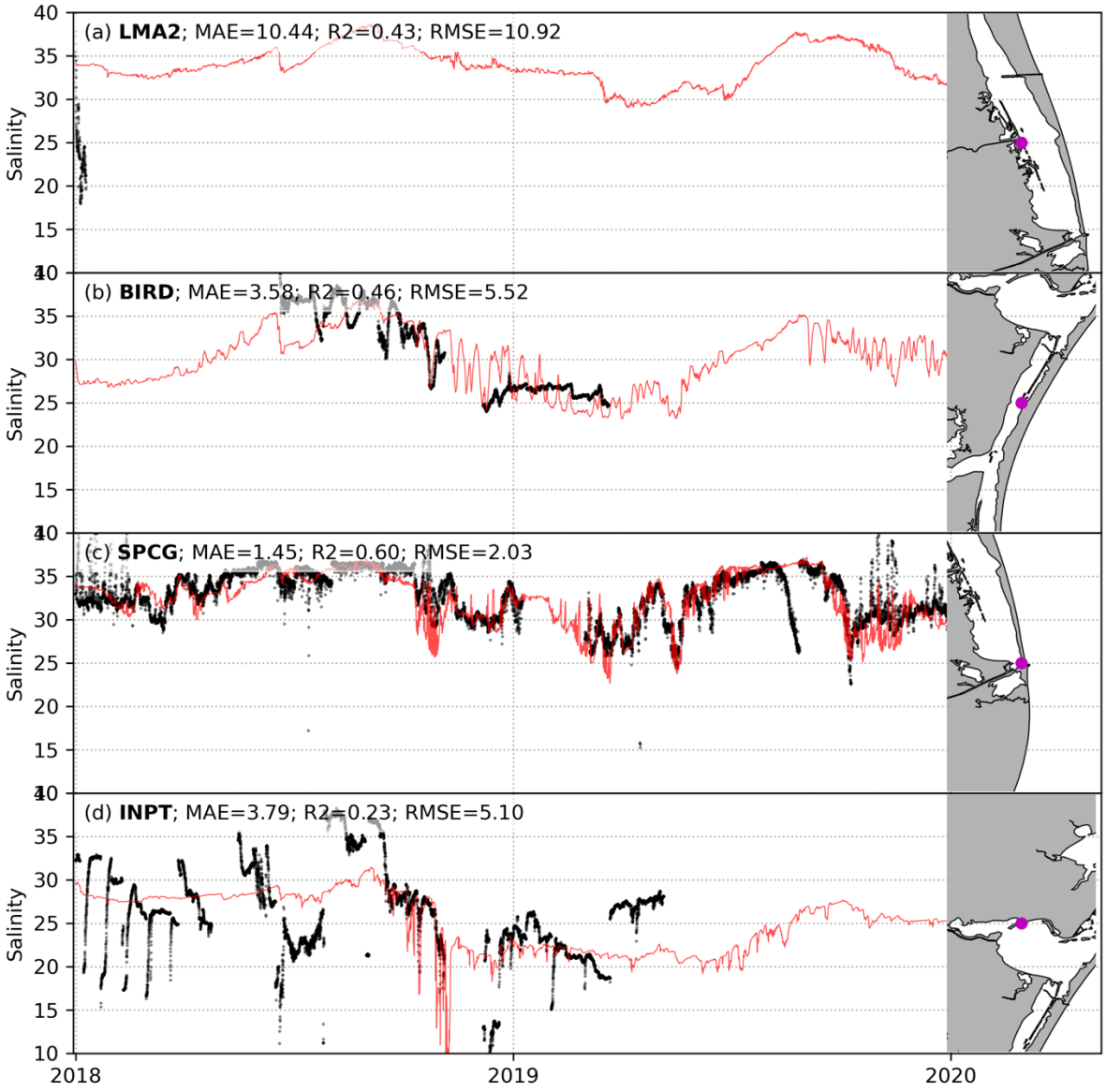


**Figure 6.13**: Salinity comparison between model (red) and observation (black) in Corpus Christi Bay, and Lower and Upper Laguna Madre, with mean absolute error (MAE), $R^2$, and root mean square error (RMSE) shown at the top of each panel. The locations of the monitoring stations are marked with magenta dots on the right subsets.

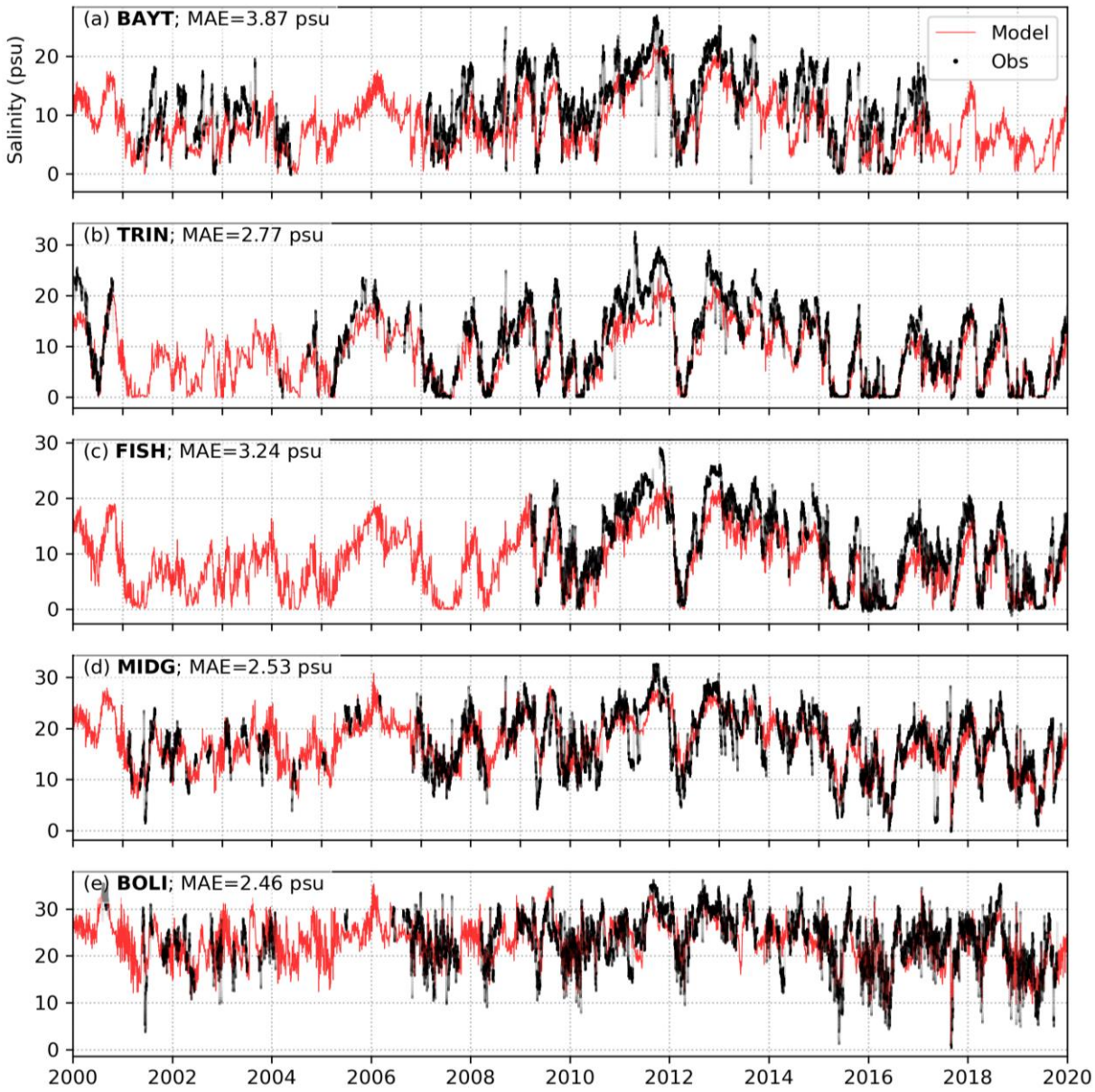


**Figure 6.14**: Subtidal salinity comparison between model (red) and observation (black) at multiple stations inside Galveston Bay from a long-term 20-year simulation, with mean absolute error (MAE) shown at the top of each panel.

## 6.4 Temperature

Compared to salinity, water temperature is less sensitive to model configuration but more reliant on the accuracy of atmospheric forcing. Comparisons at multiple stations along the Texas coast are shown in Fig. 15 and Appendix IV.

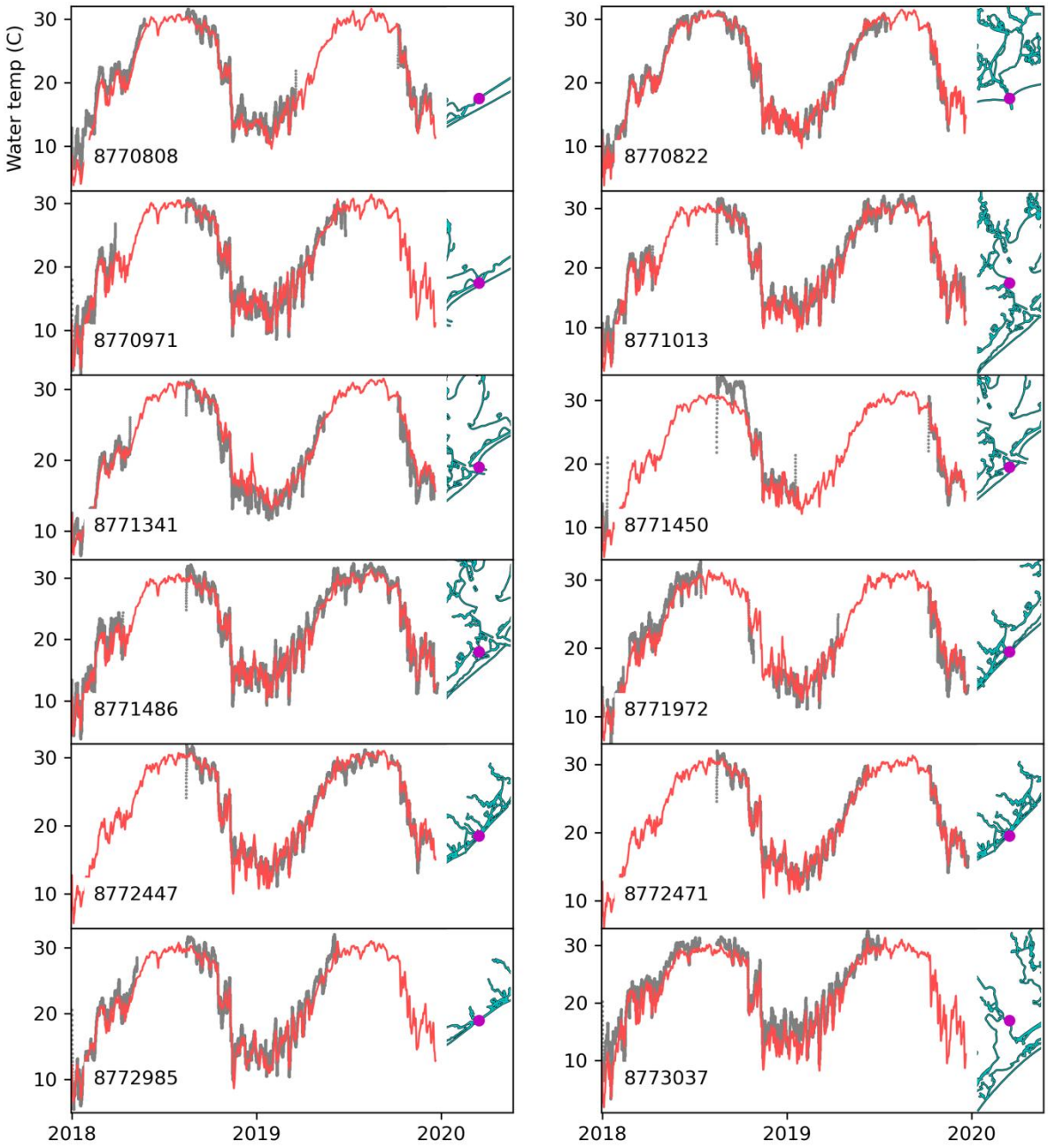


**Figure 6.15**: Temperature comparison between model (red) and observation (black) at NOAA gauging stations. The locations of the monitoring stations are marked with magenta dots on the right subsets.

# References


Amante, C. J., Love, M., Carignan, K., Sutherland, M. G., MacFerrin, M., & Lim, E. (2023). Continuously Updated Digital Elevation Models (CUDEMs) to support coastal inundation modeling. Remote Sensing, 15(6), 1702. https://doi.org/10.3390/rs15061702

Bruesewitz, D. A., Gardner, W. S., Mooney, R. F., Pollard, L., & Buskey, E. J. (2013). Estuarine ecosystem function response to flood and drought in a shallow, semiarid estuary: Nitrogen cycling and ecosystem metabolism. Limnology and Oceanography, 58(6), 2293–2309. https://doi.org/10.4319/lo.2013.58.6.2293

Buskey, E. J., Liu, H., Collumb, C., & Bersano, J. G. F. (2001). The decline and recovery of a persistent Texas brown tide algal bloom in the Laguna Madre (Texas, USA). Estuaries, 24(3), 337–346. https://doi.org/10.2307/1353236

Carrere, L., Lyard, F., Cancet, M., and Guillot, A. (2015): FES 2014, a new tidal model on the global ocean with enhanced accuracy in shallow seas and in the Arctic region, in: Abstracts of the EGU General Assembly 2015, Vienna, Austria, 12–17 April 2015. http://adsabs.harvard.edu/abs/2015EGUGA..17.5481C

Chen, X., Liu, C., O'Driscoll, K., Mayer, B., Su, J., & Pohlmann, T. (2013). On the nudging terms at open boundaries in regional ocean models. Ocean Modelling, 66, 14–25. https://doi.org/10.1016/j.ocemod.2013.02.006

Dellapenna, T. M., Hoelscher, C., Hill, L., Critides, L., Salgado, V., Bell, M., Al Mukaimi, M. E., Du, J., Park, K., & Knap, A. H. (2022). Hurricane Harvey delivered a massive load of mercury-rich sediment to Galveston Bay, TX, USA. Estuaries and Coasts, 45, 428–444. https://doi.org/10.1007/s12237-021-00990-7

Du, J., & Park, K. (2019). Estuarine salinity recovery from an extreme precipitation event: Hurricane Harvey in Galveston Bay. Science of The Total Environment, 670, 1049–1059. https://doi.org/10.1016/j.scitotenv.2019.03.265

Du, J., Park, K., Shen, J., Zhang, Y. J., Yu, X., Ye, F., et al. (2019). A hydrodynamic model for Galveston Bay and the shelf in the northern Gulf of Mexico. Ocean Science, 15(4), 951–966. https://doi.org/10.5194/os-15-951-2019

Du, J., Park, K., Yu, X., Zhang, Y. J., & Ye, F. (2020). Massive pollutants released to Galveston Bay during Hurricane Harvey: Understanding their retention and pathway using Lagrangian numerical simulations. Science of The Total Environment, 704, 135364. https://doi.org/10.1016/j.scitotenv.2019.135364

Hodges, B. R., Kulis, P. S., & David, C. H. (2006). Desalination Brine Discharge Model. Final Report to Texas Water Development Board, Center for Research in Water Resources, University of Texas at Austin. https://www.twdb.texas.gov/publications/reports/contracted_reports/doc/2005001059_DesalinationBrine.pdf.

Huang, W., Ye, F., Zhang, Y. J., Park, K., Du, J., Moghimi, S., et al. (2021). Compounding factors for extreme flooding around Galveston Bay during Hurricane Harvey. Ocean Modelling, 158, 101735. https://doi.org/10.1016/j.ocemod.2020.101735

Kim, B., Sanders, B. F., Schubert, J. E., & Famiglietti, J. S. (2014). Mesh type tradeoffs in 2D hydrodynamic modeling of flooding with a Godunov-based flow solver. Advances in Water Resources, 68, 42–61. https://doi.org/10.1016/j.advwatres.2014.02.013

Lopez, A. M., Fitzsimmons, J. N., Adams, H. M., Dellapenna, T. M., & Brandon, A. D. (2022). A time-series of heavy metal geochemistry in sediments of Galveston Bay estuary, Texas, 2017-2019. Science of The Total Environment, 806, 150446. https://doi.org/10.1016/j.scitotenv.2021.150446

MacCready, P. (2004). Toward a unified theory of tidally-averaged estuarine salinity structure. Estuaries, 27(4), 561–570. https://doi.org/10.1007/BF02907644

Santschi, P. H., Presley, B. J., Wade, T. L., Garcia-Romero, B., & Baskaran, M. (2001). Historical contamination of PAHs, PCBs, DDTs, and heavy metals in Mississippi River Delta, Galveston Bay and Tampa Bay sediment cores. Marine Environmental Research, 52(1), 51–79. https://doi.org/10.1016/S0141-1136(00)00260-9

Steffen, C., Stephens, S., Dance, M. A., Lippi, D. L., Jensen, C. C., Wells, R. J. D., & Rooker, J. R. (2023). Estuarine-coastal connectivity and partial migration of southern flounder in the Gulf of Mexico. Estuarine, Coastal and Shelf Science, 294, 108545. https://doi.org/10.1016/j.ecss.2023.108545

Summers, E., Du, J., Park, K., & Kaiser, K. (2024). Quantifying the Connectivity of Microplastic Pollution in the Texas–Louisiana Coastal Area. ACS ES&T Water, 4(6), 2482–2494. https://doi.org/10.1021/acsestwater.3c00839

Thyng, K. M., Hetland, R. D., Ogle, M. T., Zhang, X., Chen, F., & Campbell, L. (2013). Origins of Karenia brevis harmful algal blooms along the Texas coast. Limnology and Oceanography: Fluids and Environments, 3(1), 269–278. https://doi.org/10.1215/21573689-2417719

Thyng, K. M., & Hetland, R. D. (2017). Texas and Louisiana coastal vulnerability and shelf connectivity. Marine Pollution Bulletin, 116(1), 226–233. https://doi.org/10.1016/j.marpolbul.2016.12.074

Williams, A. K., Bacosa, H. P., & Quigg, A. (2017). The impact of dissolved inorganic nitrogen and phosphorous on responses of microbial plankton to the Texas City “Y” oil spill in Galveston Bay, Texas (USA). Marine Pollution Bulletin, 121(1), 32–44. https://doi.org/10.1016/j.marpolbul.2017.05.033

Ye, F., Zhang, Y. J., Wang, H. V., Friedrichs, M. A. M., Irby, I. D., Alteljevich, E., et al. (2018). A 3D unstructured-grid model for Chesapeake Bay: Importance of bathymetry. Ocean Modelling, 127, 16–39. https://doi.org/10.1016/j.ocemod.2018.05.002

Zhang, Y. J., Ateljevich, E., Yu, H.-C., Wu, C. H., & Yu, J. C. S. (2015). A new vertical coordinate system for a 3D unstructured-grid model. Ocean Modelling, 85, 16–31. https://doi.org/10.1016/j.ocemod.2014.10.003

Zhang, Y. J., Ye, F., Stanev, E. V., & Grashorn, S. (2016). Seamless cross-scale modeling with SCHISM. Ocean Modelling, 102, 64–81. https://doi.org/10.1016/j.ocemod.2016.05.002

Zhu, J., Weisberg, R. H., Zheng, L., & Han, S. (2015). On the flushing of Tampa Bay. Estuaries and Coasts, 38(1), 118–131. https://doi.org/10.1007/s12237-014-9793-6

# Appendix I: Water level comparison between model and observation

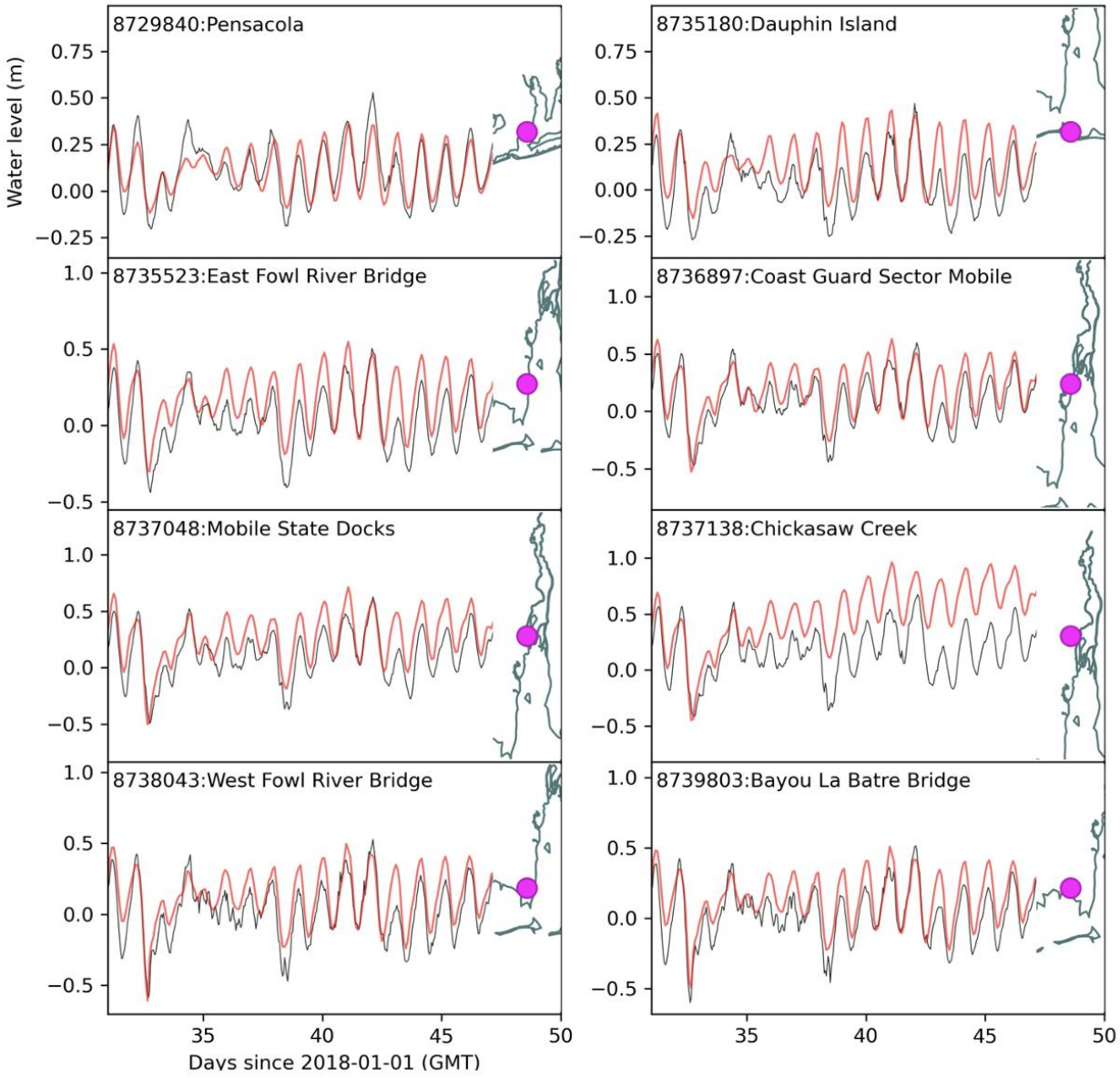


**Figure A1.1**: Water level (full signal) comparison between model (red) and observation (black) at selected stations for only a 30-day period (day 20 to 50 in 2018). The locations of the monitoring stations are marked with magenta dots on the right subsets.

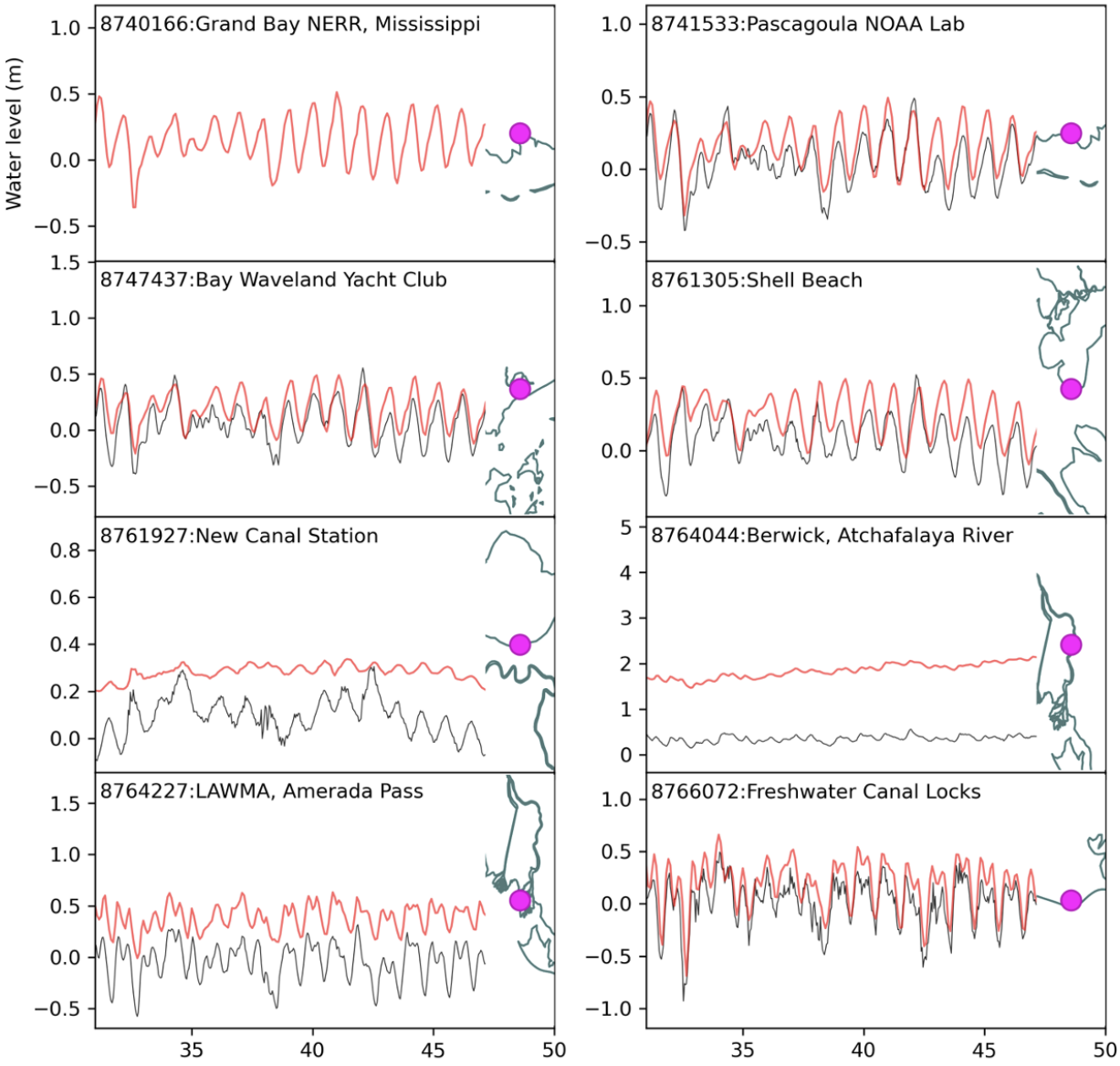


**Figure A1.2**: The same as Fig. A1.1, except for other locations.

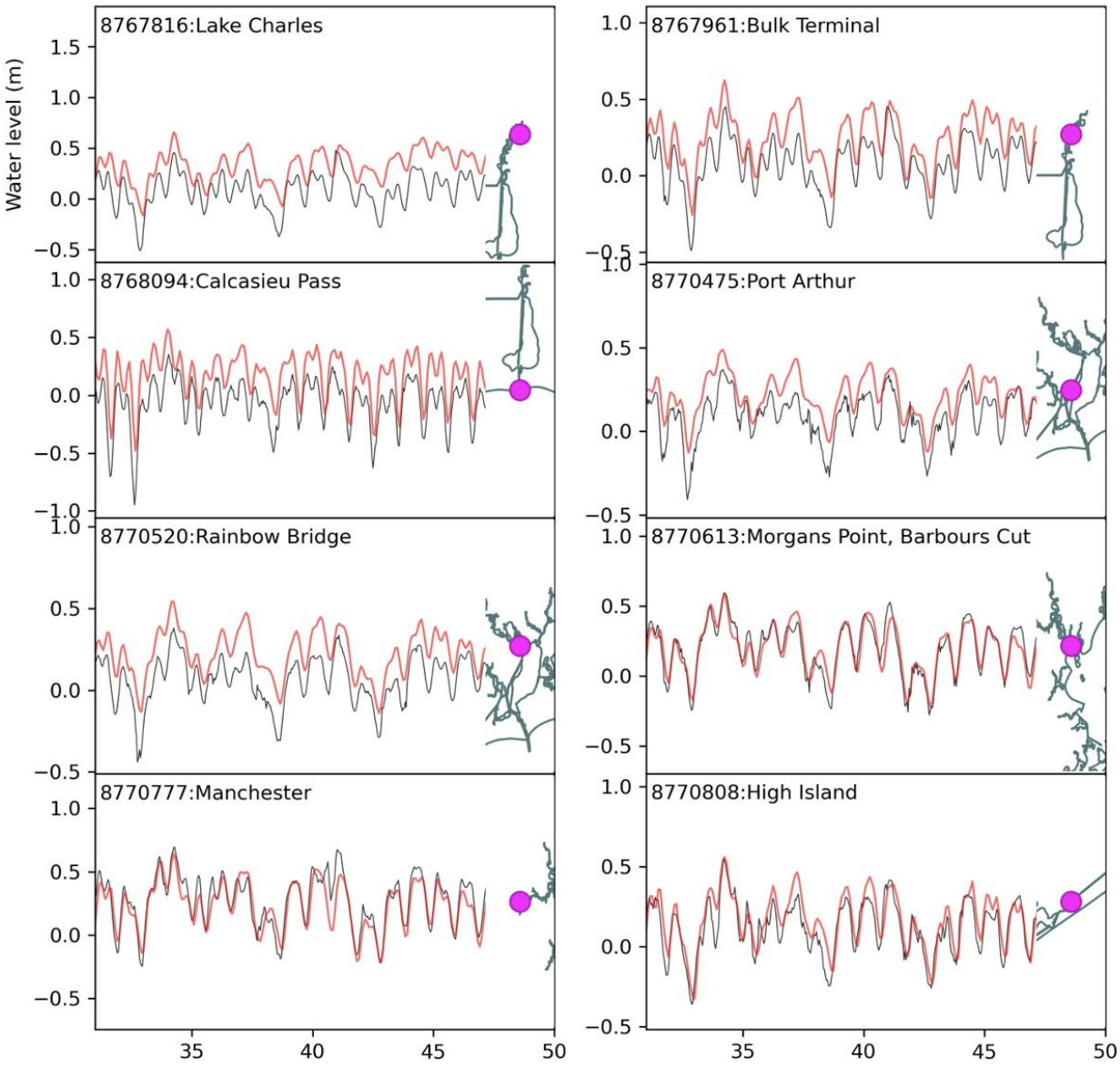


**Figure A1.3**: The same as Fig. A1.1, except for other locations.

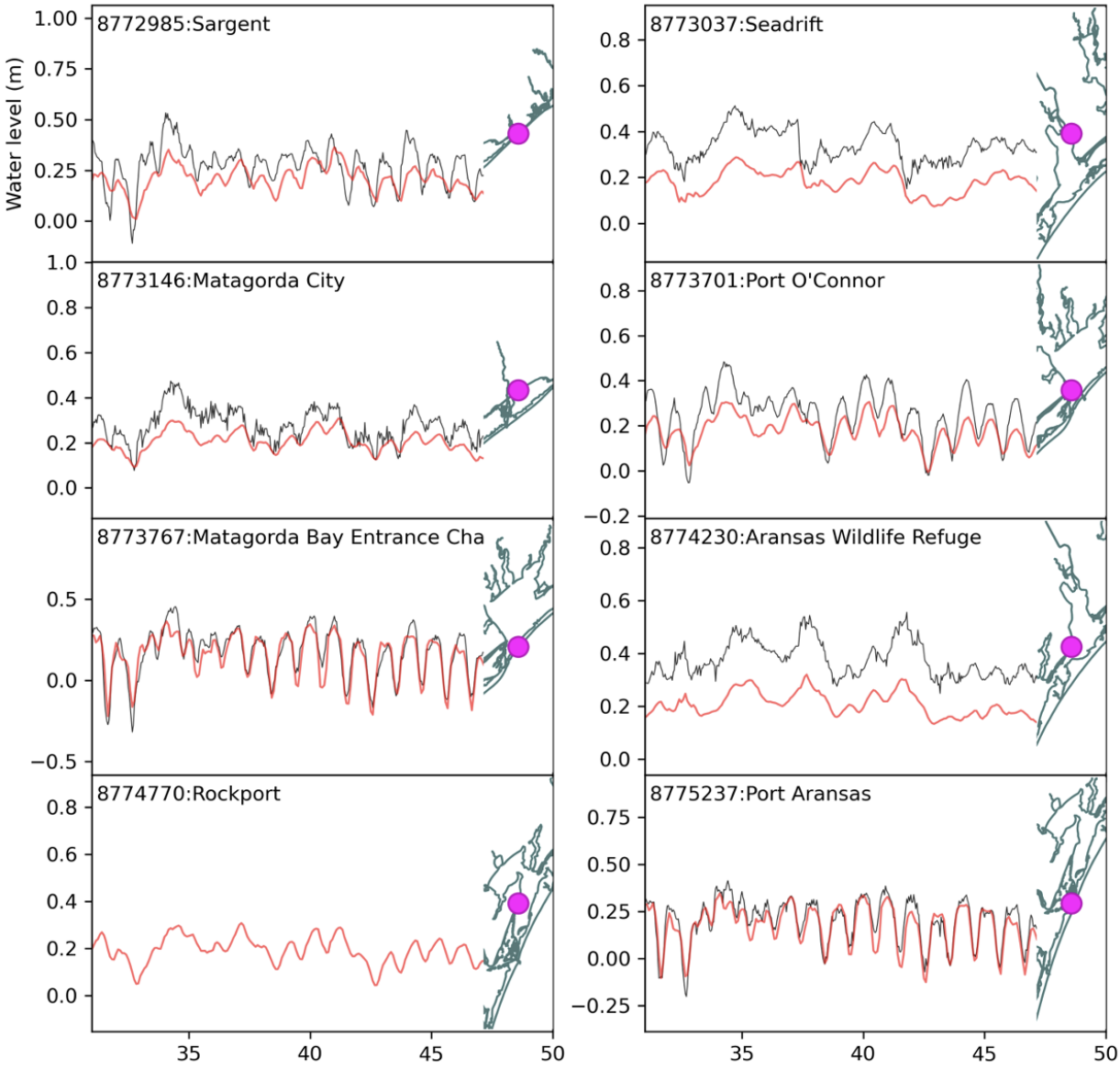


**Figure A1.4**: The same as Fig. A1.1, except for other locations.

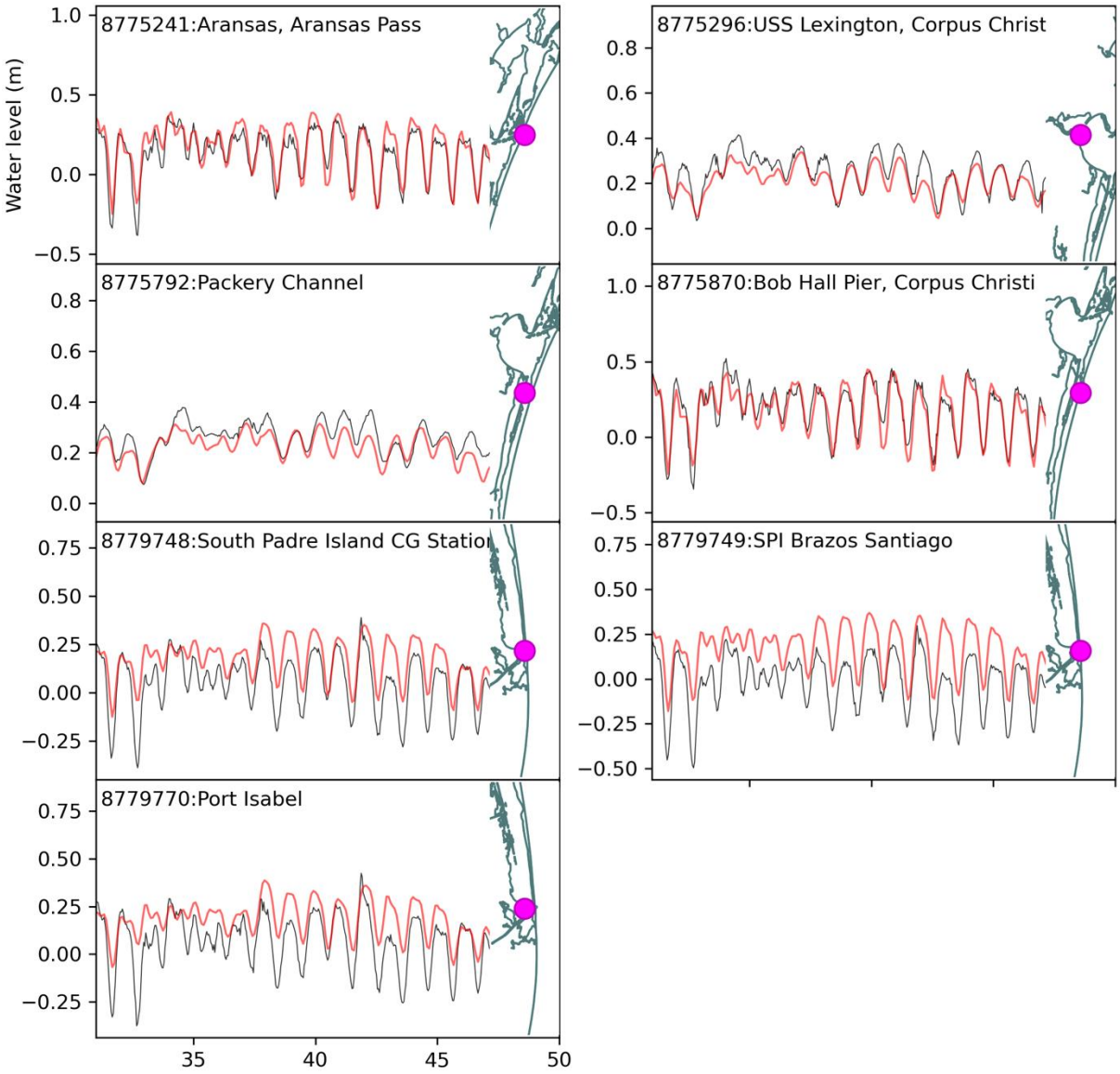


**Figure A1.5**: The same as Fig. A1.1, except for other locations.

# Appendix II: Current velocity comparison between model and observation

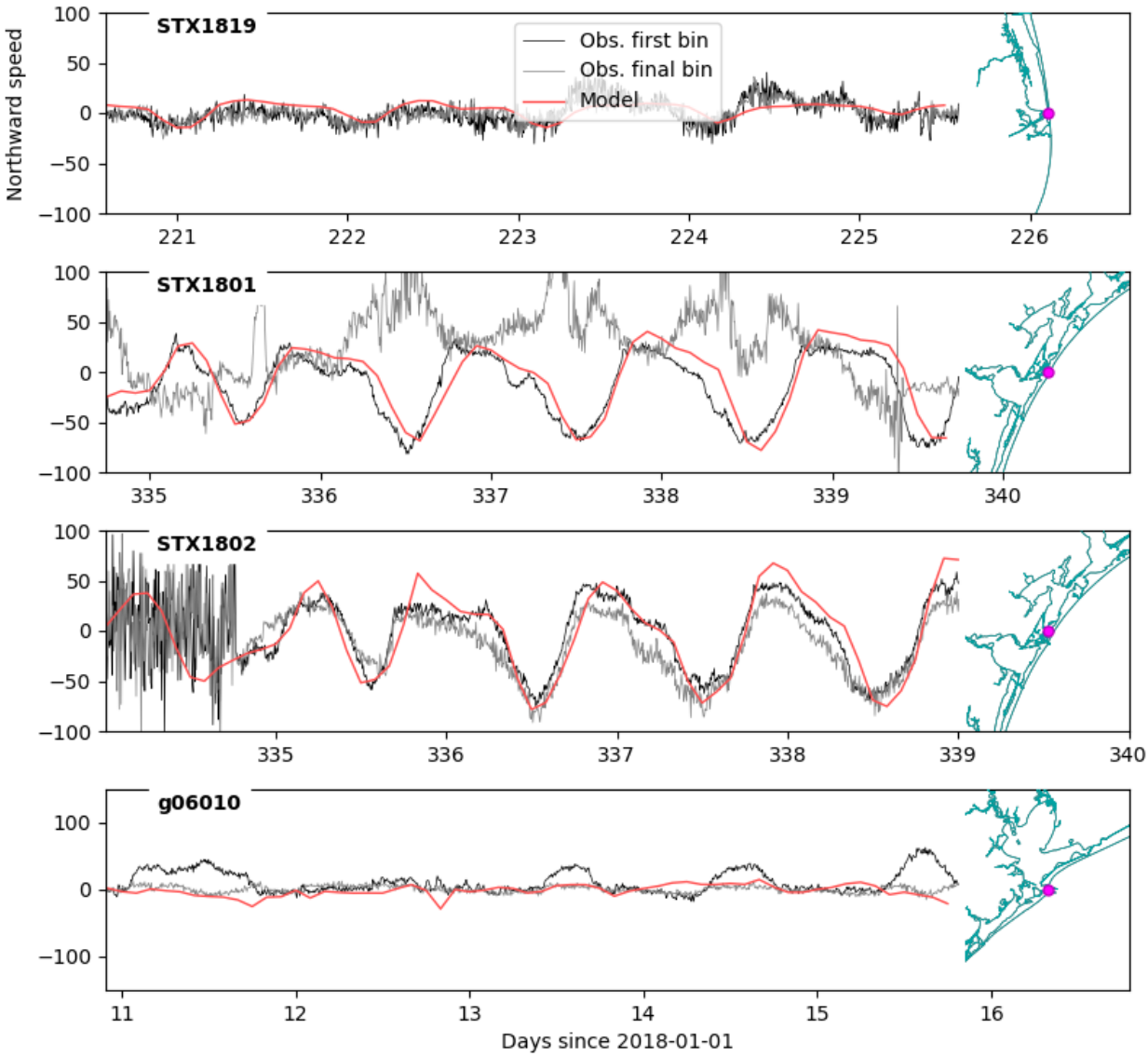


**Figure A2.1**: Comparison of northward current velocity between model (red) and observation (black) at selected NOAA stations along the Texas coast for only a 5-day period. The locations of the monitoring stations are marked with magenta dots on the right subsets.

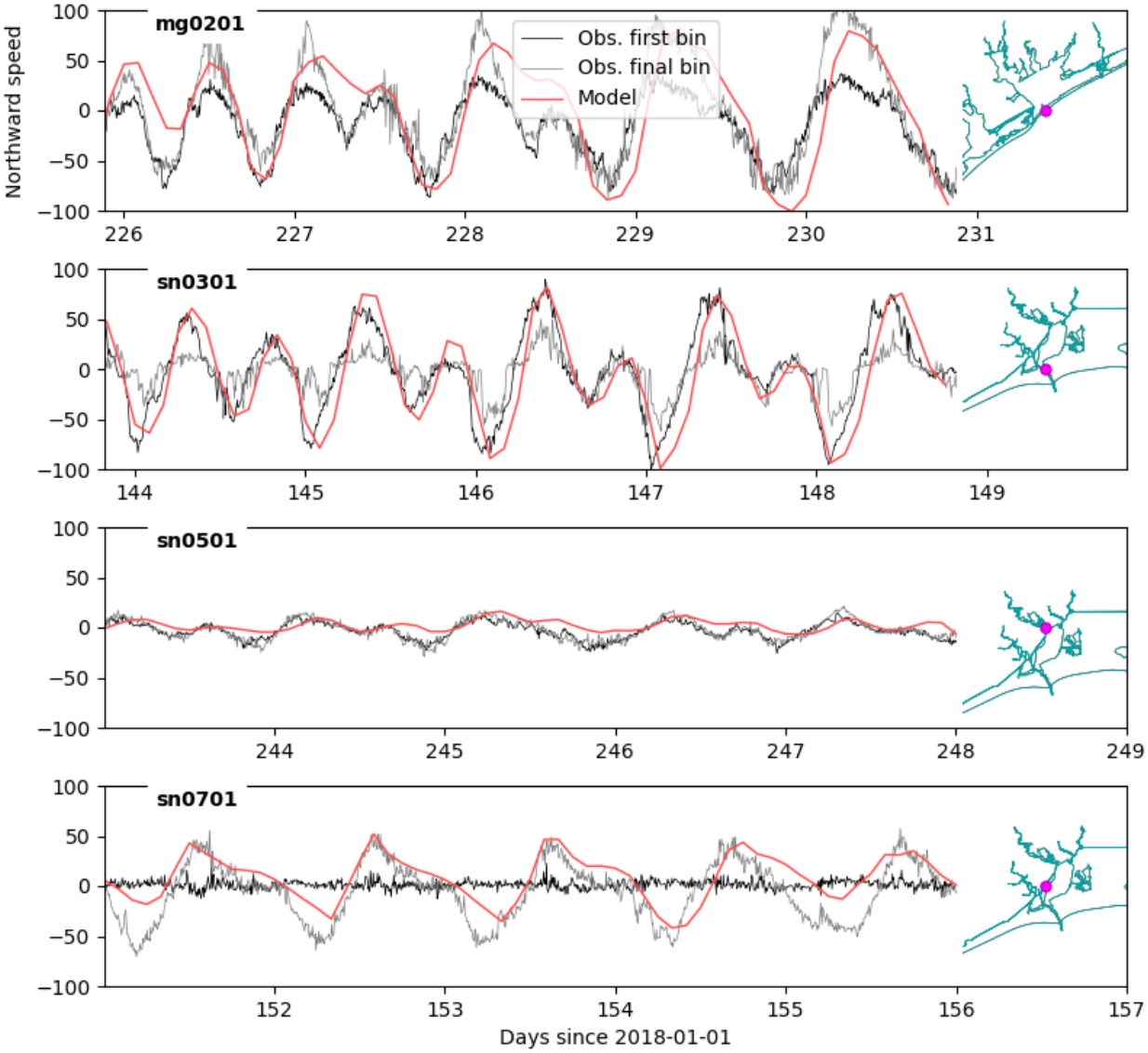


**Figure A2.2**: The same as Fig. A2.1, except for other locations.

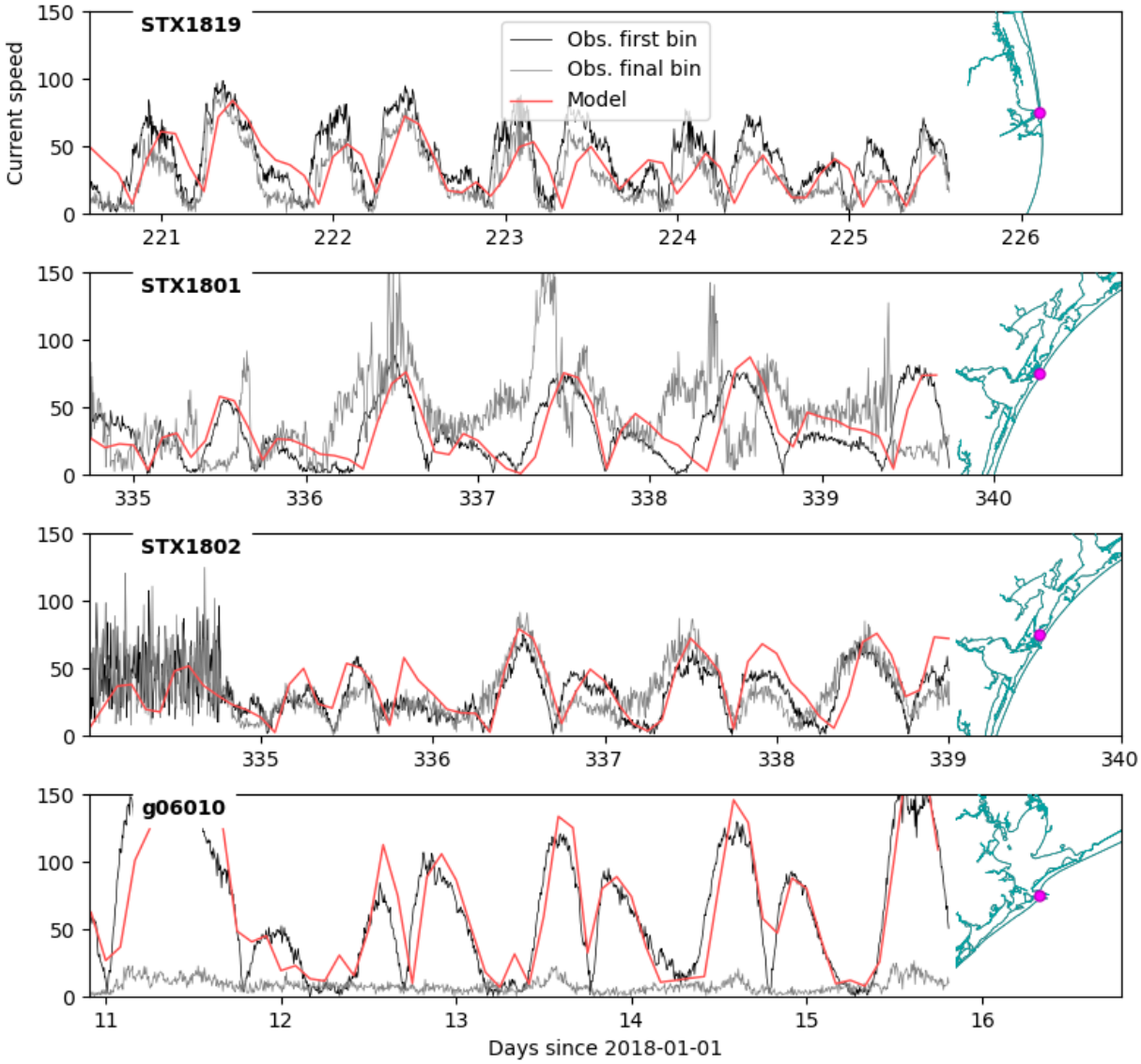


**Figure A2.3**: The same as Fig. A2.1, except for other locations.

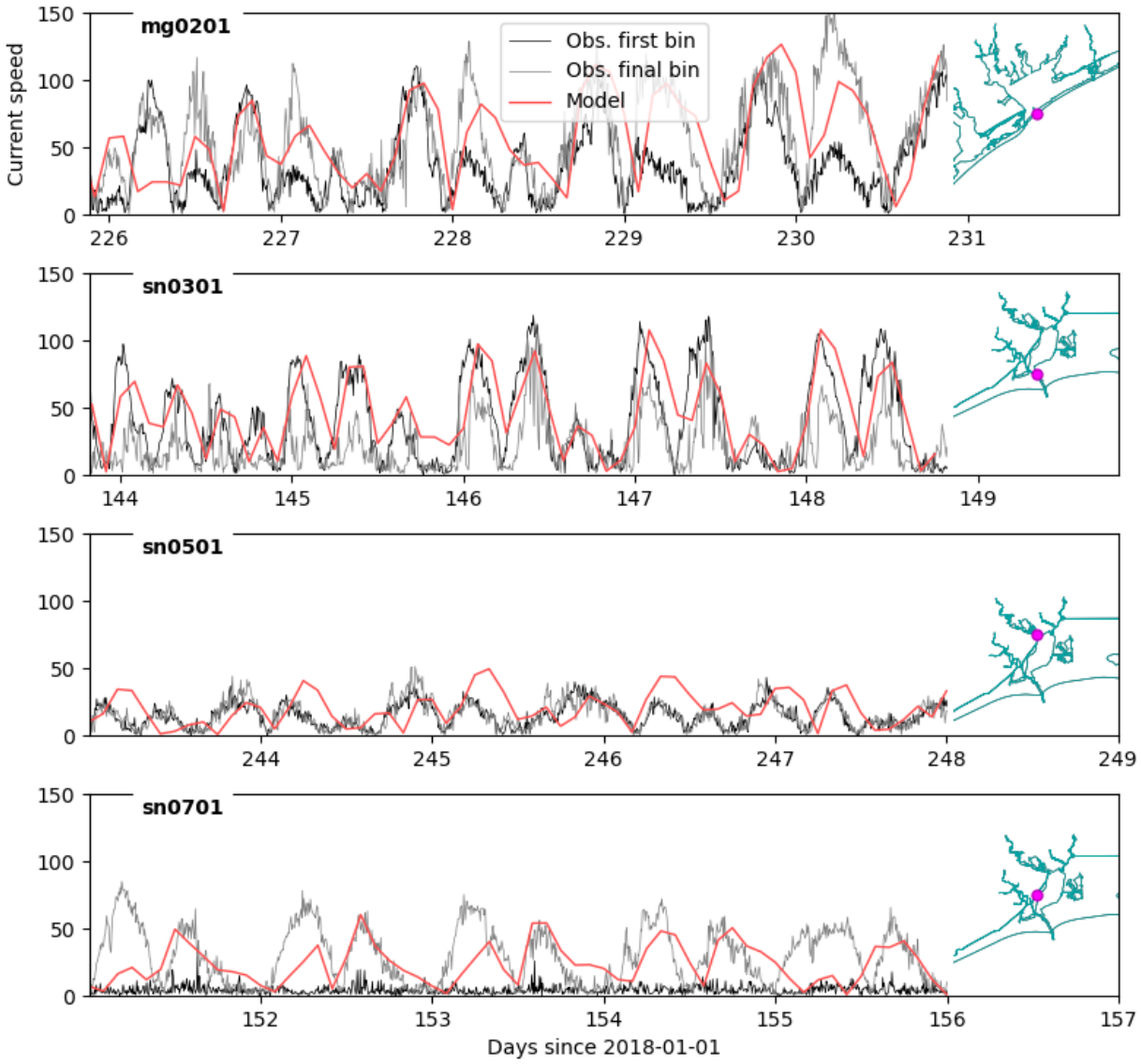


**Figure A2.4**: The same as Fig. A2.1, except for other locations.

# Appendix III: Subtidal salinity comparison between model and observation

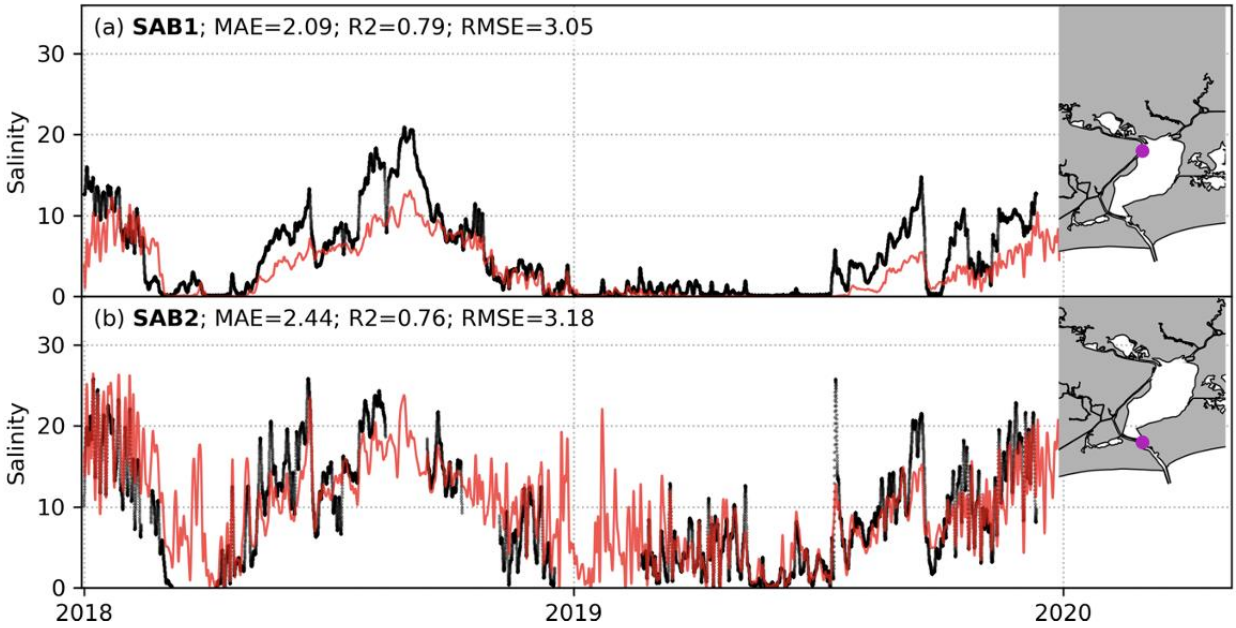


**Figure A3.1**: Comparison of subtidal salinity between model (red) and observation (black) at monitoring stations in Sabine Lake. Monitoring stations are marked with magenta dots on the right subsets.

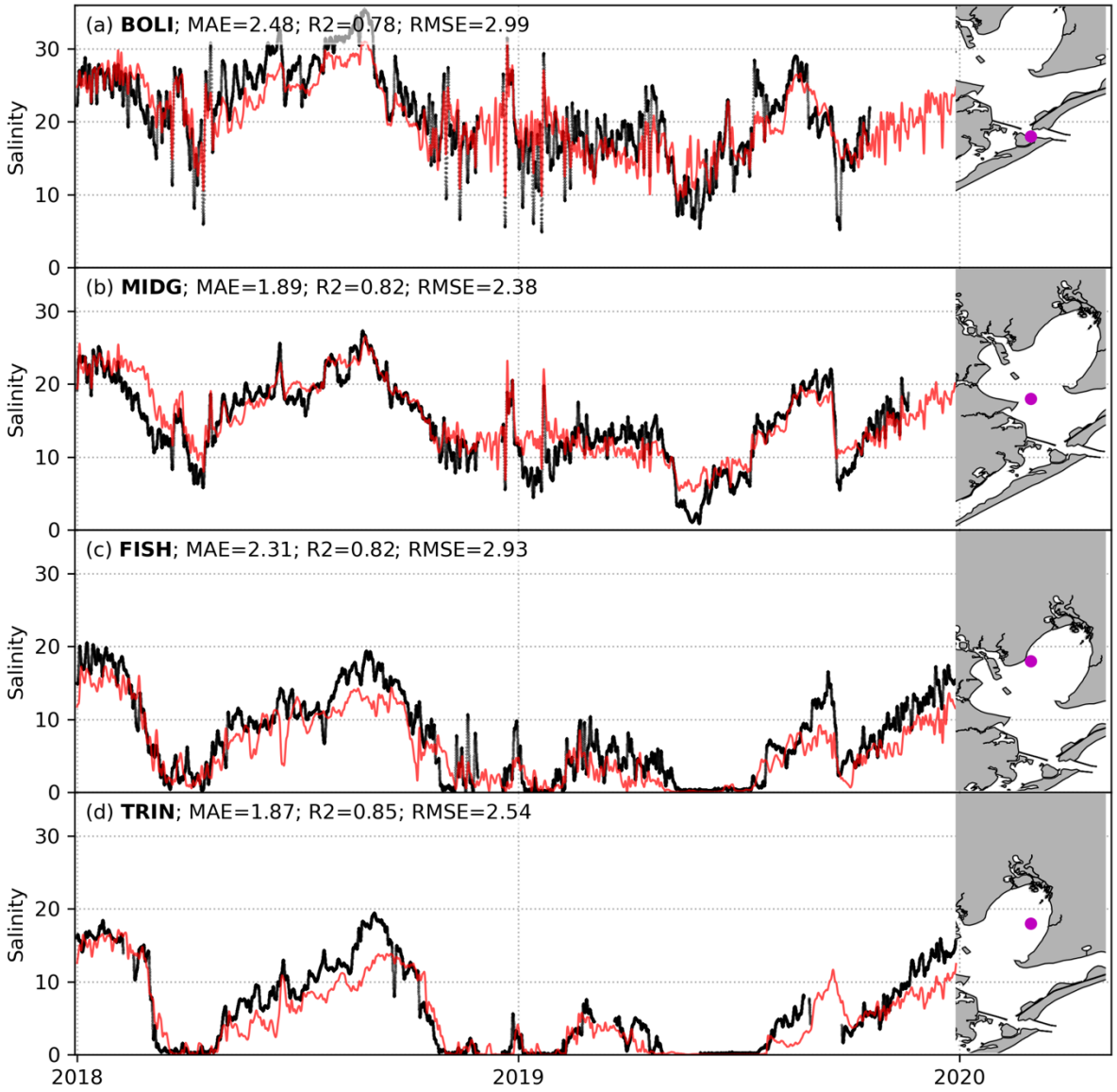


**Figure A3.2**: Comparison of subtidal salinity between model (red) and observation (black) at monitoring stations in Galveston Bay. Monitoring stations are marked with magenta dots on the right subsets.

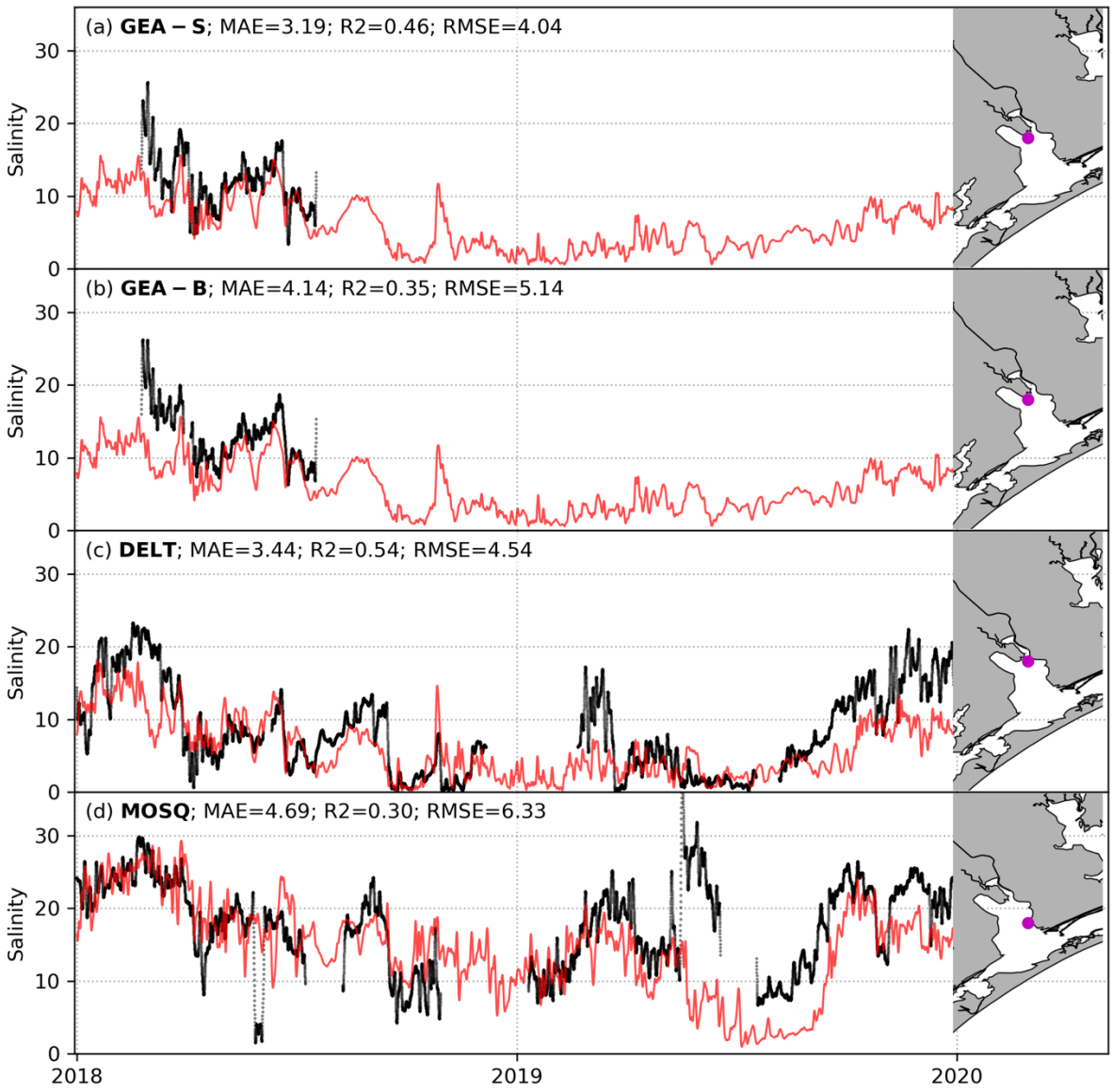


**Figure A3.3**: Comparison of subtidal salinity between model (red) and observation (black) at monitoring stations in Saint Antonio Bay. Monitoring stations are marked with magenta dots on the right subsets.

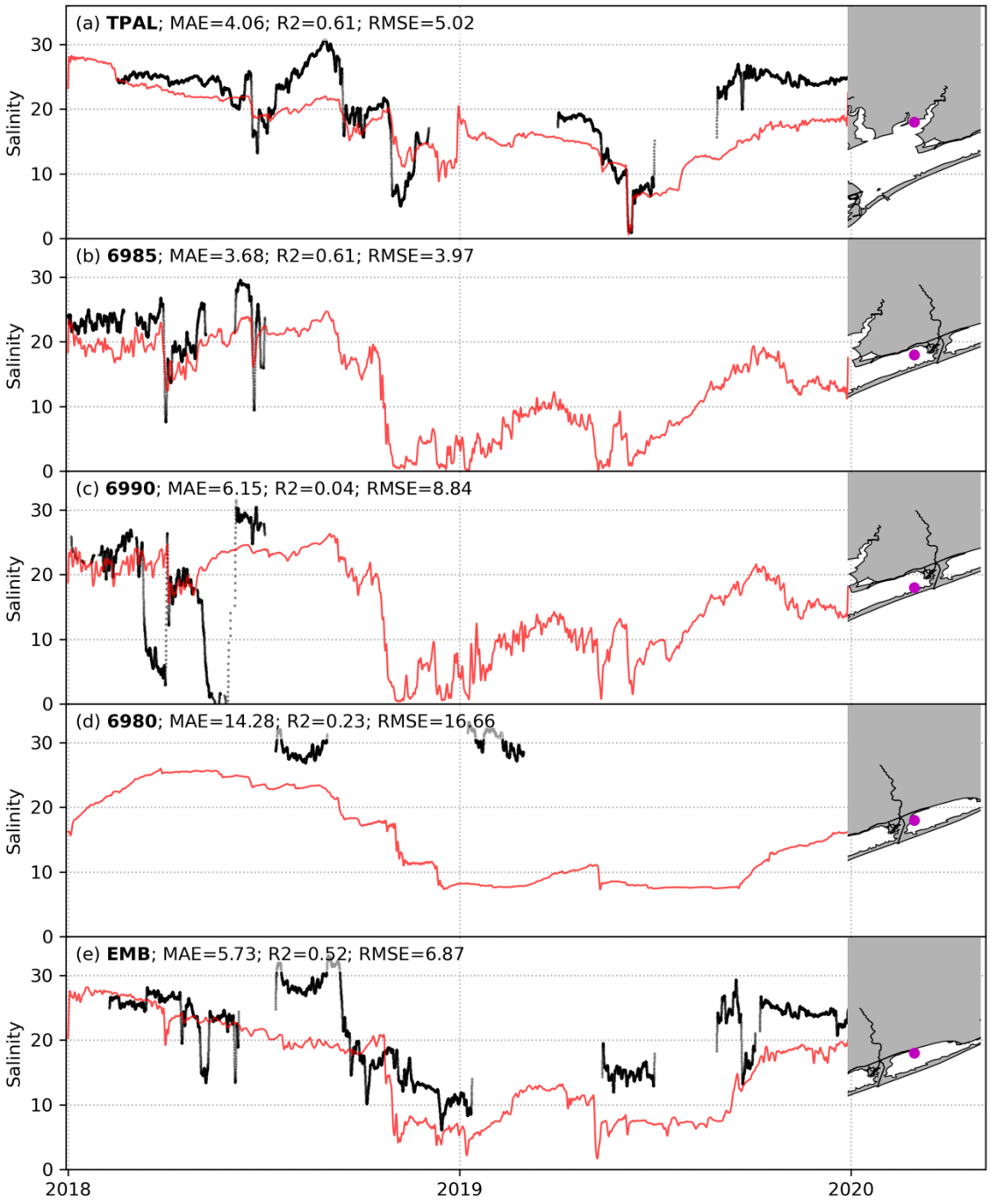


**Figure A3.4**: Comparison of subtidal salinity between model (red) and observation (black) at monitoring stations in east Matagorda and Matagorda Bays. Monitoring stations are marked with magenta dots on the right subsets.

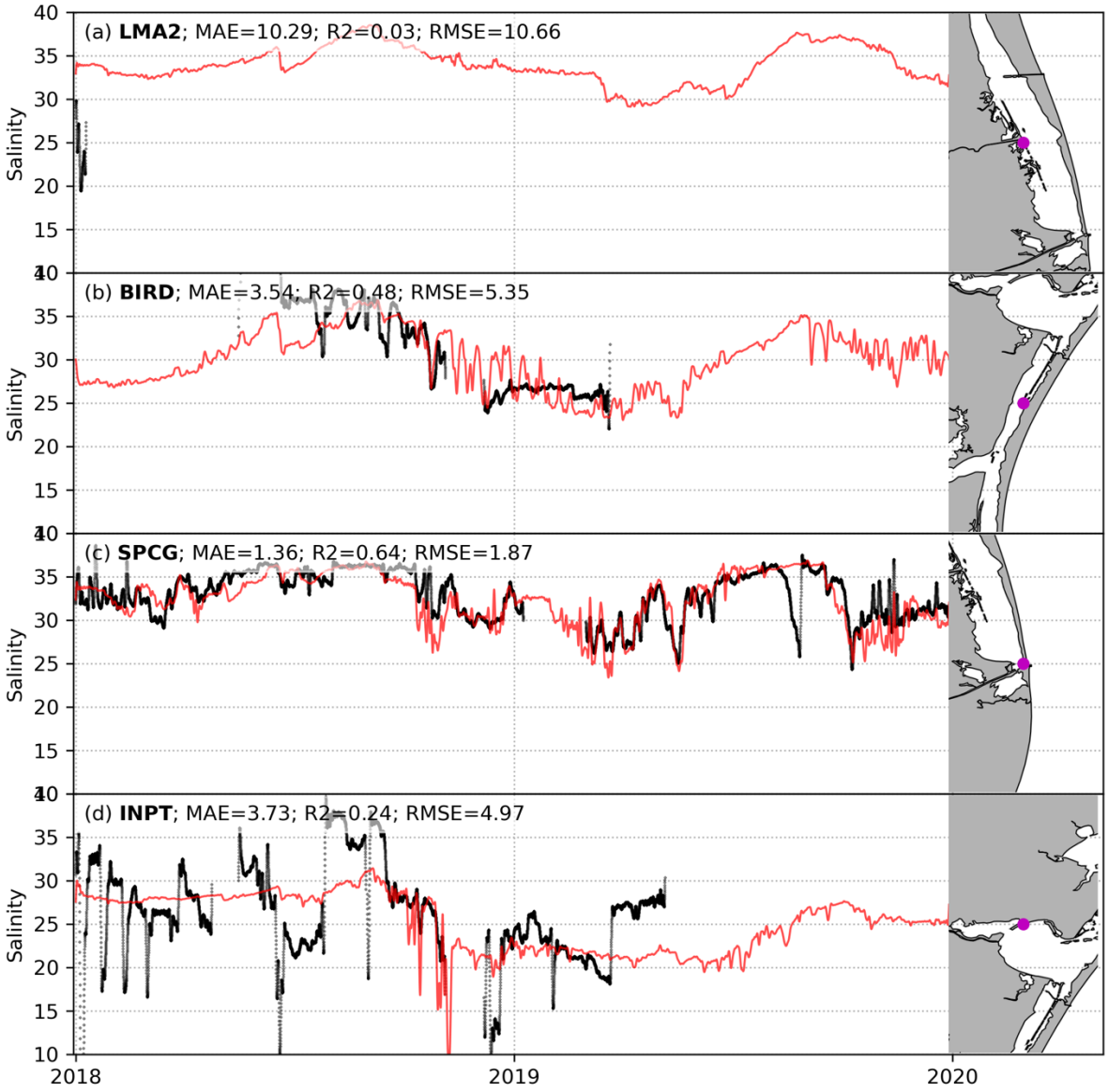


**Figure A3.5**: Comparison of subtidal salinity between model (red) and observation (black) at monitoring stations in Corpus Christi Bay and Laguna Madre. Monitoring stations are marked with magenta dots on the right subsets.

# Appendix IV: Temperature comparison between model and observation

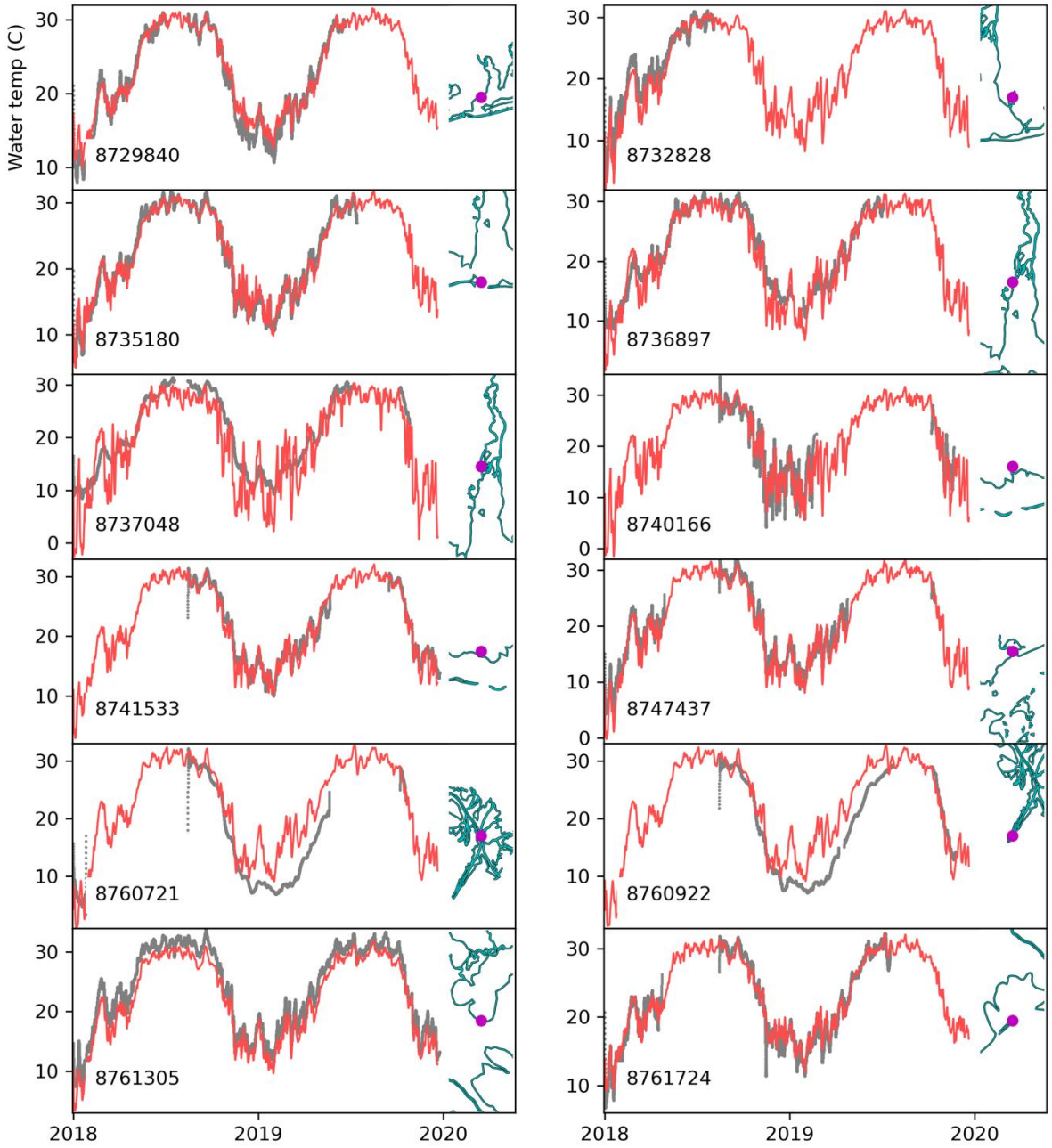


**Figure A4.1**: Comparison of water temperature between model (red) and observation (black) at NOAA gauging stations. The locations of the monitoring stations are marked with magenta dots on the right subsets.

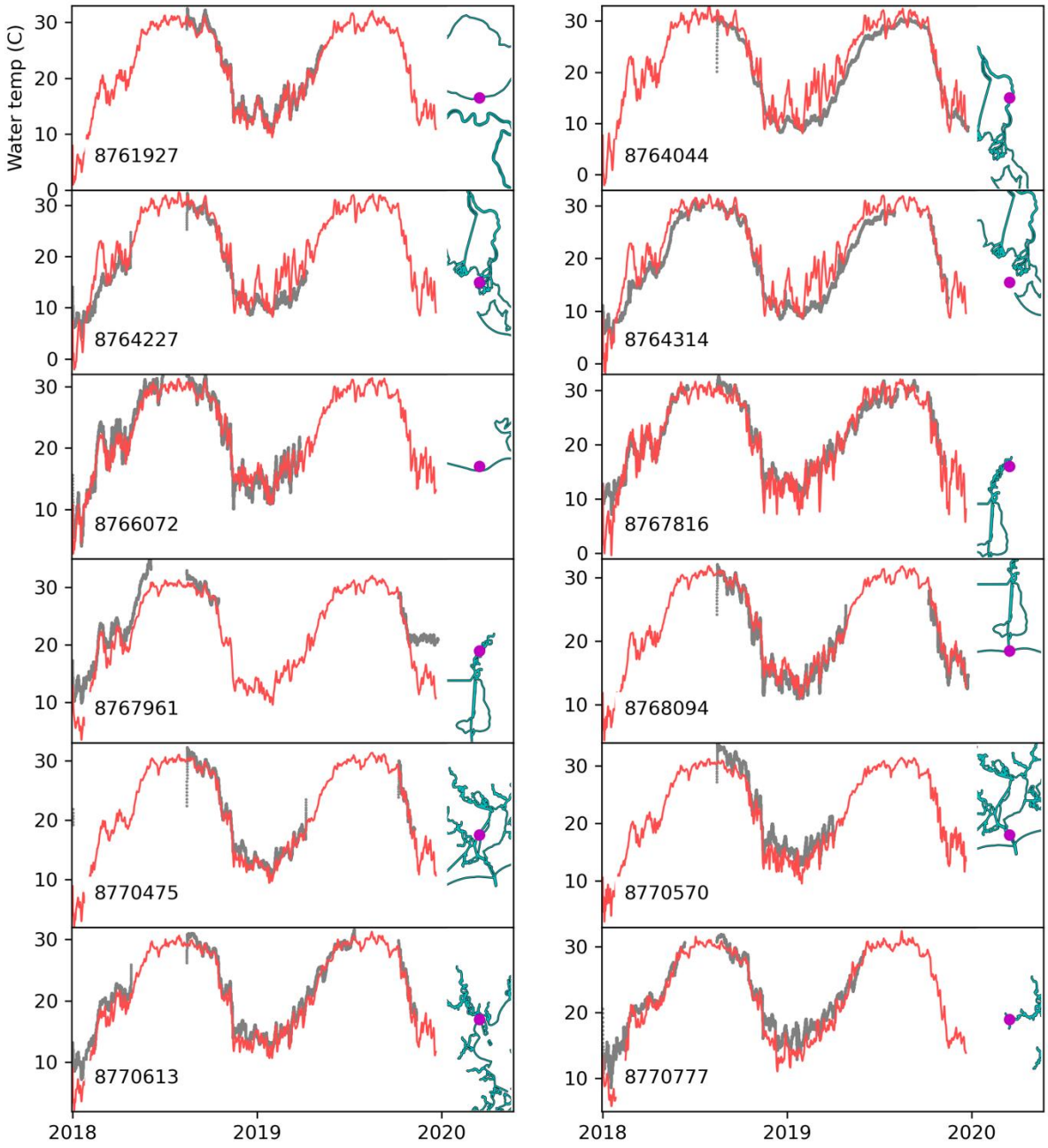


**Figure A4.2**: The same as Fig. A4.1, except for other NOAA gauging stations.

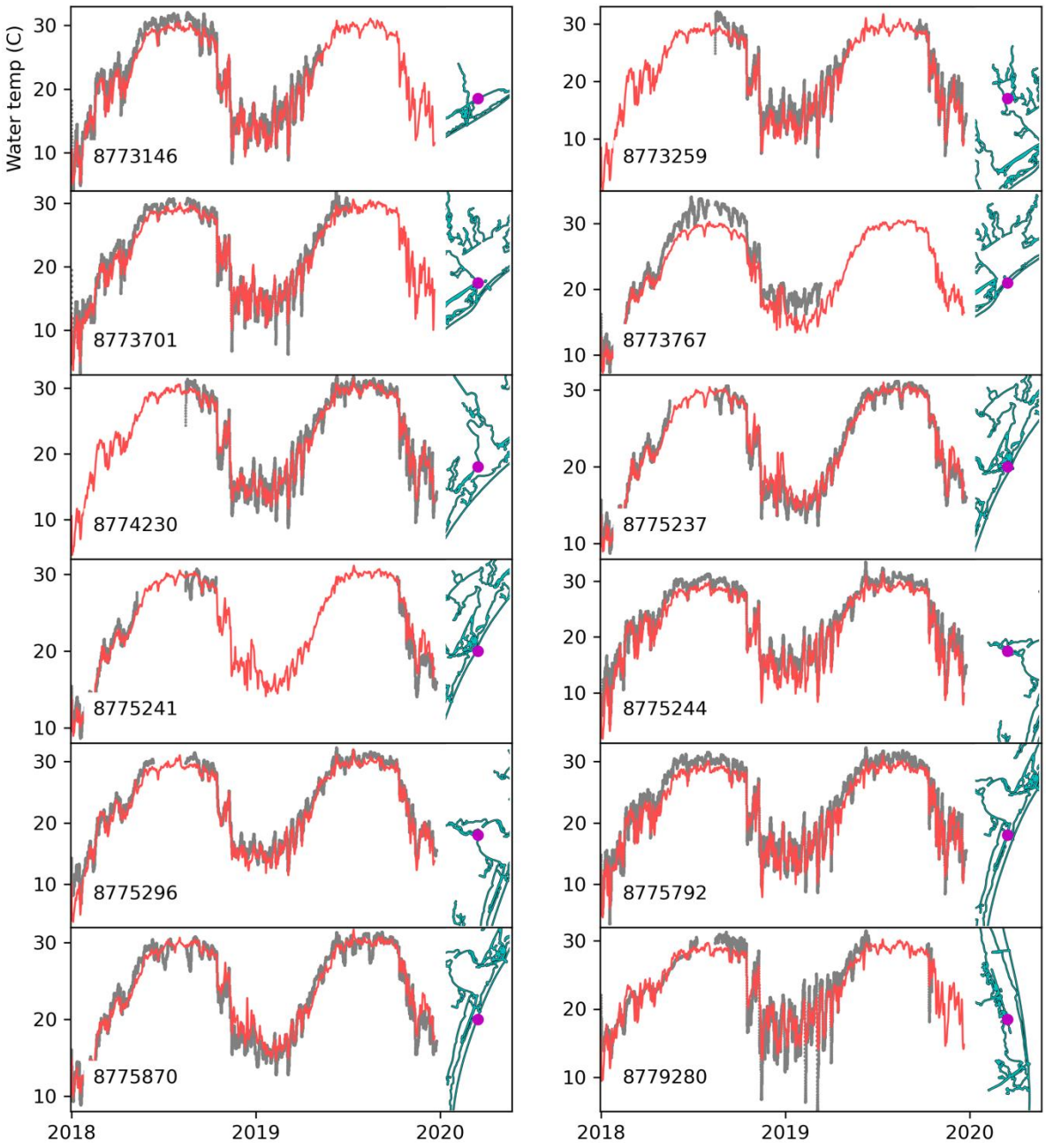


**Figure A4.3**: The same as Fig. A4.1, except for other NOAA gauging stations.